November 2015

Emergent Structure of Multi-Dislocation Ground States in Frustrated Assemblies

Amir Azadi
University of Massachusetts - Amherst

EMERGENT STRUCTURE OF MULTI-DISLOCATION GROUND STATES IN FRUSTRATED ASSEMBLIES

A Dissertation Presented

by

AMIR AZADI

Submitted to the Graduate School of the
University of Massachusetts Amherst in partial fulfillment
of the requirements for the degree of

DOCTOR OF PHILOSOPHY

September, 2015

Department of Physics

EMERGENT STRUCTURE OF MULTI-DISLOCATION GROUND STATES IN FRUSTRATED ASSEMBLIES

A Dissertation Presented

by

AMIR AZADI

Approved as to style and content by:

Gregory M. Grason, Chair

Benjamin Davidovitch, Member

Ashwin Ramasubramaniam, Member

Christian D. Santangelo, Member

Rory Miskimen, Department Chair
Department of Physics

To Mahsa

ACKNOWLEDGMENTS

The creation of this work would not have been possible without my advisor, Greg Grason, whose knowledge, insight and scientific elegance never fail to astonish me. His great impact in shaping my scientific intellect can not be described. Countless hours of valuable discussion we had, along with his guidance and support was the reason and driving force in nucleation and development of ideas in this work.

I owe a tremendous debt to professor Benjamin Davidovitch, whose perspective and theoretical framework on analyzing wrinkle patterns play a central role in this thesis. I am very grateful to him for many stimulating discussions and his feedback on this work.

I would also like to thank my other committee members, professor Christian D. Santangelo and professor Ashwin Ramasubramaniam for their feedbacks.

I also thank my colleagues, Isaac Bruss and Luis Cajamarca for helpful discussions and critical reading of my work.

ABSTRACT

EMERGENT STRUCTURE OF MULTI-DISLOCATION GROUND STATES IN FRUSTRATED ASSEMBLIES

SEPTEMBER, 2015

AMIR AZADI

B.Sc., UNIVERSITY OF TEHRAN, TEHRAN, IRAN

M.Sc., UNIVERSITY OF TEHRAN, TEHRAN, IRAN

Ph.D., UNIVERSITY OF MASSACHUSETTS AMHERST

Directed by: Professor Gregory M. Grason

In this dissertation we study the emergent patterns of multi-dislocation ground states in two geometrically related classes of frustrated assemblies, twisted filament bundles and crystalline spherical cap. We discuss the fundamental role played by characteristic patterns of dislocations in restructuring the ordered phase of theses geometrically frustrated systems in the presence of external stresses. Our analysis on the formation of grain boundary scars leads to universal predictions for the features of defect patterns and their underlying energetic principles.

TABLE OF CONTENTS

LIST OF TABLES

Table **Page**

LIST OF FIGURES

Figure **Page**

CHAPTER 1

INTRODUCTION

1.1 Introduction: Disordering of the ordered state of matters at a glance

Geometrical descriptions of materials have been developed not only to explain complex structures and their properties, but also to design new materials such as colloids, liquid crystals, membranes, glasses and complex filamentous assemblies. This relatively modern attitude, opens the door to the exploration of a broad range of problems emerging at the frontier of bio and nano materials that exhibit complex ordering in their structures. These include self-assemblies of colloids, membranes/vesicles (fig. 1.1E), and low-dimensional nanostructures, such as graphene-like nanosheets and bio-inspired mechanical metamaterials (see fig. 1.1).

The elegant use of topology and geometry of colloidal packing on a sphere is reported in experiments by Bausch and Dinsmore et al. [25, 119] to fabricate solid capsules with precise control of size, permeability and mechanical strength. Theses so called "colloidosomes" are self assembled by colloidal particles onto the interface of emulsion droplets. These "colloidosomes" can be tailored to be the constituent elements of more complex self assembled macro-structure with new functionality. The defective structure of curved membranes (like "colloidosomes") can be tailored using principles that governs the defect patterns, enabling them to self-assemble into more complex, hierarchical macro-structure with new functionality, and material properties. For example tuning the length of the scars and position of the defects, modifies the surface properties to enhance or inhibit the binding of specific molecules (see [1, 2] and fig. 1.1D).

In the realm of "soft condensed matter", we look at self assembled structures bound together by weak, van der Waals forces, like in unpolymerized lipid bilayers. These systems are held together by weak, non-covalent forces with lattice disruptions and packing flaws such as dislocation grain boundaries and disclinations that become unstable with respect to a proliferation of defects upon

heating, fluctuations, out-of-plane buckling or any external field acting on the system via some effective potential or forces.

Historically one of the first realization of the defects in soft assemblies was presented by Sir Lawrence Bragg and J.F. Nye more than sixty years ago. They have designed a simple experimental setup of polycrystalline bubble rafts, assemblies of bubbles, held together by capillary forces on the surface of a solution consisting of water, glycerine, oleic acid and triethanolamine to model metallic crystals. Their model system shows in a striking manner many phenomena which have been suppose to exist in real crystalline metals and alloys such as migration of dislocation, grain boundaries and other types of structural faults and slips under external stresses [3] (see fig. 1.1C).

In the following chapters we focus on principles that govern emergent patterns of multi-defect ground states in two geometrically related classes of frustrated assemblies, "twisted filament bundles" and "curved crystalline sheets" (see fig.1.1) and we illustrate explicitly a mathematical mapping between the elasticity of these two problems.

Often complex structures emerge in condensed matter, as a consequence of a competition between local, short ranged interactions and topological, geometric incompatibility dictated by packings and space filling rules. This type of discrepancy between local and global constraints is often called "geometric frustration". Two parallel classes of geometric models, filamentous assemblies with twisted texture in their cross sectional packings and confined crystalline sheets can reveal the competition between the local rules and geometrical constraints in the bulk. In the first class, the case of helical filamentous assemblies the uniform twist of the structure which induces certain in-plane orientation is incompatible with positional order in the cross section. This simply means that, helical twist makes it geometrically impossible to evenly space filaments in the cross section [5, 122, 123]. In the second class, curved crystalline membranes like the Thomson problem, the geometric frustration is connected to Gaussian curvature of the curved manifold. This simply can be realized in the example of mapping of the sphere (positive curvature) onto the flat plane which is impossible without tearing the sphere. But this is possible by adding material, which leads to formation of defects which can be breaking in translational symmetry, dislocation, or rotational symmetry, disclination [122, 123].

In [6], Klemán revisited the peculiar geometry related to the ordering of parallel lines which are the great circles with intrinsic twist in curved 3-sphere S^3 know as Hopf fibration (which can be generalized to Siefert fibrations). They constructed a class of twisted filament packings in S^3, and demonstrate an isomorphism between locally dense-packed filaments and disk packing on S^2 which shows the geometric frustration in toroidal bundles of equally distant and parallel, although twisted! filaments, are reminiscent of the curved space with spherical geometry. This geometric approach was used for the first time in studying the double-twist texture of blue phases in [7]. Stregraphic projection can rescue these filamentous packing from higher dimension to the physical R^3 space which in turn introduce new level of frustration globally. In this context, Grason introduced an exact mapping between the elasticity of twisted filament bundles and curved membrane with *positive Gaussian curvature* [135]. Despite the distinct geometrical origin, twist generates stresses in the cross-section of filament bundles that are formally equivalent to those induced by a *positive Gaussian curvature* in a membrane, corresponding to a spherical geometry of effective radius, $R_{eff} = \Omega^{-1}/\sqrt{3}$, where $2\pi/\Omega$ is the pitch of helical bundle twist.

In many physical processes, these geometric conflicts give rise to the self-organized emergence of defects in imperfect often crystalline assemblies, in which frustration can only be optimized. This motivate us to search for possible optimal configuration of defects, and their underlying organizing principles. We discuss the fundamental role played by characteristic patterns of topological defects (dislocations and disclinations) in restructuring the ordered phase of theses systems in the presence of external stresses. Our analysis on the formation of grain boundary scars leads to universal predictions for the geometry and symmetry of defect patterns and their underlying energetic principles.

Once in the 1970s existence of a fourth, intermediate phase of matter proposed by [8, 9] in the theory of two-dimensional melting, a surprising refinement to thousands of years old idea of existence of only three states of matter. the central role of dislocation has been revealed in a fourth "hexatic" phase, intermediate between crystal and liquid, and phase-transitions in two dimensions [10, 11, 85]. Since then, central role of defect mediated phases, specifically dislocation riddled states, has been studied extensively for past decades. As a brief survey to what is known

to date, about defect mediated phases, specifically dislocation riddled states in flexible membranes, perhaps one should start with pioneering work by H.S. Seung and David R. Nelson, [28] in studying the fundamental elastic problem of isolated dislocatoin and disclination in buckled membranes. They showed how disinclination as a monopole source of stress "screens" the internal stresses generated by buckled membrane. Later in [29], effective free energy of interacting disclinations has been proposed on the sphere. They argue that in the limit where the sphere radius is large compare to lattice spacing finite length graon boundaries are preferred (also see [125] for application of the effective elastic theory to Thomson problem). Generally, the importance of *disclinations* — points of localized 5- or 7-fold symmetry — has long been recognized, [124, 125].

More recently, experimental [119, 126] (exact realization of "generalized Thomson problem" using colloidal packing at curved oil-water interface), computational [127,128] and theoretical [129–131] studies have begun to recognize the importance of a related class of defects, *dislocations* — "neutral" 5-7 dipoles — in the minimal-energy states of curved crystals, both with and without disclinations. These multi-dislocation chains, known as "scars" [119, 129], that span large portions of the crystal. While heuristic arguments and generic scaling law, have been proposed to explain the scaling of the total number of dislocations with surface curvature [126, 129], to date there is little understanding of precisely how defects are arranged in multi-dislocation ground states and what mechanical, geometric and microscopic parameters govern these emergent structures. In [129–131] the intuitive notion of the Peach-Koehler force acting on dislocation in the pre-existing geometrically induce stress field has been presented. This gives a way to formulate the stability of few number of dislocations on curved manifolds to the point where in-homogenous and long range stress field of dislocations do not disrupt the reference background stress profile. In the continuum limit where the defect core energy is vanishingly small, The stress pattern of curved crystal is dominated by the strain of large number of defects. Problem turns into a complex N body problem with long range interaction. Here we propose a mathematically and conceptuality different framework, in the well-defined asymptotic limit, $W/a \to \infty$ (large system size to lattice spacing).

Our approach relies on the existence of the unique stress-relaxed state for highly defective state which leads to understanding the optimal defect patterns and energetics of the ground states. Furthermore our model system, spherical cap with open boundary (or geometrically identical problem of twisted bundles), provide the opportunity to study the role of boundary forces which was never studied before. In chapter 4 we study the nature and energetics of stability of topologically "charged" and "neutral" crystals (in presence and absence of excess 5-fold disclination) with spherical geometry and generalized boundary forces, that gives rise to distinct optimal defect patterns in the ground state configurations. We show the anomalous phase transition from "neutral" to "charged" topology mediated by compressive and tensile boundary forces and the gaussian curvature.

The emergent patterns of crystalline excitations, encode informations like growth pathways of their host assembly or physical conditions of their surroundings, hence interpreting this connection relies on understanding their geometry, mechanics and equilibrium/non-equilibrium properties. Emergent patterns of defects are an elaborate fingerprint of different types of stresses that act on the system from the environment. Hence tracking the geometry and dynamics of theses topological excitation can reveal the nature of physical interactions between the assembly and its surroundings. Furthermore, tuning the response of these structures to external dynamic and static stimuli via these plastic crystalline excitations is a prelude to control the elastic-geometric coupling of the structure to large shape deformations and fracturing and engineering disordering of the ordered state of matters.

Theoretical frameworks that have been developed here, can be extended and intimately related to other systems in condensed matter physics, as in the case for entangled vortices above the first order flux lattice melting transition in type-II superconductors, where the lines themselves are defects [85]. Another example that extends the applicability of present approach to the field of "hard condensed matter" is related to deformations in graphene-like sheets. The strain fields associated with defects arrangement and migration in binary compound crystals, graphene-like sheets (e.g., h-boron nitride and tungsten disulphide) can create large out-of-plane deformations,

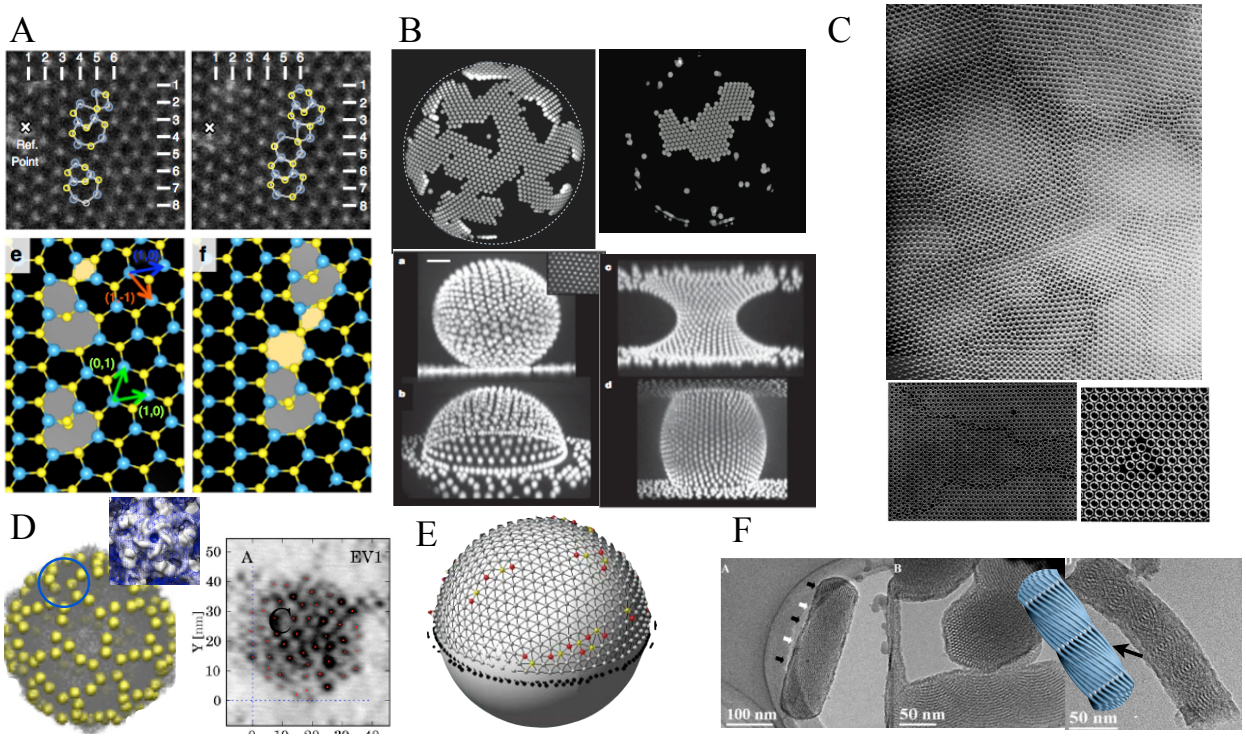

Figure 1.1. topological and geometrical modes of deformation that indicate emergent patterns in a wide range of material systems: **A** ADF-STEM images showing the migration of the dislocation in two-dimensional tungsten disulphide in [114] **B** formation of branched domains during crystal growth on curved oil-water interface in [117]. **C** network of dislocation, grain boundaries and series of fault lines between two areas of parallel orientation and voids in crystalline bubble rafts in [3] (diameter $0.3mm$) **D** site-specific targeting (protein subunits with 5-fold symmetry is targeted) of E-virus capsid by gold NP [4]. **E** assembly of PMMA colloids at oil-water interface that shows defect proliferation on curved surfaces [126]. **F** twisted columnar packing of helical mesoporous silica using achiral surfactants [20]

which in turn modify the 2D layer properties such as mechanical response and electronic properties of crystals by introducing states within their band gap [114], fig. 1.1A.

This thesis is organized as follow, in this chapter we begin by covering the fundamentals of geometrical frustration in two dimensional manifolds (*e.g.* explanation of Euler and Gauss-Bonnet theorem), some mathematical preliminaries and the derivation of the equations of mechanical equilibrium in the nonlinear continuum elasticity on curved surfaces, and the role of boundary conditions. In principal we review the energetic of two dimensional elasticity (stretching and bending) and formulate how singularities in position play a role in the equations of mechanical equilibrium.

Chapter II focuses on the intrinsic frustration occurring in packing of filaments and columns, between the two-dimensional organization of filaments in cross section and out-of-plane inter-filament twist in bundles. Using nonlinear continuum elasticity theory of columnar materials, we study the favorable coupling of twist-induced stresses to the presence of edge dislocations in the lattice packing of bundles, which leads to a restructuring of the ground-state order of these materials at intermediate twist. The stability of dislocations increases as both the degree of twist and lateral bundle size grow. We show that in ground states of large bundles, multiple dislocations pile up into linear arrays, radial grain boundaries, whose number and length grows with bundle twist, giving rise to a rich class of polycrystalline packings. The framework presented in this chapter relies on stability of few number of dislocation where the notion of Peach-Koehler force is sufficient to describe dislocation energetics and stability.

In chapter III, the concept of asymptotic behavior in the continuum limit, $W/a \to \infty$ (large system size to lattice spacing) is applied to the analogue problem of positional order and defects on spherical caps in presence of boundary forces. This leads to organizing principles which explains the emergent symmetry of multidislocation patterns, radial grain boundaries ("neutral scars), as defect proliferate unbounded in the ground state configurations.

The ideas developed in the context of asymptotic analysis of neutral scar patterns in chapter III, generalized to charged scar morphology with arbitrary boundary forces and surface coverage in chapter IV. This shows the central role of boundary forces in breaking the charge neutrality of the lattice with spherical topology and segregating the phase dominated by charged lattice characterized by positively charged bare disclination or decorated by dislocations from the topologically neutral phase stabilizes by tensile boundary forces. Conceptually in the last two chapters we show

that asymptotic and tractable results of continuum theory of scars can replace complex man-body problem of large number of defect singularities with long range interactions by a simple set of stress-relaxed states in which explain the geometry, mechanics and energetics of highly defective and heterogeneous curved crystals.

1.2 Fundamentals of elasticity on curved surfaces with defects

Curved crystallography is associated with geometric frustration, since the hexagonal packing is in conflict with Gaussian curvature. The geometric frustration in terms of topology is revealed by the Euler theorem for a curved surface. This theorem relates the number of vertices (V), faces (F), and edges (E) of any convex polyhedron:

$$V - E + F = \chi \tag{1.1}$$

For the manifold with a boundary the total topological charge on the boundary and in the interior is given by:

$$Q = \sum_{i=1}^{N_b}(4 - c_i) + \sum_{i=1}^{N_i}(6 - c_i) \tag{1.2}$$

where N_b is the total number of disclinations on the boundary, and N_i is the number of disclinations in the interior of the surface and c_i is the coordination number for vortex i. this means that the number of disclinations in the interior is free to change by means of those on the boundary. The Gauss-Bonnet theorem relates the surface curvature K_G to the total topological charge,

$$Q = 6\chi \tag{1.3}$$

where $\chi = (2\pi)^{-1} \int dA K_G$, is also known as integrated Gaussian curvature. For example, spheres with $\chi = 2$, topology requires a minimal number of twelve 5-fold disclinations. For curved surfaces with open boundaries, the number of defects is not set by topological constraints, instead the

optimal number is determined by the balance between the large elastic costs of defects and their attractive interaction to curvature. To illustrate this subtlety we need to review some aspects of continuum elasticity on curved surfaces in the presence of topological defects.

We begin the analysis of crystalline order on curved surfaces with the elastic free energy

$$E = \frac{1}{2}\int dV(\lambda u_{kk}^2 + 2\mu u_{ij}u_{ij}). \tag{1.4}$$

Here, λ and μ are the Lamé elastic coefficients characterizing the elastic properties of the material, correspond to compressive and shear distortion of the array respectively. u_{ij} is the 2D strain of cross sectional order, defined below. We consider two neighboring points on the surface at $\mathbf{x}$ and $\mathbf{x} + d\mathbf{x}$ and the stress-free reference state is a planar surface. The deformed state is described by $\mathbf{x}'(\mathbf{x}) = \mathbf{x}+h(\mathbf{x})\hat{z}$, where $h(\mathbf{x})$ is the out-of-plane deflection of the surface. The in-plane deformation is encoded in the displacement field, $\mathbf{u}(\mathbf{x})$ which maps points in the reference state to deformed state, $\mathbf{x}' = \mathbf{x} + \mathbf{u}(\mathbf{x})$. We define the strain tensor in terms of the change in separation between points in the reference state, $d\ell^2$, and deformed state, $d\ell'^2$, and we have $d\ell'^2 - d\ell^2 = 2u_{ij}dx_i dx_j$, where the nonlinear form of the strain tensor is,

$$u_{ij} = \frac{1}{2}(\partial_i u_j + \partial_j u_i + \partial_i \mathbf{u}\cdot\partial_j\mathbf{u} + \partial_i h\partial_j h), \tag{1.5}$$

this form of strain ensures the rotational invariance of the 2D solid. We will ignore the non-linear contribution to u_{ij} from derivatives of $\mathbf{u}$ and keep the in-plane gradients of h,

$$u_{ij} = \frac{1}{2}(\partial_i u_j + \partial_j u_i + \partial_i h\partial_j h), \tag{1.6}$$

In the absence of topological defects, the displacement field is a single-valued mapping, but defects disrupt this mapping. In general, two types of defects contribute to the right-hand side of equation (3.6) as the sources of the stress: disclinations and dislocations [28]. Disclinations are disruptions of the orientational symmetry of the lattice and are associated with singular configu-

rations of $\theta_6(\mathbf{x}) = \frac{1}{2}\epsilon_{ij}\partial_i u_j$, the bond angle of the lattice. Around a single disclination, θ increases or decreases by an integer multiple of $2\pi/6$,

$$\oint d\ell \cdot \nabla_\perp \theta_6 = s, \tag{1.7}$$

where $s = (2\pi/6)n$ is the topological charge of the disclination. Dislocations are associated with singular configurations of $\mathbf{u}(\mathbf{x})$ and defined in terms of a closed loop integral around which $\mathbf{u}$ changes by an integer multiple of the lattice spacing along one of the six-fold directions,

$$\oint d\ell \cdot \nabla_\perp u_i = b_i, \tag{1.8}$$

where $\mathbf{b}$ is the Burgers vector. Multiple point defects in the cross section correspond to the defect densities, $s(\mathbf{x}) = \sum_\alpha s_\alpha \delta^{(2)}(\mathbf{x} - \mathbf{x}_\alpha)$ and $\mathbf{b}(\mathbf{x}) = \sum_\alpha \mathbf{b}_\alpha \delta^{(2)}(\mathbf{x} - \mathbf{x}_\alpha)$.

We assume the surface geometry to be fixed (known as "frozen topography") and allow for mechanical equilibrium by relaxing the in-plane displacements $\mathbf{u}$. Minimization of the elastic energy, eq.(4.3), with respect to variations in $\mathbf{u}(\mathbf{x})$ leads to the Euler-Lagrange equations that describe the static mechanical equilibrium of the system,

$$\frac{\delta(E)}{\delta u_i} \simeq -\partial_j \sigma_{ij} = 0 \tag{1.9}$$

where σ_{ij} is the stress tensor,

$$\sigma_{ij} = \lambda u_{kk}\delta_{ij} + 2\mu u_{ij} \tag{1.10}$$

We proceed to solve for the divergence-free stress, in terms of the Airy stress function χ [48], related to the stress tensor by,

$$\sigma_{ij} = \epsilon_{ik}\epsilon_{j\ell}\partial_k\partial_\ell \chi \tag{1.11}$$

While this definition of σ_{ij} satisfies eq. (1.9) by construction, it is necessary to enforce extra conditions on χ that ensure that the stress corresponds to the physical configuration of $\mathbf{u}$. As in

ref. [28], this compatibility relation may be derived by equating the anti-symmetric derivatives of strain, $\epsilon_{ik}\epsilon_{j\ell}\partial_k\partial_\ell u_{ij}$, from which we derive

$$\begin{aligned} K_0^{-1}\nabla_\perp^4\chi &= \epsilon_{ik}\epsilon_{j\ell}\partial_k\partial_\ell u_{ij} \\ &= 1/2\epsilon_{ik}\epsilon_{j\ell}\partial_k\partial_\ell\left(\partial_i u_j + \partial_j u_i\right) + 1/2\epsilon_{ik}\epsilon_{j\ell}\partial_k\partial_\ell\partial_i h\partial_j h \\ &= s(\mathbf{x}) + \nabla_\perp \times \mathbf{b}(\mathbf{x}) - K_G. \end{aligned} \tag{1.12}$$

the right-hand side of eq. (1.12) may be viewed as sources for Airy stress. The first and second of these denote the sources of stress generated by topological defects, disclinations and dislocations respectively, for which the solution for $\mathbf{u}(\mathbf{x})$ is not single-valued. The final term is the Gaussian curvature, which acts as a source of stress and can be thought as a smeared out distribution of disclinations.

CHAPTER 2

DEFECTS IN CRYSTALLINE PACKINGS OF TWISTED FILAMENT BUNDLES: DISLOCATIONS AND GRAIN BOUNDARIES

2.1 Introduction

Topological defects populate the ground states of many frustrated systems in condensed matter physics [18, 19]. A key example occurs when crystalline order forms on two-dimensional surfaces of non-zero curvature, where the incompatibility between globally straight and parallel directions generates geometrically-induced stresses that favor defects in the crystalline order. On spheres, where topology requires a minimal number of twelve 5-fold disclinations, the problem of determining the ideal structure of in-plane order is known alternately as the *Thomson* or *Thames problem* [22, 124]. This problem has important connections to the structure of viral capsids, which are closed-shell assemblies of proteins [23, 24], and more recently has been the subject of experimental interest in the context of particle-stabilized emulsion droplets [25, 119]. A clear physical picture of the coupling between surface curvature and the presence of topological defects has emerged based on the continuum elasticity theory of crystalline membranes [27–30]. In this theory, disclinations carrying a discrete topological charge act as point sources for in-plane stress that can be screened by a more homogeneous distribution of "topological charge" generated by the appropriate Gaussian curvature of the membrane. From this viewpoint, the net topological charge of disclinations in the lowest energy states of curved membranes is rationally expected to increase with the integrated Gaussian curvature of a membrane, a prediction which has recently been tested experimentally for 2D crystals on surfaces of both positive and negative curvature [31].

Recently, Grason has shown that frustration of crystalline order on spherically-curved surface is fundamentally connected to frustrated order in a distinct class of two-dimensionally ordered materials, namely, twisted filament assemblies [33, 135]. Twisted assemblies of fibrous proteins are

common and important structural elements in many biological materials, such collagen [34,35] and fibrin [36]. In these assemblies, helical twist of the assembly derives from the nature of interactions between chiral biofilaments, while the dense in-plane packing results from strong cohesive interactions between filaments [37–42]. Unlike the case of crystalline membranes where frustration arises from out-of-plane deflections, the frustration of cross-sectional order in the twisted-filament bundle derives from a unique geometrical coupling of in-plane strains and filament tilts [135]. Despite the distinct geometrical origin, twist generates stresses in the cross-section of filament bundles that are formally equivalent to those induced by a *positive Gaussian curvature* in a membrane, corresponding to a spherical geometry of effective radius, $R_{eff} = \Omega^{-1}/\sqrt{3}$, where $2\pi/\Omega$ is the pitch of helical bundle twist. Strictly speaking, due to the free surface at the boundary of the bundle, the twisted-filament packing maps more closely onto the problem of crystalline order of a partial, spherical cap, a problem that has be studied theoretically for both the cases with [43] and without [113] topological defects. Based on this connection, in previous work [33, 135] it was argued that the ground-state order of filament bundles becomes unstable to one or more *5-fold disclinations* in the cross sectional order, when the twist is greater than a critical value, $|\Omega R|_c = \sqrt{2/9} \simeq 0.47$, where R is the bundle radius. Therefore, a range of multi-disclination ground states were predicted for sufficiently large and twisted bundles.

In this chapter, we study the continuum elasticity theory of twisted bundle cross sections to explore a fundamentally distinct class of topological defect configurations in the ground states: "neutral" 5-7 disclination pairs, or edge dislocations in the cross-sectional packing. Though the positive topological charge of a bare 5-fold disclination best neutralizes the negative effective charge generated by the twist, we find a broad range of conditions for which configurations of 5-7 dipoles, or dislocations, in the bundle cross section provide a lower-energy means of screening the geometrically-induced costs of twist. Interestingly, we find that appropriately polarized dislocations are universally attracted to a radial position at $R/\sqrt{3}$ away from the bundle center, a point associated with vanishing azimuthal stresses in twisted bundles. In untwisted bundles, as in a flat 2D crystal, edge dislocations incur an elastic cost per unit volume of roughly $K_0|\mathbf{b}|^2 \ln(R/|\mathbf{b}|)$, where $\mathbf{b}$ is the Burger's vector, K_0 is the 2D Young's modulus [11]. In twisted bundles, we show that an elastic

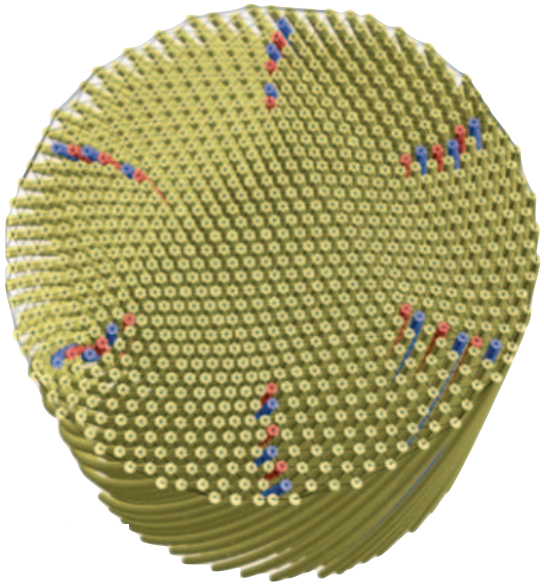

Figure 2.1. Cross-sectional view of the microscopic model of a helical filament bundle with six small-angle grain boundary arms, each with three dislocations. Dislocations are polarized such that 5-fold dislinations (red) are closer to the bundle center than 7-fold (blue).

coupling between geometrically-induced stress and dislocations leads to an additional elastic energy gain per unit volume for optimaly-placed dislocations proportional to $-K_0\Omega^2 R|\mathbf{b}|$. Thus, we show that twisted bundles become unstable to edge dislocations for reduced bundle twists above a threshold value, $|\Omega R| > (\Omega R)_* \sim a/R\ln(R/a)$, where $a \approx |\mathbf{b}|$ is the lattice spacing of the bundle. Unlike the case of disclination stability [33], find that the stability of dislocations is governed by both the twist of the bundle, (ΩR), as well as the size of the bundle relative to the microscopic size of filaments, R/a. Importantly, this analysis shows that the critical twist for dislocation stability, $(\Omega R)_*$, decreases, albeit slowly, to zero as the bundle grows macroscopic in size, as $R/a \to \infty$. A key consequence of this analysis is that large bundles are unstable to *dislocations* over a range of intermediate twist before *5-fold disclinations* are favored for $|\Omega R| > (\Omega R)_c$.

Within this intermediate range of twist $(\Omega R)_* < |\Omega R| < (\Omega R)_c$, we predict a range of complex multi-dislocation ground states, which are quite distinct in structure from well-separated defects in multi-disclination packings of twisted bundles studied in ref. [135]. In these ground states multiple

5-7 dipoles form extended, linear chains, or *grain boundaries*, aligned along the radial directions. Grain boundaries in twisted bundles run from the free surface of bundles and terminate before reaching the central core. An example of a two grain boundary packing of twisted bundles is shown in Figure 2.1. The multi-dislocation ground states of twisted bundles are quite similar to the "grain boundary scars" predicted [29, 125] and observed [31, 119] on spherical crystals in which neutral 5-7 pairs decorate the twelve topologically-required 5-fold disclinations on the sphere. Despite the similar affinity of twist-induced stresses in bundles for positively-charged disclinations, at intermediate levels of twist, the energetically favored defects arrays are "neutral", possessing no excess of 5-fold disclination charge. Based on numerical and scaling analysis of grain boundary screening of twist induced stress we deduce the dependence of the total number of dislocations, N_d, and number of grain boundaries, M, on twist and bundle size. Far above the critical twist we find that $N_d \sim (R/a)(\Omega R)^2$ and $M \sim N_d$.

The organization of this chapter is as follows. In Sec. 2.2 we review the continuum theory of two-dimensionally ordered filament arrays. In Sec. 2.3 we derive the effective energy of dislocations in the cross sections of twisted bundles, and determine the stability of neutral (dislocations) and charged (disclinations) topological defects in the ground states of twisted bundles. In Sec. 2.4 we analyze the structure and thermodynamics of multi-dislocation ground states and appearance of multiple grain boundaries in the cross sections. We also exploit a scaling argument based on the geometry of small-angle grain boundaries to establish the quantitative connection between the length and number of defect arrays in the "polycrystalline" ground states of twisted bundles.

2.2 Continuum theory of filament bundles

The derivation of the equations of mechanical equilibrium in the non-linear continuum elasticity theory of twisted filament bundles have been presented in detail previously [33]. In this section we briefly review the key elements of this analysis, which allow us to construct the effective theory of dislocations in the next section.

We consider a cylindrical bundle of radius, R, of filaments of unlimited length. The stress-free reference state is a hexagonal packing of the straight filaments in the cross section. We describe

the elastic cost of deformations of the cross section order by the following energy,

$$E = \frac{1}{2}\int dV(\lambda u_{kk}^2 + 2\mu u_{ij}u_{ij}). \tag{2.1}$$

Here, λ and μ are the Lamé elastic coefficients characterizing the elastic properties of the material and correspond to compressive and shear distortion of the array respectively, and u_{ij} is the 2D strain of cross sectional order, defined below. In this theory, the elastic energy will penalize distortions of the array that change distances between filaments in a plane *locally perpendicular to the filament tangent direction*, $\hat{\mathbf{t}}$. Hence, eq. (4.3) describes the elastic response of hexagonal-columnar material [46]. While the filaments are uniformly aligned along the $\hat{z}$ direction in the initial configuration, displacements of the array in general lead to filaments that are tilted into the xy plane of initially perfect hexagonal order [47]. This relationship is captured by introducing a two-component displacement field, $\mathbf{u}(\mathbf{x}) = \mathbf{r}_\perp(\mathbf{x}) - \mathbf{x}_\perp$, describing the local deviation in the xy plane of a filament initially at $\mathbf{x}$ and displaced to a position $\mathbf{r}(\mathbf{x})$. For small strains, the in-plane displacement is related to the filament tilt geometrically by, $\hat{\mathbf{t}}(\mathbf{x}) = \hat{z} + \partial_z\mathbf{u}$.

To satisfy the symmetry considerations described above, the non-linear strain tensor has the form

$$u_{ij} = \frac{1}{2}(\partial_i u_j + \partial_j u_i + \partial_i\mathbf{u}\cdot\partial_j\mathbf{u} - \partial_z u_i\partial_z u_i), \tag{2.2}$$

which, like the displacement, only has components in the xy plane. The first two terms on the right hand side are the standard symmetric derivatives in the elastic strain tensor. Additionally, there are two non-linear contributions to the strain tensor. The third term ensures the rotational invariance of the 2D solid around the $\hat{z}$ axis. The final term is unique to the theory of columnar materials and preserves the invariance of the elastic energy about an axis in xy plane [47]. Since $\hat{\mathbf{t}}_\perp \simeq \partial_z\mathbf{u}$, intuitively this contribution to u_{ij} shows that for a fixed separation in the xy plane, when neighboring filaments are tilted with respect to each other, the distance of closest approach between them is reduced. The presence of this non-linear coupling between filament tilts and in-plane strain necessarily introduces stress in twisted filament bundles [39].

In this study, we consider helically-twisted filament bundles in which the cross-sectional positions of filaments are reorganized due to the presence of geometrically-induced stresses. Formally, we compose the displacement field of the helically twisted assembly from two deformations: an initial (z-invariant) in-plane displacement, $\mathbf{u}(\mathbf{x})$, followed by a uniform helical twist, at a rate Ω, around the $\hat{z}$ axis. We denote the composite (z-dependent) displacement as $\mathbf{u}_\Omega$, which has the form

$$\mathbf{u}_\Omega(\mathbf{x}) = \cos(\Omega z)\big[(x+u_x)\hat{\mathbf{x}} + (y+u_y)\hat{\mathbf{y}}\big] \tag{2.3}$$

$$-\sin(\Omega z)\big[(y+u_y)\hat{\mathbf{x}} - (x+u_x)\hat{\mathbf{y}}\big] - \mathbf{x}_\perp. \tag{2.4}$$

In this configuration is it is straightforward to show that in-plane components of filament orientation have the following texture,

$$\hat{\mathbf{t}}_\perp \simeq \partial_z \mathbf{u} = \Omega\rho\hat{\phi}, \tag{2.5}$$

where ρ is the radial distance of the filament from the bundle center in the deformed state, and $\hat{\phi}$ is the azimuthal direction, also defined with respect to the deformed, or "current" position of the filament.

The helical symmetry of these configurations allow us to describe the state of strain for all z, based on the in-plane displacement field, $\mathbf{u}(\mathbf{x})$ at $z = 0$. We assume the rate of twist and filament orientation, described by displacement $\mathbf{u}_\Omega$, eq. (3), to be fixed and allow for mechanical equilibrium by relaxing the in-plane displacements $\mathbf{u}$. This assumption has the advantage that it reduces the problem energy minimization to one of 2D elasticity theory. Minimization of the elastic energy, eq. (4.3), with respect to variations in $\mathbf{u}(\mathbf{x})$ leads to the Euler-Lagrange equations that describe the static mechanical equilibrium of the system,

$$\frac{\delta(E/L)}{\delta u_i} \simeq -\partial_j \sigma_{ij} = 0 \tag{2.6}$$

where L is the length of the bundle and the stress tensor has the standard form an isotropic, 2D elastic medium, $\sigma_{ij} = \lambda u_{kk}\delta_{ij} + 2\mu u_{ij}$. Here, as in ref. [33] we have neglected a term $t_j \sigma_{jk} \partial t_k / \partial r_j$

from eq. (2.6) because it contributes to the stress balance of twisted bundles at higher order in reduced twist, ΩR, which is assumed to be smaller than unity. As the surface of the bundle is free to move, we solve for states of mechanical equilibrium subject to a vanish normal stress at the boundary of bundle

$$\hat{r}_i \sigma_{ij}(\rho = R) = 0. \tag{2.7}$$

We proceed to solve for the divergence-free stress, in terms of the Airy stress function χ [48], related to the stress tensor by,

$$\sigma_{ij} = \epsilon_{ik}\epsilon_{j\ell}\partial_k\partial_\ell\chi. \tag{2.8}$$

While this definition of σ_{ij} satisfies eq. (2.6) by construction, it is necessary to enforce extra conditions on χ that ensure that the stress corresponds to the physical configuration of $\mathbf{u}$. As in ref. [28], this compatibility relation may be derived be equating the anti-symmetric derivatives of strain, $\epsilon_{ik}\epsilon j\ell\partial_k\partial_\ell u_{ij}$, from which we derive

$$K_0^{-1}\nabla_\perp^4\chi = s(\mathbf{x}) + \nabla_\perp \times \mathbf{b}(\mathbf{x}) - K_T. \tag{2.9}$$

where $K_0 = 4\mu(\lambda+\mu)/(\lambda+2\mu)$ is the 2D Youngs modulus. The right-hand side of eq. (3.6) may be viewed as sources for Airy stress. The first and second of these denote the sources of stress generated by topological defects in a bundle cross section, disclinations and dislocations respectively, for which the solution for $\mathbf{u}(\mathbf{x})$ is not single-valued. The final term, denoted as the *intrinsic twist*, derives from the non-linear contribution to u_{ij} from filament tilt,

$$K_T = \frac{1}{2}\epsilon_{ik}\epsilon_{j\ell}\partial_k\partial_\ell t_i t_j = 3\Omega^2. \tag{2.10}$$

A similar contribution derives from the non-linear coupling of elastic strain and membrane tilt in the continuum theory of elastic membranes, where it is known that minus the Gaussian curvature

of the membrane acts a source for Airy stress [28]. Hence, we see that twist in filament bundles generates in-plane stresses that are formally equivalent to those generated by spherical membranes of curvature $3\Omega^2$.

In general, two types of defects contribute to the right-hand side of equation (3.6) as the sources of the stress: disclinations and dislocations [28]. Disclinations are disruptions of the orientational symmetry of the lattice and are associated with singular configurations of $\theta_6(\mathbf{x}) = \frac{1}{2}\epsilon_{ij}\partial_i u_j$, the bond angle of the lattice. Around a single disclination, θ increases or decreases by an integer multiple of $2\pi/6$,

$$\oint d\ell \cdot \nabla_\perp \theta_6 = s, \tag{2.11}$$

where $s = (2\pi/6)n$ is the topological charge of the disclination. Dislocations are associated with singular configurations of $\mathbf{u}(\mathbf{x})$ and defined in terms of a closed loop integral around which $\mathbf{u}$ changes by an integer multiple of the lattice spacing along one of the six-fold directions,

$$\oint d\ell \cdot \nabla_\perp u_i = b_i, \tag{2.12}$$

where $\mathbf{b}$ is the Burgers vector. Multiple point defects in the cross section correspond to the defect densities, $s(\mathbf{x}) = \sum_\alpha s_\alpha \delta^{(2)}(\mathbf{x} - \mathbf{x}_\alpha)$ and $\mathbf{b}(\mathbf{x}) = \sum_\alpha \mathbf{b}_\alpha \delta^{(2)}(\mathbf{x} - \mathbf{x}_\alpha)$.

In the presence of twist- and defect-induced stresses, eq. (3.6) may be solved for χ and subsequently the elastic energy may be computed from,

$$E = \frac{1}{2K_0} \int dV (\nabla_\perp^2 \chi)^2. \tag{2.13}$$

In ref. [33] these equations were solved in the presence of an arbitrary array of disclinations in the cross section of filament bundles by multi-pole expansion, yielding an effective energy written purely in terms of charge and position of disclinations and bundle twist

$$\frac{E}{VK_0} = \frac{3(\Omega R)^4}{128} + \sum_\alpha \frac{s_\alpha}{32\pi}\Big[\frac{s_\alpha}{\pi} - \frac{3(\Omega R)^2}{2}\Big]\Big(1 - \frac{\rho_\alpha^2}{R^2}\Big) \tag{2.14}$$

$$+\frac{1}{2}\sum_{\alpha\neq\beta} s_\alpha V_{int}(\mathbf{x}_\alpha, \mathbf{x}_\beta) s_\beta, \tag{2.15}$$

where V is the bundle volume and

$$V_{int}(\mathbf{x}_\alpha, \mathbf{x}_\beta) = \frac{1}{16\pi^2}\Big(1 - \frac{\rho_\alpha^2}{R^2}\Big)\Big(1 - \frac{\rho_\beta^2}{R^2}\Big) \tag{2.16}$$

$$+\frac{|\Delta\mathbf{x}_{\alpha\beta}|}{16\pi^2 R^2}\ln\left[\frac{|\Delta\mathbf{x}_{\alpha\beta}|^2}{(R^2-\rho_\alpha^2)(R^2-\rho_\beta^2)/R^2 + |\Delta\mathbf{x}_{\alpha\beta}|^2}\right], \tag{2.17}$$

and $\Delta\mathbf{x}_{\alpha\beta} = \mathbf{x}_\alpha - \mathbf{x}_\beta$. This energy has three contributions: the first term describes the elastic cost of twist; the second term is the defect self energy and twist-defect interaction; and the third term describes the elastic interaction between disclinations. Importantly, both the disclination self-energy terms in (4.17) and interaction terms in (4.18) vanish continuously as disclinations approach the bundle surface, $\rho_\alpha \to R$. As noted in [33], this property derives from the screening of far-field stresses induced by topological defects by boundary-induced stresses as defects draw near to the free boundary.

2.3 Elastic energy of dislocations in twisted bundles

2.3.1 Dislocation energies and interactions

In this section, we take advantage of the dual description of dislocations, which may be constructed from neutral 5-7 pairs of disclinations [11] to derive the continuum theory of dislocation energies and interactions in twisted bundles. The theory of edge dislocations in the cross section of (untwisted) cylindrical crystals was originally studied in detail by Koehler [49]. In this study, the resulting forms for dislocation self-energy and interaction energies were derived in terms complex area-integrals of stress distribution overlap, which were then analyzed numerically. In the present study, the exact, closed-form expressions for *disclinations energies* derived in ref. [33] allow us to derive the algebraic formula for the full position- and orientation dependence of *dislocation* energies in cylindrical crystals.

From eq. (3.6) we may show that far field stresses generated by a single dislocation of Burgers vector $\mathbf{b}$ at $\mathbf{x}$, may be constructed by superposing a 5-fold disclination, $s = +2\pi/6$, at $\mathbf{x} + \mathbf{a}/2$ and 7-fold disclination, $s = -2\pi/6$, at $\mathbf{x} - \mathbf{a}/2$, where $\hat{z} \times \mathbf{a} = (2\pi/6)\mathbf{b}$. Defining $\chi_+(\mathbf{x})$ as the Airy stress generated by a single 5-fold disclination, $s = +2\pi/6$, which was calculated exactly in ref. [33], the Airy stress corresponding to a dislocation at $\mathbf{x}$, denoted by $\chi_{disl}(\mathbf{x})$, is given by

$$\chi_{disl}(\mathbf{x}) = |\mathbf{b}| \lim_{a\to 0} \Big[\frac{\chi_+(\mathbf{x} + \mathbf{a}/2) - \chi_+(\mathbf{x} - \mathbf{a}/2)}{a} \Big]. \tag{2.18}$$

To calculate the energy of a single edge dislocation in the bundle cross section, we simply superpose a 5-7 disclination pair separated by a vector $\mathbf{a}$, sum the self- and interaction energies described in eq. (4.17), and expand the resulting energy to second order in a/R. This results in the following energy for a single dislocation,

$$E_{disl} = E_{self} + E_{twist}. \tag{2.19}$$

where,

$$\frac{E_{self}}{VK_0} = \frac{b_\phi^2}{8\pi^2 R^2} \left(\frac{\rho}{R}\right)^2 \tag{2.20}$$

$$+ \frac{|\mathbf{b}|^2}{8\pi^2 R^2} \left[\ln\left(1 - \frac{\rho^2}{R^2}\right) + \ln\left(\frac{R}{a}\right) \right] \tag{2.21}$$

and

$$\frac{E_{twist}}{VK_0} = -\frac{3\Omega^2}{16\pi} b_\phi \rho \left(1 - \frac{\rho^2}{R^2}\right). \tag{2.22}$$

E_{self} is the elastic energy of a single dislocation in an untwisted bundle, which depends largely on the radial position, ρ, and weakly on orientation of the dislocation. This energy is maximal for a central dislocation, $\rho = 0$, and reduces to the well known logarithmically divergent cost for a single dislocation in a bulk crystal [51, 138]. The radial dependence of E_{self} shown in Fig. 2.2a, becomes singular as the dislocation approaches the bundles surface as the boundary-induced force on a dislocation diverges as $\sim (R - \rho)^{-1}$ [49]. Hence, in the limit that $R - \rho \ll a$, the 5-7 disclination superposition is non-analytic as $a \to 0$, and hence the small-a expansion of eq. (2.20) becomes inaccurate.

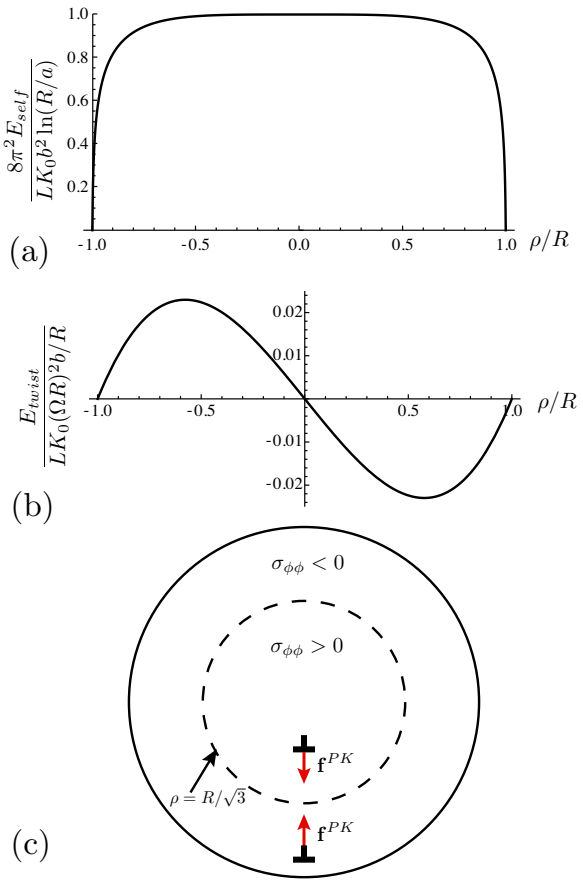

Figure 2.2. The dislocation self-energy is plotted in (a) vs. radial position, ρ. In (b), we show the radial dependence of the elastic coupling between twist and dislocation stresses. In (c), a schematic showing the Peach-Koehler force on disclocations in the presence of twisted induced stress, where $\perp$ indicates the position of an edge dislocation. The dashed line indicates a contour of vanishing hoop stress, to which dislocations in highly-twisted bundles are driven. For each figure, the dislocation orientation is $\mathbf{b} = b\hat{\phi}$.

E_{twist} describes the elastic coupling between the twist induced stresses and the dislocation stresses shown in Fig. 2.2b. Notably, this coupling is negative and minimal for $\mathbf{b} = b\phi$ and $\rho = R/\sqrt{3}$, demonstrating that twist favors dislocations of a certain polarization and located at a specific radial position in twisted bundles. The favorable orientations of dislocations correspond to disclination dipoles oriented along the radial direction, with the 5-fold end oriented towards the bundle center. Alternatively, we may view such a dislocation as a partially removed row of filaments extending from the free bundle surface to the dislocation.

To understand the origin of an optimal location of dislocation in twisted bundles, we consider an alternative derivation of E_{twist} based on the Peach-Koehler force [52] generated by twist-induced stress. The force per unit length on a dislocation line along $\hat{z}$ subject to imposed stress σ_{ij} is given by,

$$f_i^{PK} = \epsilon_{ij}\sigma_{jk}b_k. \tag{2.23}$$

The stresses generated by twist are described by the solution to $K_0^{-1}\nabla_\perp^4\chi_{twist} = -3\Omega^2$, which can be readily solved to show the following azimuthal stress distribution,

$$\sigma_{\phi\phi}^{twist}(\rho) = \frac{3K_0\Omega^2}{16}(R^2 - 3\rho^2). \tag{2.24}$$

This stress distribution divides the bundle into two regions: tensile hoop stresses, $\sigma_{\phi\phi}^{twist} > 0$, at the bundle core for $\rho < R/\sqrt{3}$; and due to large azimuthal tilt of filaments at the periphery, compressive hoop stresses, $\sigma_{\phi\phi}^{twist} < 0$, for $\rho > R/\sqrt{3}$. Since twist induces a radially symmetric stress, $\sigma_{\phi r}^{twist} = 0$, the force of a dislocation whose Burgers vector is oriented along ϕ (with a 5-7 dipole along $\hat{r}$) is in the $\hat{r}$ direction. As shown in Fig 2.2c, for such a defect in the compressive zone, for $\rho > R/\sqrt{3}$, the Peach-Koehler force drives the dislocation inwards, while in the tensile zone, for $\rho < R/\sqrt{3}$, this force drive the dislocation outwards. Hence, the force vanishes where $\sigma_{\phi\phi}^{twist}$ vanishes at $\rho = R/\sqrt{3}$, the stable position. Combining eqs. (2.23) and (2.24), energetic coupling between twist and dislocations, eq. (2.22), may be readily calculated from the mechanical work of driving a defect into the bundle, $E_{twist} = -b_\phi \int_\rho^R d\rho' \sigma_{\phi\phi}^{twist}(\rho')$.

We end this section with an analysis of dislocation-dislocation interactions in cylindrical bundles. As with E_{self} and E_{twist}, we derive these from the interactions between two neutral disclination pairs. To compute inter-dislocation energies, we sum disclination interactions over two disclinations, $s_1^{\pm} = \pm 2\pi/6$ at $\mathbf{x}_1^{\pm} = \mathbf{x} \pm \mathbf{a}_1/2$, and the second pair of disclinations, $s_2^{\pm} = \pm 2\pi/6$ at $\mathbf{x}_2^{\pm} = \mathbf{x} \pm \mathbf{a}_2/2$. Again, we retain terms to lowest order in a from the expansion of multiple disclination interactions, yielding the interaction energy

$$\begin{aligned}
\frac{E_{int}}{K_0 V} &= \frac{1}{4\pi^2 R^2}\Bigg[-(\mathbf{b}_1 \cdot \mathbf{b}_2)\left(\ln\cos^2\xi + \sin^2\xi\right) + \frac{(\mathbf{r}_1 \times \mathbf{b}_1)(\mathbf{r}_2 \times \mathbf{b}_2)}{R^2}\sin^4\xi \\
&+ \frac{(\mathbf{b}_1 \times \boldsymbol{\Delta}\mathbf{x}_{12})(\mathbf{b}_2 \times \boldsymbol{\Delta}\mathbf{x}_{21})}{|\boldsymbol{\Delta}\mathbf{x}_{12}|^2}\left(1 - \cos^4\xi\right) \\
&+ \frac{(\mathbf{b}_1 \times \boldsymbol{\Delta}\mathbf{x}_{12})(\mathbf{b}_2 \times \mathbf{r}_2)(1-\rho_1^2/R^2) + (\mathbf{b}_2 \times \boldsymbol{\Delta}\mathbf{x}_{21})(\mathbf{b}_1 \times \mathbf{r}_1)(1-\rho_2^2/R^2)}{(R^2-\rho_1^2)(R^2-\rho_2^2) + |\boldsymbol{\Delta}\mathbf{x}_{12}|^2}\sin^2\xi\Bigg]
\end{aligned} \tag{2.25}$$

Here, $\mathbf{r}_i$ measures the position of ith dislocation with respect to the bundle center, and ξ is defined by

$$\cos^2\xi = \frac{|\boldsymbol{\Delta}\mathbf{x}_{12}|^2}{(R^2-\rho_1^2)(R^2-\rho_2^2) + |\boldsymbol{\Delta}\mathbf{x}_{12}|^2}. \tag{2.26}$$

Due to the presence of the free boundary, this pair potential encodes a significantly more complex dependence on defect orientation and position than the well-known elastic interactions of dislocations in 2D crystals [11,51,138]. However, we notice the well-known form of logarithmic dislocation interactions in bulk crystals is easily obtained by taking the limit that $\rho_i/R \to 0$ of eq. (2.25), for which $\cos\xi \to |\Delta\mathbf{x}_{12}|/R$ and $\sin\xi \to 1$. Additionally, we note that when in the limit where either dislocation approaches the boundary, $\rho_i/R \to 1$, the dislocations interactions vanish, which can easily be verified for the case $\cos\xi \to 1$ and $\sin\xi \to 0$.

2.3.2 Defect phase diagram of twisted bundles

Here, we analyze the stability of disclination and dislocations in the cross section of twisted bundles. As shown previously [33, 135], and eq. (4.17), twist-induced stresses couple favorably to

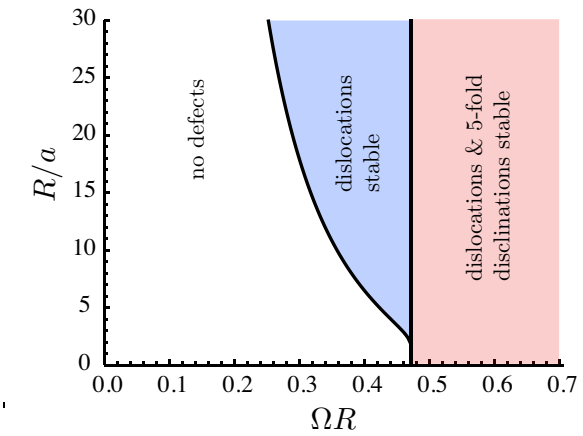

Figure 2.3. The phase diagram indicating stability of appropriately oriented ($\mathbf{b} = b\hat{\phi}$) dislocations and 5-fold disclinations in cross sectional order of twisted filament bundles in terms of reduced twist and reduced size of bundles.

the presence of positively charged ($s = +2\pi/6$), 5-fold disclinations, and above a critical threshold of reduced twist, $|(\Omega R)_c = \sqrt{2/9} \simeq 0.47$, this energetic coupling is sufficient to compensate for the positive self-energy cost of a single disclination at any position. Thus, bundles are unstable to one or more 5-fold disclinations for $|\Omega R| \geq (\Omega R)_c$.

We consider the stability of a dislocation by considering the energy of a single dislocation, which is polarized by twist-induced stress such that $\mathbf{b} = b\hat{\phi}$. Minimizing the sum of eqs. (2.20) and (2.22) over radial position, ρ, we find the value of twist, $(\Omega R)_*$ at which the net cost of a single dislocation vanishes, $E_{disl}(\rho_*) = 0$, where ρ_* is the stable position of the dislocation [1] For larger bundle twists $|\Omega R| \geq (\Omega R)_*$, one or more dislocations is stable in the low-energy packing of twisted bundles.

In Fig. 2.3 we show the value of both the threshold for disclinations and dislocations, $(\Omega R)_c$ and $(\Omega R)_*$, respectively, as functions of R/a, the size of the bundle in units of the lattice spacing, $a \simeq |\mathbf{b}|$. The threshold for 5-fold disclinations is independent of bundle size; however, we find that $(\Omega R)_* < (\Omega R)_c$ for all $R/a \geq 2$. Thus, for fixed bundle size R/a, for increasing values of (ΩR),

[1] In the limit of small R/a, the stable dislocation necessarily approaches the surface of the bundle where the small a expansion of eq. (2.20) fails. In this limit, in order to resolve $(\Omega R)_*$ it is necessary to maintain the full form of the 5-7 disclination pair energy for a finite a.

twisted bundles become unstable to neutral defects, dislocations, before becoming unstable to the 5-fold disclinations in their ground-state packing.

We can roughly estimate the size dependence of $(\Omega R)_*$ in the regime of large bundles. In this limit, the position of the dislocation is determined by the twist energy alone, which is minimal for $\rho_* = R/\sqrt{3}$. Solving $E_{disl}(R/\sqrt{3}) = 0$ critical twist $(\Omega R)_*$, we find

$$(\Omega R)_*^2 \simeq \frac{\sqrt{3}|b|}{\pi R}\left[\ln\left(\frac{R}{a}\right) - 0.072\right]. \tag{2.27}$$

This formula highlights the balance between the logarithmic self-energy of a single dislocation, $\sim K_0|\mathbf{b}|^2 \ln(R/a)$, and the compensating dislocation-twist coupling, $\sim -K_0\Omega^2 R|\mathbf{b}|$. Hence, we find that the threshold twist necessary for stabilizing dislocations in the cross section becomes arbitrarily small as bundles become macroscopic in radius, in the $R/a \to \infty$ limit. This analysis suggests that dislocations proliferate in large bundles, and therefore, understanding the ground state packing requires the study of multi-dislocation structure and energetics.

2.4 Multi-dislocation ground states

2.4.1 Numerical study

In this section we explore the structure of multi-dislocation cross sections in the region of intermediate twist, $(\Omega R)_* < |\Omega R| < (\Omega R)_c$. We base our analysis on a certain class of mechanically stable and high-symmetry dislocation geometries where parallel, $\mathbf{b} = b\hat{\phi}$ dislocations concentrate along M identical radial lines, or "arms", spaced evenly at angular intervals of $2\pi/M$, around the bundle. A similar class multi-dislocation geometries have been studied in the context of grain-boundary screening of isolated disclinations in 2D crystals [130]. In these geometries, each radial line of dislocations is line of mirror symmetry in the defect packing so that $\sigma_{r\phi} = 0$ along these lines and, by eq. (2.23), the ϕ component of force (the glide direction) vanishes for each dislocation. The remaining force balance along the radial direction results from repulsive inter-dislocation forces that favor expansion of the array and the Peach-Koehler force on dislocations arising from twist-induced stresses that favors a restoring compression of the array. As shown in Fig. 2.1, extended strings

of alternating 5- and 7-fold defects constitute tilt grain boundaries across which the orientation of two domains of crystalline order rotates by a discrete angle [51].

To determine the radial position of dislocations in these minimal-energy configurations, we consider the total energy of configurations possessing N_d total dislocations, composed of M equivalent arms of $n = N_d/M$ dislocations per arm. For a fixed dislocation geometry, reduced twist and bundle size, the sum of the single defect energy, eq. (2.19), and interaction energy between defect pairs, eq. (2.25), is numerically minimized with respect to the radial position of the n dislocation "rings" in the array. In this analysis, the minimum spacing between successive dislocations along the array is set to be, a, the lattice spacing.

Fig. 2.4 shows the results for the number and arrangement of dislocations in a bundle of size $R = 100a$ for a range of twist below the threshold for stable 5-fold defects. As the twist increases beyond $(\Omega R)_* \simeq 0.16$, the number of dislocations favored in the cross section increases quickly. For each value of N_d, the geometry of the dislocation packing is labeled by the integer pair, (M, n), denoting the number of grain boundary arms and the number of dislocations per arm, respectively. Along with the total dislocation number, the number of radial grain boundaries also grows with (ΩR), leading 2-, 3-, 4- and 6-fold grain boundary geometries depicted in Fig. 2.4.

In Fig. 2.5 we show results for N_d vs. (ΩR) for a much larger bundle, $R = 700a$. While this bundle shows a similar trend with increasing twist, we note that the threshold for stable dislocations is markedly reduced, $(\Omega R)_* \simeq 0.07$ and a distinct sequence of dislocation geometries is predicted as N_d increases rapidly with twist. Notably, we find for all multi-dislocation geometries over a range from $R/a = 20$ to 700, that grain-boundary arms penetrate only a fraction of the distance from the bundle surface to the bundle center, terminating in the bulk at a finite radius, a feature uncommon in bulk crystalline materials.

To investigate the evolution of grain-boundary structure in bundles with increasing twist, in Fig. 2.6 we plot the number of grain boundary arms, M, vs. N_d for all values of R/a studied. Over the range of dislocations explored here (up to $N_d = 50$) we find little systematic dependence of the growth in the number of grain boundaries on bundle size. Despite more than an order of magnitude variation of bundle size, the trend of increasing number of grain boundaries is consistent

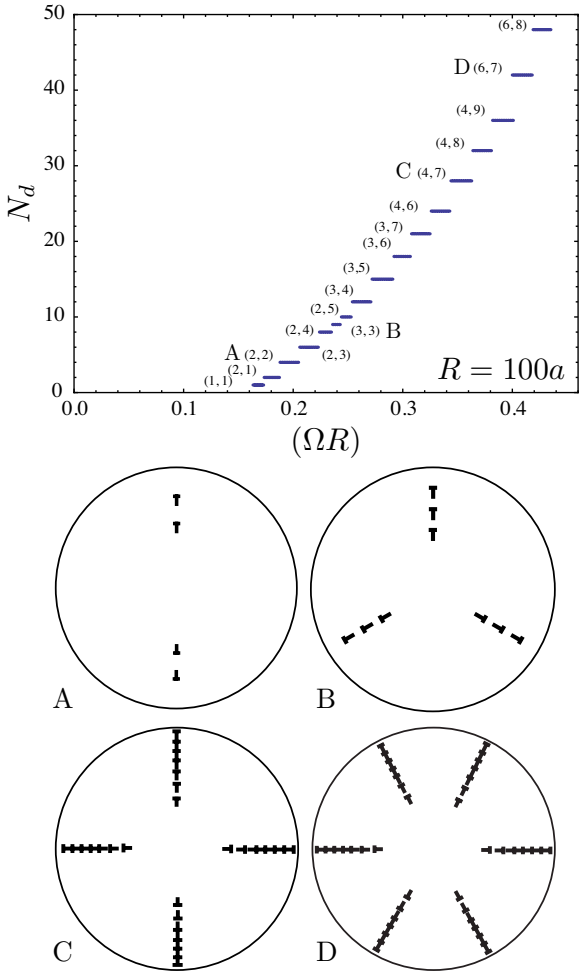

Figure 2.4. (Top) The total dislocation number for ground-state configurations of twisted bundles with multiple dislocations for a bundle of size, $R = 100a$. Integer pairs, (M, n), refer to the number grain of boundary arms and the number of dislocations per arm, respectively. (Bottom) A, B, C, and D show 2-,3-, 4- and 6-fold grain boundary geometries, where $\perp$ labels the position of a single dislocation.

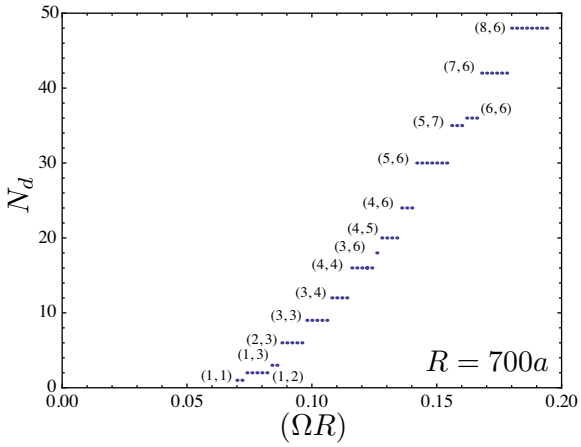

Figure 2.5. The total dislocation number for ground-state configurations of twisted bundles with multiple dislocations for a bundle of size, $R = 700a$. Data points are labeled as in Fig. 2.4.

with a roughly linear relationship, $M \sim N_d$ for all R/a. This suggests that the optimal dislocation geometry is nominally determined by N_d alone, which in turn is regulated by ΩR in a manifestly size-dependent manner, as evidenced by the results for $R = 100a$ and $R = 700a$ bundles, of Figs. 2.4 and 2.5, respectively.

2.4.2 Scaling analysis

Above, we found that the gross structure of the multi-dislocation ground state is predominantly sensitive to the total dislocation number. Here, we consider a simple scaling argument to understand the dependence of N_d on bundle twist and size. This argument is similar to the geometric analysis of "grain-boundary scars" on spherical crystals [29], with the notable exception that in the present case, neutral grain boundaries form in the absence of excess point disclinations. According to the compatibility relation, eq. (3.6), we can formally consider the source of twist-induced stresses, $K_T = 3\Omega^2$, to be a uniform areal density of negatively charged disclinations. Integrating this charge density over the cross section of the bundle we define an effective disclination charge,

$$s_{eff} = -3\pi(\Omega R)^2. \tag{2.28}$$

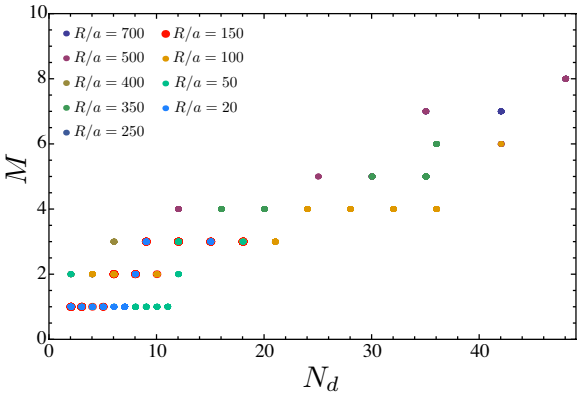

Figure 2.6. Plot of number of grain boundarm arms, M, vs. total dislocation number, N_d for bundle sizes in the range $R/a = 20 - 700$.

As argued in ref. [29], the strain generated by this "topological defect" can be compensated by the presence of M radial grain boundaries, each of which accommodates a rotation of $\theta \simeq a/d$, where d is the mean dislocation spacing along the boundary [54]. Equating the effective topological charge to the total grain boundary rotation, we find the mean-spacing between dislocations,

$$d^{-1} \approx a^{-1}(\Omega R)^2/M. \tag{2.29}$$

Integrating the linear density of dislocations along the length of grain boundaries ($\sim R$) we find the mean number of dislocations per arm,

$$n \approx (R/a)(\Omega R)^2/M. \tag{2.30}$$

Multiplying n by the number of grain boundaries in the cross section, we argue that for large twist, $N_d \sim (R/a)(\Omega R)^2$. To capture both limiting cases of large twist and the critical twist at which N_d vanishes, we construct the following scaling form for total disclination number,

$$N_d \sim (R/a)\left[(\Omega R)^2 - (\Omega R)_*^2\right]. \tag{2.31}$$

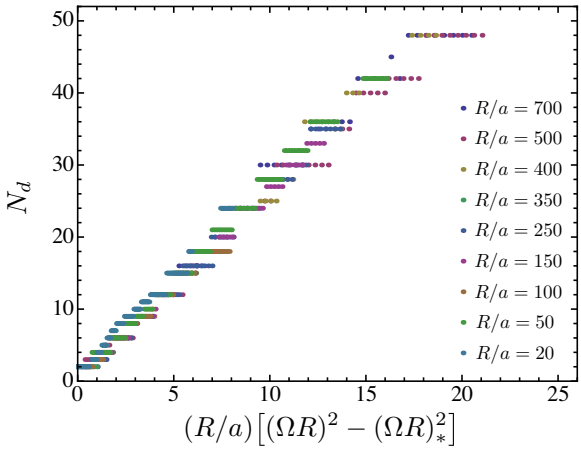

Figure 2.7. Plot of dislocation number vs. scaling prediction, eq. (2.31), for bundle sizes in the range $R/a = 20 - 700$.

Hence, not only do larger bundles become unstable to dislocations at smaller values of bundle twist, the growth of the optimal number of dislocations with "excess" twist in large bundles is also more rapid than in smaller bundles.

In Fig. 2.7 we compare the total dislocation number of the numerically-determined ground states to the scaling prediction, eq. (2.31). We find that the scaling prediction agrees well with numerical results over the range of N_d and the large range of bundle sizes explored here, $20 \leq R/a \leq 700$.

2.5 Summary

In summary, we have shown that geometric frustration arising from helical twist in two-dimensionally ordered filament bundles restructures the ground-state packing at intermediate twist by favoring the presence of appropriately oriented, edge dislocations. Based on the continuum theory of disclinations and dislocations in filament bundles, we show that *dislocations* become favorable in the cross section at twist smaller than the critical twist needed to stabilize *5-fold disclinations*. Unlike the case of stable 5-fold disclinations studied previously [33,135], here we find that the threshold for stable dislocations in bundles is highly dependent on the size of the bundle compared to the microscopic inter-filament spacing. Above the threshold single dislocations in twisted bundles, we predict a rich spectrum of low-symmetry ground-state order. Twist-induced stresses in filament

bundles lead to a natural tendency to "polygonalize" the cross-sectional packing, giving rise to low-energy structures where multiple crystalline domains are separated by radially-extending grain boundaries that terminate in the bundle bulk, not unlike the finite-length grain-boundary scars of spherical crystals.

This study is significant in the context of frustrated order because it demonstrates that "neutral" configurations of topological defects may effectively screen "charged", geometrically-induced stresses, like the stresses generated by filament twist in bundles. Previous studies of defects on curved, crystalline membranes, have predicted extended chains dislocations, or scars, only in the presence of excess disclinations that are themselves either forced in by topology [29, 125] or, in the case of a membranes with a free boundary, as the result of energetic coupling to curvature-induced stresses [43,55]. In these cases, the dislocation arrays function to screen the disclination stress more efficiently than the stresses induced by Gaussian curvature. Here, we show that neutral arrays of 5-7 disclination pairs flood the ground-state packing of crystalline bundles well before twist favors the incorporation of excess 5-fold defects. That is, dislocations arrays are also driven into the packing of frustrated materials by the tendency to screen geometrically-induced stresses alone. Due to the formal relationship between the non-linear elasticity of twisted bundles and curved, crystalline membranes, we expect that the novel grain-boundary geometries predicted here may also occur as ground states of the latter system.

In the context of filamentous materials, the present study is significant for two reasons. First, it identifies ΩR and R/a as the two geometric parameters that govern the ground state packing of helically-twisted bundles. Importantly, we show that the critical degree of twist at which the bundle cross section becomes unstable to topological defects is crucially sensitive to bundle size, R/a. We may relate the reduced twist of the bundle to the tilt angle, θ_{max} of the outermost filament with respect the pitch axis of the helical bundle by, $\theta_{max} = \tan^{-1}(\Omega R)$. For small bundles, less than a few radial filament layers, the critical twist for stability of *any* defect type in the cross section corresponds to a degree of tilt greater than 25°. Because the critical twist decreases with bundle size as $(\Omega R)_* \sim a/R \ln(R/a)$, for bundles that are macroscopically large compared to filament size,

say $R = 100a$, the critical degree of filament tilt is markedly reduced to nearly 9°. For comparison, we note the helical twist of certain collagen fibrils is in the range $15 - 17^\circ$ of helical tilt [35, 56].

The case of collagen points to the second important result regarding the structure of optimally-packed twisted fibers. In many tissue types, collagen fibrils form with lateral dimensions hundreds of times larger than the roughly 1 nm scale of constituent filaments, making multiple dislocations energetically favorable even in fibrils of relatively modest twist. Notably the precise nature of the cross-sectional ordering of collagen molecules in fibrils is a long-standing and open question, in part, due to small-angle scattering data that suggest cross sections are composed of unknown superpositions of crystalline inter-molecular order and disordered inter-molecular packing of some type. Numerous models have been proposed to infer the real-space packing [57], many of which mix aspects of crystalline and non-crystalline order in novel ways [58]. To date, the model most consistent with observed features of x-ray scattering data was proposed by Hulmes, Wess, Prockop and Fratzl [59]. In this model, multiple crystalline domains in a cylindrical bundles are separated by grain boundaries extending radially from a central, low-density region to the surface of the fibril. Remarkably, this model is very similar in gross structure to the ground states of twisted bundles predicted for large bundles of intermediate twist (for example in Fig. 2.4). Though this model of collagen fibril packing did not take into account the effects of twist explicitly, we believe many of the key features of the "disordered" packing of these materials may be understood as crucial elements of energy-minimizing packings of twisted bundles. Future work will explore the form factor of ideal packings of twisted bundles and critically test the intriguing and putative connection between defects in the ground states of twisted bundles and the disorder in the collagen fibril.

2.6 Appendix: Relations for stress, strain and displacement fields of defects

Disclination: The induced stress for a single disclination satisfies bi-harmonic equation, $\nabla^4 \chi = 0$, and exhibit a solution [136]:

$$\chi_i = \sum_{n=0} \left[C_n r^n \cos(n\phi) + D_n r^{n+2} \cos(n\phi) \right] . \tag{2.32}$$

with $C_0 = C_1 = 0$. But for $D_n, n \geq 2$. D_n coefficient calculated in the appendix B section of [136] are:

$$
\begin{aligned}
D_{n\geq 2} &= \frac{1}{R^{n+2}} \left(\frac{\rho}{R}\right)^n \left(\frac{R^2}{n} - \frac{\rho^2}{n+1}\right) && (2.33)\\
d_0 &= -\ln R - 1/2 - \frac{\rho^2}{2R^2} && (2.34)\\
d_1 &= \frac{\rho}{R^2} - \frac{\rho^3}{2R^4} && (2.35)
\end{aligned}
$$

From the Boundary condition $\chi|_{r=R} - R\partial_r \chi_{r=R} = 0$ We can find:

$$
\left(2C_n r^n = r\partial_r \chi^n_{d,>} - (n+2)\chi^n_{d,>}\right)_{r=R} \tag{2.36}
$$

Where $\chi_{d,>}$ is the direct stress contribution and calculated in [136]

$$
\chi^{n\geq 2}_{d,>} = (\frac{\rho}{r})^n \left[\frac{r^2}{n(n-1)} - \frac{\rho^2}{n(n+1)}\right] \tag{2.37}
$$

$$
C_n = -\frac{\rho^n}{R^{2n}}(-\frac{\rho^2}{n} + \frac{R^2}{n-1}) \tag{2.38}
$$

The full expression for induced stress using the known coefficient D_n is:

$$
\begin{aligned}
\chi_i^{n\geq 2} &= \sum_{n=2}^{\infty} K \frac{(r\rho)^n}{R^{2n}} \left(-\frac{R^2}{n-1} - \frac{r^2\rho^2}{(n+1)R^2} + \frac{r^2+\rho^2}{n}\right)\cos(n\phi)\\
\chi_i^{n=0,1} &= K\left(-r^2\left(1/2 + \frac{\rho^2}{2R^2} + \ln R\right) + r^3\cos\phi\left(\frac{\rho}{R^2} - \frac{\rho^3}{2R^4}\right)\right) && (2.39)
\end{aligned}
$$

Where $K = K_0 s/8\pi$ where s is the topological charge of the disclination. Now we can calculate radial and azimuthal component of the stress field using:

$$\sigma_{rr} = r^{-2}\partial_\phi^2\chi + r^{-1}\partial_r\chi, \tag{2.40}$$

$$\sigma_{\phi\phi} = \partial_r^2\chi \tag{2.41}$$

$$\sigma_{r\phi} = -\partial_r(r^{-1}\partial_\phi\chi) \tag{2.42}$$

$$\sigma_{rr} = \sum_{n=2}^{\infty} K\frac{r^{n-2}}{nR^{2(n+1)}}\rho^n\Big[nR^2(\rho^2+n(R^2-\rho^2)) - (n-2)r^2\left(R^2(n+1)-n\rho^2\right)\Big]\times \cos(n\phi) \tag{2.43}$$

$$\sigma_{\phi\phi} = -\sum_{n=2}^{\infty} K\frac{r^{n-2}}{nR^{2(n+1)}}\rho^n\Big[nR^2\left(\rho^2+n(R^2-\rho^2) - (2+n)r^2\left((n+1)R^2-n(\rho^2)\right)\right)\Big]\times \cos(n(\phi)) \tag{2.44}$$

Strain-stress relations are given by:

$$u_{rr} = \frac{1}{K}(\sigma_{rr} - \nu\sigma_{\phi\phi}), \tag{2.45}$$

$$u_{\phi\phi} = \frac{1}{K}(\sigma_{\phi\phi} - \nu\sigma_{rr}), \tag{2.46}$$

$$u_{r\phi} = \frac{1+\nu}{K}\sigma_{r\phi}. \tag{2.47}$$

First we focus on radial components:

$$u_{rr}^{n\geq 2} = \frac{\rho^n r^{n-2}\cos n\phi}{nR^{2(n+1)}}\left[nR^2(\nu+1)\left(\rho^2+n(R^2-\rho^2)\right) - r^2\left((n+1)R^2-n\rho^2\right)(n-2+(2+n)\nu)\right] \tag{2.48}$$

$$u_{rr}^{n=0,1} = (3\nu-1)\bar{r}\bar{\rho}\left(\bar{\rho}^2-2\right)\cos\phi + (\nu-1)\left(1+\bar{\rho}^2+2\ln R\right) \tag{2.49}$$

After summation for $u_{rr}^{n\geq 2}$ we find:

$$\begin{aligned} u_{rr}^{n\geq 2} &= Re\Bigg[\frac{e^{i\phi}\bar{\rho}}{\left(1-e^{i\phi}\bar{\rho}\bar{r}\right)^2}\Bigg(2\bar{r}(\nu-1)+e^{2i\phi}\bar{r}\bar{\rho}^2\Big[\bar{r}^2(3\nu-1)\left(2-\bar{\rho}^2\right)-(\nu+1)\Big]+ \\ & e^{i\phi}\ \bar{\rho}\Big[(\nu+1)\left(2-\bar{\rho^2}\right)+\bar{r}^2\left(3(1-3\nu)+4\nu\bar{\rho}^2\right)\Big]\Bigg)+2(\nu-1)\ln\left(1-e^{i\phi}\bar{\rho}\bar{r}\right)\Bigg] \end{aligned} \tag{2.50}$$

Second for azimuthal components we have:

$$u_{\phi\phi}^{n\geq 2} = -\frac{\rho^n r^{n-2}\cos n\phi}{nR^{2(n+1)}}\left[nR^2(\nu+1)\left(\rho^2+n(R^2-\rho^2)\right)-r^2\left((n+1)R^2-n\rho^2\right)(n+2+(n-2)\nu)\right] \tag{2.51}$$

$$u_{\phi\phi}^{n=0,1} = -\ (\nu-3)\bar{r}\bar{\rho}\left(\bar{\rho}^2-2\right)\cos\phi+(\nu-1)\left(1+\bar{\rho}^2+2\ln R\right) \tag{2.52}$$

After summation for $u_{\phi\phi}^{n\geq 2}$ we find:

$$\begin{aligned} u_{\phi\phi}^{n\geq 2} &= Re\Bigg[\frac{e^{i\phi}\bar{\rho}}{\left(1-e^{i\phi}\bar{\rho}\bar{r}\right)^2}\Bigg(2\bar{r}(\nu-1)+e^{2i\phi}\bar{r}\bar{\rho}^2\Big[\bar{r}^2(\nu-3)\left(2-\bar{\rho}^2\right)+(\nu+1)\Big]- \\ & e^{i\phi}\ \bar{\rho}\Big[(\nu+1)\left(2-\bar{\rho^2}\right)+\bar{r}^2\left(3(\nu-3)+4\bar{\rho}^2\right)\Big]\Bigg)+2(\nu-1)\ln\left(1-e^{i\phi}\bar{\rho}\bar{r}\right)\Bigg] \end{aligned} \tag{2.53}$$

Now by integrating the strain we can find the displacement field, $u_r=\int u_{rr}dr$:

$$u_r=\frac{\rho^n r^n\cos n\phi}{nR^{2(n+1)}}\left[\frac{nR^2(\nu+1)\left(\rho^2+n(R^2-\rho^2)\right)}{r(n-1)}+\frac{-r\left((n+1)R^2-n\rho^2\right)(n-2+(2+n)\nu)}{n+1}\right] \tag{2.54}$$

After summation we have:

$$
\begin{aligned}
u_r &= Re\Bigg[\frac{1}{2\left(e^{i\phi}r\rho - R^2\right)}\Bigg(r\rho\Bigg[(\nu-3)\left(2\rho - e^{i\phi}r\bar{\rho}^2\right) - 4(\nu-1)e^{i\phi}r\Bigg] \\
&+ e^{2i\phi}r\rho^2\left[-2(\nu+1)(1-\bar{\rho}^2) + (3\nu-1)\bar{r}^2(2-\bar{\rho}^2)\right] \\
&+ 4\ln\left(1 - \frac{e^{i\phi}r\rho}{R^2}\right)\left(R^2 - e^{i\phi}r\rho\right)\Bigg[-(\nu-1)r + (\nu-1)\rho\cos\phi + 2i\rho\sin\phi\Bigg]\Bigg)\Bigg]
\end{aligned} \tag{2.55}
$$

$$
u_r^{0,1} = \frac{1}{2}(3\nu-1)\bar{r}^2\rho\left(\bar{\rho}^2 - 2\right)\cos\phi + (\nu-1)r\left(1 + \bar{\rho}^2 + 2\ln R\right) \tag{2.56}
$$

where we define, $\bar{r} = r/R$ and $\bar{\rho} = \rho/R$ and $u_r^{0,1}$ is for $n = 0, 1$ contribution and Re is the real part of an expression. For azimuthal component by integrating the strain we can find the displacement field, $u_\phi = \int r u_{\phi\phi} - u_r d\phi$:

$$
u_\phi = -\frac{\rho^n r^n \sin n\phi}{nR^{2(n+1)}}\left[\frac{nR^2(\nu+1)\left(\rho^2 + n(R^2-\rho^2)\right)}{r(n-1)} + \frac{-r\left((n+1)R^2 - n\rho^2\right)\left(n + 4 + (1+\nu)n\right)}{n+1}\right] \tag{2.57}
$$

After summation we have:

$$
\begin{aligned}
u_\phi &= Im\Bigg[\frac{1}{2\left(e^{i\phi}r\rho - R^2\right)}\Bigg(r\rho\Bigg[(\nu-3)\left(2\rho - e^{i\phi}r\bar{\rho}^2\right) + 8e^{i\phi}r\Bigg] \\
&+ e^{2i\phi}r\rho^2\left[2(\nu+1)(1-\bar{\rho}^2) + (\nu+5)\bar{r}^2(2-\bar{\rho}^2)\right] \\
&+ \ln\left(1 - \frac{e^{i\phi}r\rho}{R^2}\right)\left(R^2 - e^{i\phi}r\rho\right)\Bigg[-4e^{i\phi}r - (\nu-3)\rho + e^{2i\phi}\rho(\nu+1)\Bigg]\Bigg)\Bigg]
\end{aligned} \tag{2.58}
$$

$$
u_\phi^{01} = -\frac{1}{2}(\nu+5)\bar{r}^2\rho\left(\bar{\rho}^2 - 2\right)\sin\phi \tag{2.59}
$$

where Im is imaginary part of an expression. Now calculating the direct term using the Airy stress:

$$
\chi_d = \frac{K}{2}r'^2\ln r'^2 \tag{2.60}
$$

where $r'^2 = r^2 + \rho^2 - 2\rho r\cos\phi$. for radial component of stress and strain we have:

$$\sigma^d_{rr}/K = \frac{r'^2+\rho^2(1-\cos 2\phi)}{r'^2}+\ln r'^2 \tag{2.61}$$

$$\sigma^d_{\phi\phi}/K = \frac{3r'^2-2\rho^2\sin\phi^2}{r'^2}+\ln r'^2 \tag{2.62}$$

$$\sigma^d_{r\phi}/K = \frac{2\sin\phi\,(\rho\cos\phi-r)\,\rho}{r'^2} \tag{2.63}$$

$$u^d_{rr} = -(\nu-3)-2(\nu+1)\frac{(r-\rho\cos\phi)^2}{r'^2}-(\nu-1)\ln(r'^2) \tag{2.64}$$

$$u^d_{\phi\phi} = -(\nu-3)-2(\nu+1)\frac{(\rho\sin\phi)^2}{r'^2}-(\nu-1)\ln(r'^2) \tag{2.65}$$

$$u^d_{r\phi} = \frac{2(\nu+1)\sin\phi\,(\rho\cos\phi-r)\,\rho}{r'^2} \tag{2.66}$$

$$\begin{aligned} u^d_r &= (\nu-1)\left[2r+2\rho\sin\phi\arctan\left(\frac{\rho\cos\phi-r}{\rho\sin\phi}\right)+(\rho\cos\phi-r)\ln r'\right] \\ &- r(3\nu-1)-(\nu+1)\frac{\rho\cos\phi^2}{\sin\phi}\arctan\left(\frac{\rho\cos\phi-r}{\rho\sin\phi}\right) \end{aligned} \tag{2.67}$$

Note: here we define $K = k_0 s/8\pi$ where k_0 is the 2D Young's modulus. where following integrals has been used to calculate u_r:

$$\int \ln(ax^2+bx+c)dx = \frac{1}{a}\sqrt{4ac-b^2}\arctan\left(\frac{2ax+b}{\sqrt{4ac-b^2}}\right)-2x+(\frac{b}{2a}+x)\ln(ax^2+bx+c) \tag{2.68}$$

$$\int (ax^2+bx+c)^{-1}dx = \frac{2}{\sqrt{4ac-b^2}}\arctan\left(\frac{2ax+b}{\sqrt{4ac-b^2}}\right) \tag{2.69}$$

Second way to find the direct displacement contribution, is finding the stress and strain at r for centered disclination and then displace the disclination to $\hat{x}\rho$ by means of coordinate transformation $\vec{r'} = \vec{r} - \rho\hat{x}$. First we find the stress and strain at r for centered disclination:

$$\chi_d = \frac{K}{2}r^2\ln r^2 \tag{2.70}$$

$$\sigma^d_{rr}/K = 1+\ln r^2 \tag{2.71}$$

$$\sigma^d_{\phi\phi}/K = 3+\ln r^2 \tag{2.72}$$

$$u^d_{rr} = 1-3\nu-(\nu-1)\ln r^2 \tag{2.73}$$

$$u^d_{\phi\phi} = (3-\nu)-(\nu-1)\ln r^2 \tag{2.74}$$

$$\tag{2.75}$$

Coordinate transformation $\vec{r'} = \vec{r} - \rho\hat{x}$ can be obtained by rotating the coordinates with $\cos^2\psi = (\frac{\vec{r'}.\vec{r}}{|\vec{r'}||\vec{r}|})^2 = \frac{(r-\rho\cos\phi)^2}{r'^2}$ which yields:

$$\begin{aligned} u'^d_{rr} &= \cos^2\psi u^d_{rr} + \sin^2\psi u^d_{\phi\phi} \\ &= \left(1 - \frac{(r-\rho\cos\phi)^2}{r'^2}\right)\left(3-\nu-(\nu-1)\ln r'^2\right) + \frac{(r-\rho\cos\phi)^2}{r'^2}\left(1-3\nu-(\nu-1)\ln r'^2\right) \end{aligned} \tag{2.76}$$

$$\begin{aligned} u'^d_{\phi\phi} &= \sin^2\psi u^d_{rr} + \cos^2\psi u^d_{\phi\phi} \\ &= \left(1 - \frac{(r-\rho\cos\phi)^2}{r'^2}\right)\left(1-3\nu-(\nu-1)\ln r'^2\right) + \frac{(r-\rho\cos\phi)^2}{r'^2}\left(3-\nu-(\nu-1)\ln r'^2\right) \end{aligned} \tag{2.77}$$

with some manipulations u'^d_{rr} and $u'^d_{\phi\phi}$ gives the same result as Eqs. (30, 31).

Dislocation: Dislocation stress, strain and displacement field can be constructed by superposition of the fields of two disclination with opposite topological charge $s = \pm$ at cylindrical coordinates $\rho^{\pm} = \rho \pm \delta\rho/2$ and $\phi^{\pm} = \phi \pm \delta\phi$ where $\delta\rho$ and $\delta\phi/2$ are small (Here $\delta\rho$ is proportional to the the radial component of the dislocation's orientation vector $\vec{a}$). Superposing and expanding the strain of two disclination with $s = \pm$ at coordinates, $\rho \pm \delta\rho/2$ and $\phi \pm \delta\phi/2$ and keeping term to the lowest order in $\delta\phi$ and $\delta\rho$ we have:

$$\begin{aligned} u^{Disl.,n\geq 2}_{rr} &= \sum_{n=2}^{\infty} -\frac{r^{n-2}\rho^n s\delta\phi\sin(n\phi)}{R^{2(n+1)}}\Big[nR^2(\nu+1)\left(\rho^2 + n\left(R^2-\rho^2\right)\right) \\ &- r^2\left(R^2 + n\left(R^2-\rho^2\right)\right)\left(n-2+(n+2)\nu\right)\Big) \\ &+ \frac{r^{n-2}\rho^{n-1}s\delta\rho\cos(n\phi)}{R^{2(n+1)}}\Big(R^2(\nu+1)\left(n^2R^2 - \left(n^2+n-2\right)\rho^2\right) \\ &- r^2\left(R^2 - 2\rho^2 + n\left(R^2-\rho^2\right)\right)\left(n-2+(n+2)\nu\right)\Big] \end{aligned} \tag{2.78}$$

$$u^{Disl.n=0,1}_{rr} = \frac{\delta\rho s}{R^2}\left(2(\nu-1)\rho - r\cos\phi(3\nu-1)\left(2-3\bar{\rho^2}\right)\right) - s\delta\phi\bar{r}\bar{\rho}(3\nu-1)\left(\bar{\rho}^2-2\right)\sin\phi \tag{2.79}$$

$$
\begin{aligned}
u_{\phi\phi}^{Disl.,n\geq 2} &= \sum_{n=2}^{\infty} \frac{r^{n-2}\rho^n s\delta\phi\sin(n\phi)}{R^{2(n+1)}}\Big(nR^2(\nu+1)\left(\rho^2+n\left(R^2-\rho^2\right)\right) \\
&- r^2\left(R^2+n\left(R^2-\rho^2\right)\right)(n+2+(n-2)\,\nu)\Big) \\
&+ \frac{r^{n-2}\rho^{n-1}s\delta\rho\cos(n\phi)}{R^{2(n+1)}}\Big(R^2(\nu+1)\left(-n^2R^2+\left(n^2+n-2\right)\rho^2\right) \\
&- r^2\left(R^2-2\rho^2+n\left(R^2-\rho^2\right)\right)(n+2+(n-2)\,\nu)\Big)
\end{aligned} \tag{2.80}
$$

$$
u_{\phi\phi}^{Disl.n=0,1} = \frac{\delta\rho s}{R^2}\Big(2(\nu-1)\rho - r\cos\phi(\nu-3)\left(2-3\bar{\rho^2}\right)\Big) - s\delta\phi\bar{r}\bar{\rho}(\nu-3)\left(\bar{\rho}^2-2\right)\sin\phi \tag{2.81}
$$

For the displacement components in radial and azimuthal direction we have:

$$
\begin{aligned}
u^{Disl.,n\geq 2}_{r,a_r} &= \frac{r^n\rho^{n-1}s\delta\rho\cos(n\phi)}{R^{2(n+1)}}\Bigg(\frac{R^2(\nu+1)\left[n^2(R^2-\rho^2)-(n-2)\rho^2\right]}{(n-1)r} \\
&- \frac{r\left(n(\nu+1)+2(\nu-1)\right)\left[n(R^2-\rho^2)+R^2-2\rho^2\right]}{n+1}\Bigg)
\end{aligned} \tag{2.82}
$$

$$
\begin{aligned}
&= Re\Bigg[\frac{a_r\bar{r}\bar{\rho}}{2\left(-e^{i\phi}\bar{r}\bar{\rho}+1\right)^2}\Bigg[(\nu-3)\left(-2+3e^{i\phi}r\bar{\rho}\right)+e^{3i\phi}\bar{r}\bar{\rho}\left(2-3\rho^2\right)\left[\bar{r}^2(3\nu-1)-2(\nu+1)\right] \\
&+ 2e^{2i\phi}\left(3(\nu+1)+\bar{r}^2\bar{\rho}^2(1+5\nu)-4\nu\bar{r}^2-4(\nu+1)\bar{\rho}^2\right)\Bigg] \\
&- e^{-i\phi}a_r\left(\nu-3+(\nu+1)e^{2i\phi}\right)\ln\left(1-e^{i\phi}\bar{r}\bar{\rho}\right)\Bigg]
\end{aligned} \tag{2.83}
$$

$$
\begin{aligned}
u^{Disl.,n\geq 2}_{r,a_\phi} &= \frac{-2r^n\rho^{n-}s\delta\phi\sin(n\phi)}{R^{2(n+1)}}\Bigg(\frac{R^2(\nu+1)\left[\rho^2+n(R^2-\rho^2)\right]}{(n-1)r} \\
&- \frac{r\left(n(\nu+1)+2(\nu-1)\right)\left[n(R^2-\rho^2)+R^2\right]}{n+1}\Bigg)
\end{aligned} \tag{2.84}
$$

$$
\begin{aligned}
&= Im\Bigg[\frac{a_\phi\bar{r}\bar{\rho}}{2\left(-e^{i\phi}\bar{r}\bar{\rho}+1\right)^2}\Bigg[(\nu-3)\left(-2+3e^{i\phi}r\bar{\rho}\right)+e^{3i\phi}\bar{r}\bar{\rho}\left(\rho^2-2\right)\left[\bar{r}^2(3\nu-1)-2(\nu+1)\right] \\
&+ 2e^{2i\phi}\left(3(\nu+1)+\bar{r}^2\bar{\rho}^2(3\nu-1)-4\nu\bar{r}^2-2(\nu+1)\bar{\rho}^2\right)\Bigg] \\
&+ e^{-i\phi}a_\phi\left(3-\nu+(\nu+1)e^{2i\phi}\right)\ln\left(1-e^{i\phi}\bar{r}\bar{\rho}\right)\Bigg]
\end{aligned} \tag{2.85}
$$

$$
u^{Disl.n=0,1}_r = \frac{a_r r}{2R^2}\left(4(\nu-1)\rho-r\cos\phi(3\nu-1)\left(2-3\bar{\rho^2}\right)\right)-2a_\phi\bar{r}(3\nu-1)\left(\bar{\rho}^2-2\right)\sin\phi \tag{2.86}
$$

where we used the following geometric definitions, $s\delta\phi\rho = a_\phi$, $s\delta\rho = a_r$ and $'s'$ is the magnitude of the topological charge, hence a_ϕ, a_r are the radial and azimuthal components of the Burgers vector respectively.

$$u_{\phi,a_r}^{Disl.,n\geq 2} = - \frac{r^{n-1}\rho^{n-1}s\delta\rho\sin(n\phi)}{R^{2(n+1)}}\Bigg(\frac{R^2(\nu+1)\big[n^2(R^2-\rho^2)-(n-2)\rho^2\big]}{(n-1)} - \frac{r^2\left(4+n(1+\nu)\right)\left[n(R^2-\rho^2)+R^2-2\rho^2\right]}{n+1}\Bigg) \tag{2.87}$$

$$\begin{aligned} &= Im\Bigg[\frac{a_r\bar{r}\bar{\rho}}{2\left(-e^{i\phi}\bar{r}\bar{\rho}+1\right)^2}\Bigg[-2(\nu-3)\left(-2+3e^{i\phi}r\bar{\rho}\right) \\ &+ e^{3i\phi}\bar{r}\bar{\rho}\left(2-3\rho^2\right)\left[\bar{r}^2(5+\nu)-2(\nu+1)\right] \\ &+ 2e^{2i\phi}\Big(-(\nu+1)(3-4\bar{\rho}^2)+\bar{r}^2\left[2(1-\rho^2)(\nu+3)-\rho^2(\nu+1)\right]\Big)\Bigg] \\ &+ e^{-i\phi}a_r\left(3-\nu+(\nu+1)e^{2i\phi}\right)\ln\left(1-e^{i\phi}\bar{r}\bar{\rho}\right)\Bigg] \end{aligned} \tag{2.88}$$

$$u_{\phi,a_\phi}^{Disl.,n\geq 2} = -\frac{2r^{n-1}\rho^n s\delta\phi\cos(n\phi)}{R^{2(n+1)}}\Bigg(\frac{R^2(n-2)(\nu+1)\big[n(R^2-\rho^2)+\rho^2\big]}{(n-1)} - \frac{r^2\left(4(1-\nu)+n(2+n+(n-2)\nu)\right)\left[n(R^2-\rho^2)+R^2\right]}{(n+1)n}\Bigg) \tag{2.89}$$

$$\begin{aligned} &= Re\Bigg[\frac{a_\phi\bar{r}}{2\left(-e^{i\phi}\bar{r}\bar{\rho}+1\right)^2}\Bigg[8e^{i\phi}\bar{r}(\nu-1)+(\nu-3)\left(-2\bar{\rho}+3\bar{r}\bar{\rho}^2e^{i\phi}\right) \\ &+ e^{3i\phi}\bar{r}\bar{\rho}^2\left[\bar{r}^2(5\nu-7)(2-\bar{\rho}^2)+2(\nu+1)\bar{\rho}^2\right] \\ &- 2\bar{\rho}e^{2i\phi}\Big((\nu+1)-\bar{r}^2\bar{\rho}^2(\nu-3)+4\bar{r}^2(2\nu-3)\Big)\Bigg] \\ &- 2a_\phi\left((\cos\phi-2\frac{r}{\rho})(\nu-1)+2i\bar{\rho}\sin\phi\right)\ln\left(1-e^{i\phi}\bar{r}\bar{\rho}\right)\Bigg] \end{aligned} \tag{2.90}$$

$$u_\phi^{Disl.n=0,1} = \bar{r}^2(5+\nu)\left[\frac{a_r\sin\phi}{2}\left(2-3\bar{\rho}^2\right)-\frac{a_\phi\cos\phi}{2}\left(\bar{\rho^2}-2\right)\right] \tag{2.91}$$

For the direct terms from Eqs. (33, 34) for the disclination dipole after expansion we have:

$$
\begin{aligned}
u_{rr}^{Disl.,d} &= \frac{2a_r}{r'^4}\Big(r^2\rho(3+\nu)-\rho^3(\nu-1)+r\cos\phi\left[r^2(\nu-1)+\rho^2(\nu-5)\right] \\
&+ 2r\rho\cos^2\phi\left[(\nu+1)\rho\cos\phi-2r\nu\right]\Big) \\
&- \frac{2a_\phi\sin\phi}{r'^4}\Big(r^3(\nu-1)+2r\rho^2(1+2\nu)-2\cos\phi\left[2r^2\nu+(\nu+1)\rho^2\right]+r\rho^2(1+\nu)\cos 2\phi\Big)
\end{aligned} \tag{2.92}
$$

$$
\begin{aligned}
u_{\phi\phi}^{Disl.,d} &= \frac{a_r}{r'^4}\Big(r\cos\phi\left[2r^2(\nu-1)+(7\nu-5)\rho^2\right]+2\rho\left[r^2(1-3\nu)+\rho^2(1-\nu)\right] \\
&+ 4\rho r^2\cos 2\phi-\rho^2 r(1+\nu)\cos 3\phi\Big) \\
&+ \frac{2a_\phi\sin\phi}{r'^4}\Big(-r^3(\nu-1)+2r\rho^2(2+\nu)-2\rho\cos\phi\left[2r^2+(\nu+1)\rho^2\right]+r\rho^2(1+\nu)\cos 2\phi\Big)
\end{aligned} \tag{2.93}
$$

where we define $r'^2 = r^2+\rho^2-2\rho r\cos\phi$. Finally we also free to add the rigid body translation-rotation terms to displacement fields,

$$
u_r^{RT} = A\cos\phi + B\sin\phi \tag{2.94}
$$

$$
u_\phi^{RT} = -A\sin\phi + B\cos\phi + Cr \tag{2.95}
$$

where A, B, C are arbitrary constants due to the rotation and translation of the system.

CHAPTER 3

CONTINUUM THEORY OF SCARRED MEMBRANES

3.1 Introduction

We study the structural features and underlying principles of multi-dislocation ground states of a crystalline spherical cap. In the continuum limit where the ratio of crystal size to lattice spacing W/a diverges, dislocations proliferate and ground states approach a characteristic sequence of structures composed of radial grain boundaries ("neutral scars"), extending radially from the boundary and terminating in the bulk. Employing a combination of numerical simulations and asymptotic analysis of continuum elasticity theory, we prove that an energetic hierarchy gives rise to a structural hierarchy, whereby dislocation number and scar number diverge as $a/W \to 0$ while scar length and dislocation number per scar become *independent* of lattice spacing. We characterize a secondary transition occurring as scar length grows, where the n-fold scar symmetry is broken and ground states are characterized by polydisperse, forked-scar morphologies.

Understanding the ground-state order of curved, 2D crystals remains an outstanding challenge with far ranging implications, from the assembly of viral capsids [109, 140] and multi-component lipid membranes [113, 118] to the structure and stability of particle coated-droplets [119]. The planar, six-fold, equitriangular packing favored by isotropic interactions is incompatible with Gaussian curvature and as a consequence, topological defects are necessary features of ground-state order in curved crystals [122, 123]. The importance of *disclinations* — points of localized 5- or 7-fold symmetry — has long been recognized for crystals on fixed-topology surfaces, like the well-known Thomson problem [124, 125]. More recently, experimental [119, 126], computational [127, 128] and theoretical [129–131] studies have begun to recognize the importance of a related class of defects, *dislocations* — "neutral" 5-7 dipoles — in the minimal-energy states of curved crystals, both with and without disclinations. Unlike disclinations, the number of dislocations, N_d, in curved-crystal

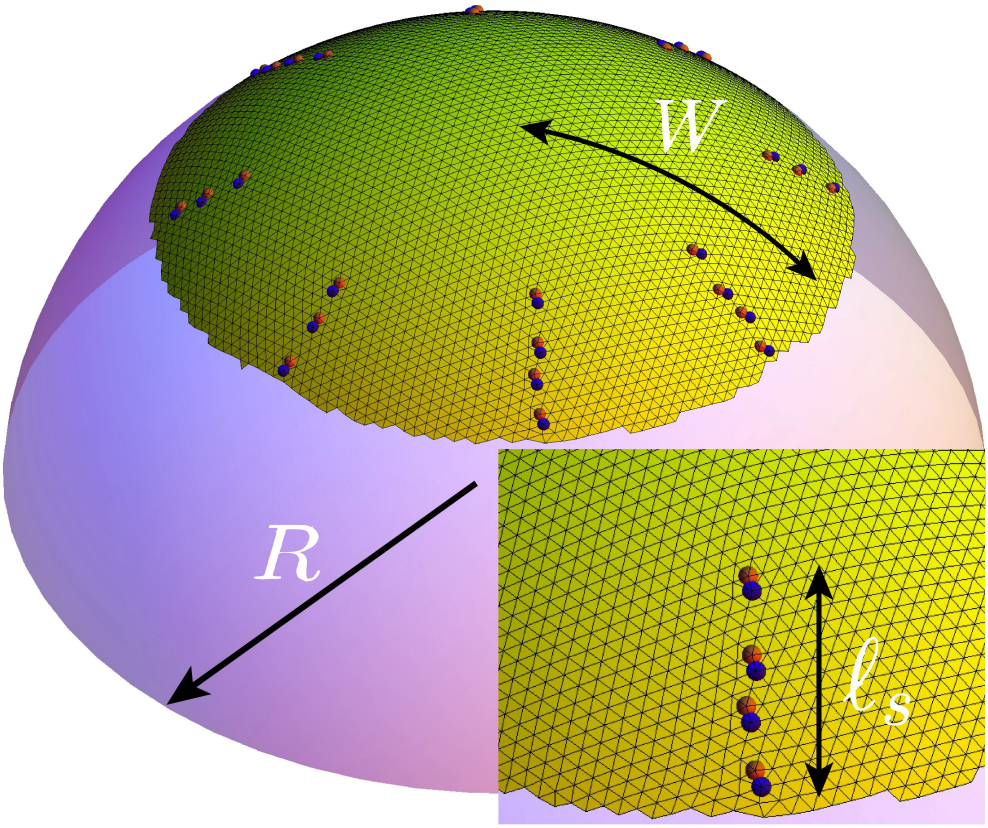

Figure 3.1. Mesh reconstruction of an 8-scar ground state of a crystalline cap bound to sphere of radius R, where 5-7 dislocation "dipoles" are shown as red and blue vertices.

ground states grows arbitrarily large in the continuum limit — where W/a the ratio crystal size to lattice spacing diverges — resulting in multi-dislocation chains, known as "scars" [119, 129], that span large portions of the crystal. While heuristic arguments have been proposed to explain the scaling of the total number of dislocations with surface curvature [126, 129], to date there is little understanding of precisely how defects are arranged in multi-dislocation ground states and what mechanical, geometric and microscopic parameters govern these emergent structures.

In this chapter, we study a continuum elasticity model of crystalline caps bound to a spherical substrate to illuminate the emergent structure of mutli-dislocation ground states in the continuum limit. A combination of numerical and asymptotic analysis prove that as $N_d \to \infty$ the arrangement approaches a characteristic pattern: n_s radially-oriented scars extending from the crystal edge terminating in the bulk (Fig. 3.1). An energetic hierarchy underlies the structural hierarchy

characterizing these states, which was recently argued [132] to parallel mechanisms of elastic pattern formation in wrinkled ultra-thin films [133,134], whereby certain features of the defect pattern (N_d and scar length, ℓ_s) are encoded in the mechanics of the asymptotic limit of vanishing lattice spacing, while other features (optimal scar number n_s) are governed by imperfect relaxation of geometric stresses by discrete dislocations.

It has been shown in [132] how "far-from-threshold" analysis developed originally to study emergent patterns of wrinkles in thin elastic sheets, far from buckling threshold [121, 134] can be extended to scarred crystalline sheets. Key features of emergent pattern of symmetric dislocation scars (*e.g.* the length of defective zone in analogy to wrinkle length) on curved crystalline sheets can be explained with common basis that underlies the compression-free states in wrinkled thin sheets. This approach was developed in the well-behaved continuum limit, $b/W \to 0$ and small confinement, of highly defective state for the case of scarred sheets, which is analogous to highly bendable wrinkled elastic sheet with vanishingly small thickness $t \to 0$. The formalism was developed for the small confinement limit where predictions was limited to the defect morphologies described by narrow scarred zone close to the boundary. Here, first we generalize and extend that framework to the arbitrary confinement, including singular limit of infinite confinement, in which geometric strains control the emergent pattern of complex scar morphology. Second, we demonstrate that optimal symmetry of n-fold defect patterns is selected by a competition between the distinct energetics associated with different parts of the scars, their respective *lengths* and *ends*. Remarkably, this reveals that the asymptotic approach to the continuum limit is characterized by the divergence of *both* the number of dislocations *and scars*, such that N_d/n_s, the number of dislocations per scar, approaches a universal constant, independent of lattice spacing and defect core energy. Finally, we present numerical evidence that the principles of this energetic hierarchy remain intact when caps are driven through a secondary structural transition which breaks the n-fold symmetry of the defect pattern.

3.2 Effective theory of multi-dislocation ground-state

3.2.1 Multi-scar energetics

We begin with the effective elastic energy of multi-dislocation patterns of crystalline caps expressed purely in terms of defect positions in the cap. We study a circular 2D crystalline "cap" of radius W bound to a rigid spherical substrate of radius R, subject to an adhesive, radial tension T at its boundary that favors spreading of the cap over the substrate. Our analysis is based on the continuum elasticity theory of 2D crystals, where the total energy is

$$E = \frac{1}{2}\int dA\sigma_{ij}u_{ij} - T\Delta A. \tag{3.1}$$

we decompose the total stress in two components

$$\sigma_{ij} = \sigma^0_{ij} + \sigma^D_{ij}, \tag{3.2}$$

where σ^0_{ij} represents the axisymmetric stress of the cap in the defect-free state and σ^D_{ij} represents stresses generated by defects (distinct from the stress $\sigma^{\rm d}_{ij}$ of the "defect riddled" ground-states. For a weakly-curved crystal, elastic strain derives from in-plane displacement $\mathbf{u}(\mathbf{x})$ (components in xy plane) and out-of-plane defection $h(\mathbf{x})$, with $u_{ij} = (\partial_i u_j + \partial_j u_i + \partial_i h\partial_j h)/2$, while the stress response of a hexagonal crystal is characterize by Lamé constants, λ and μ, $\sigma_{ij} = \lambda\delta_{ij}u_{kk} + 2\mu u_{ij}$. The second term in (4.3) represents the adhesive work where $\Delta A = W\int d\theta\ u_r(r = W)$ is the area change of the sheet, and (r, θ) are polar coordinates. Dislocations are singular points, $\mathbf{x}_\alpha$ around which displacements increases (or decrease) by Burgers vector $\mathbf{b}$, corresponding to a partial row of lattice sites of width $|\mathbf{b}| \simeq a$ added or removed from crystal, terminating at $\mathbf{x}_\alpha$. For a curved crystal possessing dislocations [85], stress is governed by two relations, in-plane force balance, $\partial_i\sigma_{ij} = 0$, and the compatibility equation,

$$Y^{-1}\nabla^2_\perp\sigma_{ii} = -K_G - \nabla_\perp \times \mathbf{b}(\mathbf{x}), \tag{3.3}$$

where $Y = 4\mu(\lambda + \mu)/(\lambda + 2\mu)$ is the 2D Young's modulus, $K_G = R^{-2}$ is the Gaussian curvature, and $\mathbf{b}(\mathbf{x}) = \sum_\alpha \mathbf{b}_\alpha\delta(\mathbf{x} - \mathbf{x}_\alpha)$ is the areal Burgers density. Note that in using eq. (3.6) we assume

the small-slope limit, where $|\nabla_\perp h| \approx W/R \ll 1$ and the cap covers a small (but finite) sphere fraction. In particular, we study coverages smaller than $(W/R)_c = \sqrt{2/3} \simeq 0.82$ beyond which small-slope theory is unstable to excess 5-fold disclinations [135, 136].

The defect free stress field σ^0_{ij}, is the solution of the compatibility equation

$$Y^{-1}\nabla^2_\perp \sigma^0_{ii} = -K_G, \tag{3.4}$$

subject to the boundary condition $\sigma^0_{rr}(r = W) = T$. This part of stress quantifies the cost of frustration of the confined sheet associated with axially symmetric stresses. Stress in defect-free state, σ^0_{ij}, derives from geometric strains imposed by curvature and adhesive forces at the boundary, which require $\sigma_{rr}(r = W) = T$,

$$\sigma^0_{rr} = \frac{Y}{16R^2}(W^2 - r^2) + T;\ \sigma^0_{\theta\theta} = \frac{Y}{16R^2}(W^2 - 3r^2) + T. \tag{3.5}$$

Unlike the radial direction which is always tensile, in the defect-free state for sufficiently small T the hoop direction becomes compressive ($\sigma^0_{\theta\theta} < 0$) at large radii, $r > L_0 = W/\sqrt{3}(1 + 2T/T_*)^{1/2}$, where $T_* = Y/8(W/R)^2$ is a critical tension above which the compressed zone vanishes.

On the other hand the stress distribution in presence of dislocations, σ^D_{ij} is governed by,

$$Y^{-1}\nabla^2_\perp \sigma^D_{ii} = -\nabla_\perp \times \mathbf{b}(\mathbf{x}) = \sum_\alpha (\mathbf{b}_\alpha \times \nabla_\perp)\delta(\mathbf{x} - \mathbf{x}_\alpha), \tag{3.6}$$

where $\mathbf{b} \times \nabla_\perp = \epsilon_{ij} b_i \partial_j$. To maintain fixed total stress at the boundary, σ^D_{ij} satisfies vanishing normal stress at $r = W$. The elastic energy deriving from σ^D_{ij} field encodes both the self-energy of dislocations and the interaction energy between dislocations. These energies were calculated analytically in ref. [137] in terms of the Greens function of the biharmonic equation subject to the vanishing normal stress, where dislocations correspond to 5-7 disclination dipole. The elastic self-energy of a single dislocation at radial position r is

$$E^D_{self}(\mathbf{b}, r) = \frac{Y(\mathbf{b}\cdot\hat{\theta})^2}{8\pi^2}\left(\frac{r}{W}\right)^2 + \frac{Y|\mathbf{b}|^2}{8\pi^2}\left[\ln\left(1 - \frac{r^2}{W^2}\right) - \ln\left(\frac{a}{W}\right) + E_c\right], \tag{3.7}$$

where E_c parameterizes the microscopic energy of the dislocation core (note the expression for *dislocation* self energy, E^D_{self}, should not be confused with the self-energy of *scars*, $E_{\rm self}$). The pairwise elastic interactions between dislocations $\mathbf{b}_1$ and $\mathbf{b}_2$ at respective positions $\mathbf{x}_1$ and $\mathbf{x}_2$ take the form

$$\begin{aligned} E^D_{int}\left(\mathbf{b}_1,\mathbf{x}_1;\mathbf{b}_2,\mathbf{x}_2\right) &= \frac{Y}{4\pi^2}\Bigg[-\frac{(\mathbf{b}_1\cdot\mathbf{b}_2)}{2}(\ln\cos^2\xi+\sin^2\xi) \\ &+ \frac{(\mathbf{r}_1\times\mathbf{b}_1)(\mathbf{r}_2\times\mathbf{b}_2)}{W^2}(1-\cos^4\xi)+\frac{(\mathbf{b}_1\times\boldsymbol{\Delta}\mathbf{x}_{12})(\mathbf{b}_2\times\boldsymbol{\Delta}\mathbf{x}_{21})}{|\boldsymbol{\Delta}\mathbf{x}_{12}|^2}\sin^4\xi \\ &+ \frac{(\mathbf{b}_1\times\boldsymbol{\Delta}\mathbf{x}_{12})(\mathbf{b}_2\times\mathbf{xs}_2)(1-r_1^2/W^2)+(\mathbf{b}_2\times\boldsymbol{\Delta}\mathbf{x}_{21})(\mathbf{b}_1\times\mathbf{x}_1)(1-r_2^2/W^2)}{(W^2-r_1^2)(W^2-r_2^2)+|\boldsymbol{\Delta}\mathbf{x}_{12}|^2}\sin^2\xi\Bigg] \end{aligned} \tag{3.8}$$

where ξ is

$$\cos^2\xi=\frac{|\boldsymbol{\Delta}\mathbf{x}_{12}|^2}{(W^2-r_1^2)(W^2-r_2^2)+|\boldsymbol{\Delta}\mathbf{x}_{12}|^2}. \tag{3.9}$$

The coupling of the dislocation induced stresses to the curvature and tension induced stresses—cross terms $\frac{1}{2}\int dA(\sigma^D_{ij}u^0_{ij}+\sigma^0_{ij}u^D_{ij})-2\pi WTu^D_r(W)$—lead to the "relaxation energy" associated with release of hoop compression from the cap. This energy is equivalently derived from the Peach-Koehler force $f_i(r)=\epsilon_{ij}\sigma_{jk}(r)b_k$ experienced by dislocation subject to stresses σ^0 (and associated boundary forces). The relaxation of defects may be calculated from the "climbing" of a dislocation from the edge at $r=W$ into the cap,

$$E^D_{relax}(r)=b\int_r^W dr'\sigma^0_{\theta\theta}(r')=\frac{YW^2b}{16R^2}r\left[(r/W)^2-1\right]+TWb(1-r/W). \tag{3.10}$$

Hence the total elastic energy of the scarred crystal with N_d dislocations on a curved surface in eq. (1) can be described by

$$E_{tot}=E_0+\sum_{\alpha=2}^{N_d}\sum_{\beta<\alpha}^{N_d}E^D_{int}\left(\mathbf{b}_\alpha,r_\alpha;\mathbf{b}_\beta,r_\beta\right)+\sum_{\alpha=1}^{N_d}E^D_{self}\left(\mathbf{b}_\alpha,r_\alpha\right)+\sum_{\alpha=1}^{N_d}E^D_{relax}\left(\mathbf{b}_\alpha,r_\alpha\right), \tag{3.11}$$

where E_0 is the energy of the defect-free, axisymmetric state,

$$\begin{aligned} E_0 &= \pi \int_0^W \sigma_{ij}^0 u_{ij}^0 - 2\pi W T u_r(W) \\ &= \frac{\pi W^2}{Y}\left((\nu-1)T^2 + TY\frac{W^2}{4R^2} + \frac{1}{384}\frac{Y^2W^4}{R^4}\right). \end{aligned} \tag{3.12}$$

Dislocations corresponding to the removal of a row extending from the defect to the boundary (i.e. $\mathbf{b} = b\hat{\theta}$) relax compression at the edge and lower the elastic energy, provided their cost is sufficiently low. We characterize the susceptibility to dislocations (dubbed the "defectivity" of the crystal [132]) in terms of the ratio of dislocation self-energy, proportional to Yb^2, to elastic energy of the defect-free sheet, proportional to $YW^2(W/R)^4$,

$$\epsilon = (b/W)^2(W/R)^{-4}, \tag{3.13}$$

which vanishes in the continuum limit $b/W \to 0$, indicating the instability of the crystal to dislocations when $T < T_*$.

3.3 Emergent structure of multi-dislocation ground states in curved crystals

3.3.1 Structure of ground-state configurations

We study the structure and energy of multi-dislocation configurations in this regime by superposing σ_{ij}^0 with stresses generated by multiple dislocations ($\mathbf{b}$ aligned to hoop direction). The self-energy of dislocations, dislocation interaction energy, and the energy associated with relaxing geometrically-induced compression derive from the free-boundary condition Greens functions of single dislocations [136, 137] and eq. (4.3). For given values of tension, curvature and b/W, we relax the total energy by numerically adjusting defect position and number in the crystal. For fixed N_d, the energy is minimized by steepest descent starting from $\sim 10^4$ random initial defect configurations. The minimal energy multi-dislocation pattern is selected from this ensemble of "simulated quenches". As T is reduced below T_*, a characteristic multi-dislocation pattern emerges: n_s evenly spaced and symmetric scars extending a distance ℓ_s from the edge into the cap. For conditions

shown in Fig 3.1 ($W = 0.3R$, $b = 0.013W$, $T = 0.1T_*$) we find a $n_s = 8$ scars of average length $\ell_s = 0.45W$, composed of $N_d = 27$ dislocations. While optimal size and number of scars, as well as total defect number, change with both macroscopic (cap size, tension) and microscopic (Burgers vector) parameters, all simulated ground-states show spontaneous emergence of n-fold symmetry at the onset of scar stability, $T < T_*$.

3.3.2 Global features

We now demonstrate how the features of this characteristic dislocation pattern are governed by the distribution of stress approached in the asymptotic limit $b/W \to 0$. The ultimate stress $\sigma^{\rm d}_{ij}$ of the defect-riddled state must be significantly remodeled by dislocations from the defect free stress σ^0_{ij}, which is unstable to defects. The stability of multi-dislocation state can be understood in terms of the Peach-Kohler force [138] on acting on dislocations, $f_i = b\epsilon_{ij}\sigma^{\rm d}_{j\theta}$, which implies that dislocations climbing from the boundary continue to lower the energy until defects are localized to regions where $\sigma^{\rm d}_{r\theta} = \sigma^{\rm d}_{\theta\theta} = 0$. The stable stress pattern derives from the continuum dislocation density $\mathbf{b}_c(\mathbf{x}) = b\rho(r)\hat{\theta}$ that approximates defect distribution in the $N_d \to \infty$, $b \to 0$ limit, and mechanical constraints imposed by a zone of vanishing compression [132]. The axisymmetry of the areal density $\rho(r)$ implies vanishing of shear stress, while the collapse of hoop stress is governed by the solution of eq. (3.6) in two radial zones: a defect-free ($\rho = 0$) *axisymmetric inner region* for $r < L_{\rm d}$ where the stress is identical to eq. (3.5) up to an overall additive constant; and an *outer scarred zone* ($\rho \neq 0$) for $r \geq L_{\rm d}$ where $\sigma^{\rm d}_{\theta\theta} = 0$ as required by defect stability and $\sigma^{\rm d}_{rr} = TW/r$ as required by force balance and boundary conditions. Continuity of radial and hoop components at the edge of scarred zone require an defect-free inner zone of radius

$$L_{\rm d} = W - \ell_s = W(T/T_*)^{1/3}, \tag{3.14}$$

which predicts that scars extend *beyond* the original compressed zone of the defect free state since $L_{\rm d} < L_0$. Like the "far-from-threshold" analysis of wrinkling of ultra-thin elastic sheets [132, 134, 139], the asymptotic stress pattern achieved in a defect-riddled cap in the $b/W \to 0$ limit is independent of "microscopic" features of the pattern, including b and the scar number, n_s.

Given this stable, compression-free pattern of stress, the dislocation distribution is determined by integrating the compatibility relation — matching the discontinuity in $\partial_r \sigma_{ii}^{\rm d}$ at $r = L_{\rm d}$ with the dislocation density at the edge of the scarred zone — yielding

$$\rho(r) = \frac{\epsilon^{-1/2}}{8W^2}\left[4\frac{r}{W} - \frac{T}{T_*}\Big(\frac{W}{r}\Big)^2\right]. \tag{3.15}$$

Integrating $\rho(r)$ over the scarred zone $L_{\rm dr} \geq r \geq W$, the total dislocation number becomes,

$$N_d = \frac{\pi\epsilon^{-1/2}}{12}\Big[4(1 - T/T_*) + (T/T_*)\ln(T/T_*)\Big]. \tag{3.16}$$

At small T, $N_d \sim \epsilon^{-1/2}$ is consistent with the balance of the total edge length removed by dislocations $N_d b$ and shortening of latitudes at the outer boundary imposed by spherical geometry $\sim W(W/R)^2$, while as $T/T_* \to 1$, boundary forces eliminate this compression, hence dislocation number vanishes in this limit $N_d \sim \epsilon^{-1/2}(T_* - T)$.

Notably, the principle of stress-collapse in the scarred zone illustrated here is equivalent to the previously invoked notion of "perfect screening" of Gaussian curvature by dislocations which, for $T = 0$, achieves $\sigma_{ij} = 0$ throughout the sheet [126, 129]. Comparison to numerical simulations demonstrates that the value of the"perfect screening" distribution, and its generalization to non-zero boundary forces, is far more than heuristic, describing certain features of multi-dislocation states (length of scars and defect number) quantitatively, even for finite, but large values of $\epsilon^{-1} \sim (W/b)^2$. In fig. 3.2a-b we compare predictions for ℓ_s and N_d to "free dislocation" simulations, as well as to a much larger class of numerically-optimized, fixed n-fold symmetry radial scar patterns, whose fewer degrees of freedom (radial positions of each dislocation "ring") allow us to reach highly "defective" caps, up to $\epsilon^{-1} \simeq 6 \times 10^4$ and $N_d \approx 250$.

3.3.3 Energetic hierarchy: Scaling of energetics of multi-scar configurations

Unlike the dislocation number and scar length, the optimal scar number does not derive from the asymptotic stress pattern $\sigma_{ij}^{\rm d}$ in the $b/W \to 0$ limit, which is independent of n_s. In [132], it was shown in the limit of narrow scars ($\ell_s/W \ll 1$) that the n_s-degenerate energetics encoded in the

elastic energy of asymptotic stress σ_{ij}^{d} correspond directly to the combination of relaxation energy per scar and the repulsive interactions between scars, which describe respectively the dominant gains and costs of multi-scar patterns. Here, we consider *sub-dominant* costs of the self-energies of scars, in terms of distinct costs attributed to the *ends* and *lengths* of scars, which describe energetics of fine-scale (intra-scar) stresses absent from the continuum limit, and more important, lift the degeneracy of the energy with n_s.

To illustrate the key predictions implied by the scale separation in the continuum limit, we consider the scaling of the energetics multi-scar configurations with n_s. The relaxation energy of derives from the mechanical interaction between dislocation stresses and the initially compressive stress field, σ_{ij}^0. As a dislocation is "pulled" from the cap edge, a length $\sim \ell_s \sim W$ is compressed by b, relaxing energy by $\sim bW\sigma_{\theta\theta}^0(r = W)$, leading to

$$E_{\mathrm{relax}} \approx -bWT_*N_d \sim -E_{\mathrm{axi}}, \tag{3.17}$$

where we used the fact that edge stress is of order T_* and $N_d \sim \epsilon^{-1/2}$ and $E_{\mathrm{axi}} \approx YW^2(W/R)^4$ is the elastic energy scale of the defect-free state. Turning now to elastic interactions between scars, we note that scars differ from ordinary grain boundaries in that the former terminate in the bulk of crystal [129]. Crossing a grain boundary implies rotation of crystal axes by b/d, where d is the dislocation spacing. Hence, scar end are disclination-like singularities, points around which lattice directions rotate rapidly [138], and the far-field stresses generated by scars, and their corresponding interactions, are dominated by the interactions between these end singularities. Interactions between disclinations of equal topological charge s in a crystal of size W acquire elastic cost $\sim Ys^2W^2$ [85]. Estimating dislocation spacing as $d = Wn_s/N_d$ yields and effective disclination charge $s \approx b/d \sim (b/W)(N_d/n_s)$, and summing over all $n_s(n_s - 1)/2 \sim n_s^2$ pairs, the cost of scar interactions becomes

$$E_{\mathrm{int}} \approx Y(N_d b/W)^2 \sim E_{\mathrm{axi}}. \tag{3.18}$$

Like $E_{\rm relax}$, the scar interactions contribute at the dominant scale, $E_{\rm axi}$, and exhibit no dependence on scar number or on the microscopic scale, b, identifying these terms with the elastic energy of the asytomptotic stress pattern $\sigma_{ij}^{\rm dr}$.

Scars differ from ordinary grain boundaries in that the former terminate in the bulk of crystal [129]. Crossing a grain boundary implies rotation of crystal axes by b/D, where D is the dislocation spacing. Hence, scar ends are disclination-like singularities, points around which lattice directions rotate rapidly [138], and the far-field stresses generated by scars are dominated by these end singularities. Estimating dislocation spacing as $D = \ell_s n_s/N_d$ yields and effective disclination charge $s \approx b/D \sim (b/\ell_s)(N_d/n_s)$, and the elastic cost to introduce this charge $\ell_s \approx W$ from the cap edges becomes $\sim Y s^2 W^2$ [85]. In addition to the cost of the singular ends, grain boundary scars are characterized by a "line tension", $\sim Y b^2/D\big[\ln(D/b) + E_c\big]$ [138], where E_c parameterizes the inelastic core energies of dislocations, from which we estimate

$$\begin{aligned} E_{\rm self} &\approx n_s^{-1} Y (N_d b/W)^2 + Y b^2 N_d \ln\Big(\frac{N_d W}{n_s b'}\Big) \\ &\sim E_0\big[n_s^{-1} + \epsilon^{1/2}\ln(n_s\epsilon^{1/2})\big], \end{aligned} \tag{3.19}$$

where b' is a renormalized core size and $E_0 \approx Y(W/R)^4 W^2$. The elastic cost of scar tips favors a large number of low-angle scars, which is balanced by the weaker (or $\epsilon^{1/2}$) preference of line tension for dense scars (small n_s). This sets an optimal scar number $n_s \sim \epsilon^{-1/2} \gg 1$ that diverges in the continuum limit as $W/b \to \infty$. As the dislocation number and scar length vary with T/T_*, we expect more generally that optimal scar number of n_s-fold symmetric states behaves as

$$n_s = \epsilon^{-1/2}\bar{n}_s(T/T_*) \tag{3.20}$$

where $\bar{n}_s(x)$ is dimensionless function which vanishes as $x \to 1$. Assuming n-fold symmetry for all T, we may determine $\bar{n}_s(T/T_*)$ by numerically optimizing self-energy contributions for all T/T_* (see section 3.3.4). This prediction for optimal scar number is compared numerical ground states (both n-fold and "free dislocation" simulations) in Fig. 3.2c, confirming the collapse of optimal

scar number to form of eq. (3.20) as $\epsilon \to 0$. Both dislocation and scar number diverge as $\epsilon^{-1/2}$, implying a universality in the approach to the continuum distribution of dislocations. Remarkably, the number of dislocations per scar $N_d/n_s \equiv M(T/T_*)$ is predicted to approach a constant value for a given ratio T/T_*, *independent* of lattice spacing. As shown in Fig. 3.2d, M is varies weakly with tension, from $M \simeq 1$ as $T \to T_*$, to roughly 6 dislocations per scar in the absence of boundary forces ($T = 0$).

3.3.4 Self-energy of scars revisited

In [132] it was shown for the weak confinement regime ($T \to T_*$), and argued more generally in the last sections, that the subdominant energetics associated with the *self-energies of scars* is responsible for selecting the optimal symmetry of n-fold scar patterns. In the section 3.3.3 a scaling prediction for the n_s dependence was made based on the distinct energetics associated with scar lengths and scar ends. Here, we derive an explicit expression for the self energy contribution of scars in terms of dislocation energetics (self-energies and interactions) which we then minimize numerically with respect to n_s to find a prediction for optimal scar number, $n_s\,(T/T_*)$, for arbitrary value of T/T_*. Because the dominant pattern of stress σ^d_{ij} and continuum limit defect-distribution $\rho(r)$ are independent of n_s, scar number enters the self-energy calculation of scars only through the change in linear density of dislocations along a scar, $\lambda(r)$. Assuming pattern of n_s-fold symmetry we find a local dislocation spacing $D(r) = 1/\lambda(r)$,

$$D(r) = \frac{n_s}{2\pi r \rho(r)}, \tag{3.21}$$

which shows that scars become more diffuse (dense) lengthwise as their number increases (decreases).

The self-energy of a scar derives from the sum of the self-energies of individual dislocations and the sum over all pairwise interactions between dislocations along a single scar. For the case, of parallel dislocation pairs along a single scar, the form of dislocation interaction simplifies to,

$$E^D_{dis}(r_1, r_2) = \frac{Yb^2}{4\pi^2}\Big[-\frac{1}{2}(\ln\cos^2\xi + \sin^2\xi) - \sin^2\xi(1 - r_1 r_2/W^2)\Big], \tag{3.22}$$

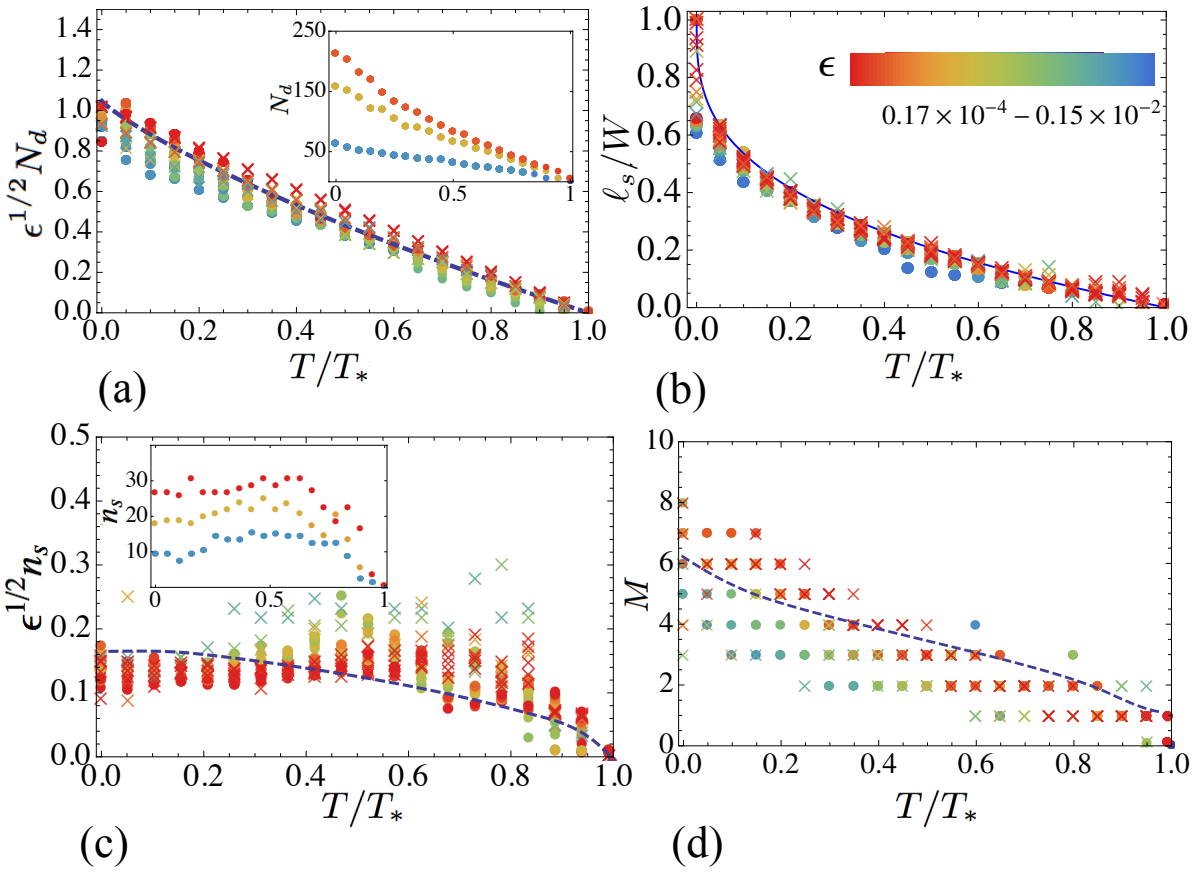

Figure 3.2. The scaled dislocation number $\epsilon^{1/2}N_d$ (a), the length of the scarred zone ℓ_s (b), the scaled scar number $\epsilon^{1/2}n_s$ (c) and the number of dislocations per scar M (d) for simulated ground states of the cap are shown as functions of the reduced tension, T/T_*. Insets of (a) and (c) are unscaled dislocations and scar numbers. Results from unconstrained, "free dislocation" and imposed n-fold symmetric simulations are shown respectively as crosses and filled circles. Color scale of points in (b) correspond to dimensionless dislocaition cost $\epsilon = (b/W)^2(W/R)^{-4}$, where simulations were carried out over a range of cap sizes and curvatures: $W/b = 100 - 1400$ and $W/R = 0.05 - 0.3$. The dashed lines indicate predictions from asymoptotic analysis of dominant and sub-dominant energetics of defect patterns.

where $\cos\xi = W|r_1 - r_2|/(W^2 - r_1 r_2)$. The total contribution from the self-energies of the n_s scars can be written as the summations

$$E_{\rm self}/n_s = \sum_{\alpha=2}^{M}\sum_{\beta<\alpha}^{M} E^D_{int}\left(r_\alpha, r_\beta\right) + \sum_{\alpha=1}^{M} E^D_{self}\left(r_\alpha\right), \tag{3.23}$$

where $M = N_d/n_s$ is the number of dislocation per scar. To approximate the value of the discrete sums along the scar, we replace dislocation self-energies and interaction energies with their *mean values* along intervals of width $D(r_\alpha)$, centered around dislocation positions r_α, allowing us to convert sums to integrals,

$$\begin{aligned} E_{\rm self}/n_s &\cong \sum_{\alpha=2}^{M}\sum_{\beta<\alpha}^{M} \frac{1}{D(r_\beta)} \int_{r_\beta - D(r_\beta)/2}^{r_\beta + D(r_\beta)/2} E^D_{int}\left(r, r_\alpha\right) dr + \sum_{\alpha=1}^{M} \frac{1}{D(r_\alpha)} \int_{r_\alpha - D(r_\alpha)/2}^{r_\alpha + D(r_\alpha)/2} E^D_{self}\left(r\right) dr \\ &\cong \sum_{\alpha=2}^{M} \int_{r_\alpha + D(r_\alpha)/2}^{W + D(W)/2} \lambda(r) E^D_{dis}\left(r, r_\alpha\right) dr + \int_{L - D(L)/2}^{W + D(W)/2} \lambda(r) E^D_{self}\left(r\right) dr \\ &= \int_L^W \lambda(r')dr' \int_{r' + D(r')/2}^{W} \lambda(r) E^D_{int}\left(r, r'\right) dr + \int_L^W \lambda(r, T/T_*) E^D_{self}\left(r\right) dr, \end{aligned} \tag{3.24}$$

where we have dropped $\pm D/2$ corrections to the range of integration the ends of scars $r = L$ and $r = W$. Substituting eq. (4.70), and defining $\epsilon^{1/2} n_s d(r) = D(r)$ to scale out the ϵ and n_s dependence of dislocation spacing, we find the total self-energy of scars as a function of scar number,

$$E_{\rm self}(n_s) = \frac{4\pi^2}{n_s} \int_L^W \rho(r')r'dr' \int_{r' + n_s\epsilon^{1/2} d(r')}^{W} \rho(r) E^D_{int}(r, r')rdr + 2\pi \int_L^W \rho(r) E^D_{self}(r)rdr. \tag{3.25}$$

Since $\rho(r)$ and L are independent of scar number, the second term, which represents the contribution from dislocation self-energies along the scar, is independent of n_s, while the n_s-dependence of the first term — deriving from pairwise dislocation interactions — derives from the numerator as well as n_s-dependence limit of integration over r.

Careful inspection of eq. (3.25) shows it to be a function (up to a multiplicative constant) of two dimensionless variables, reduced tension T/T_* and scaled scar number $\bar{n}_s = \epsilon^{1/2} n_s$. To determine the optimal scar number, $E_{\rm self}(n_s)$, is numerically integrated, and numerically minimized with respect to $\bar{n}_s$ for a given T/T_* to determine the function $\bar{n}_s(T/T_*)$ plotted in Fig. 3.2.c.

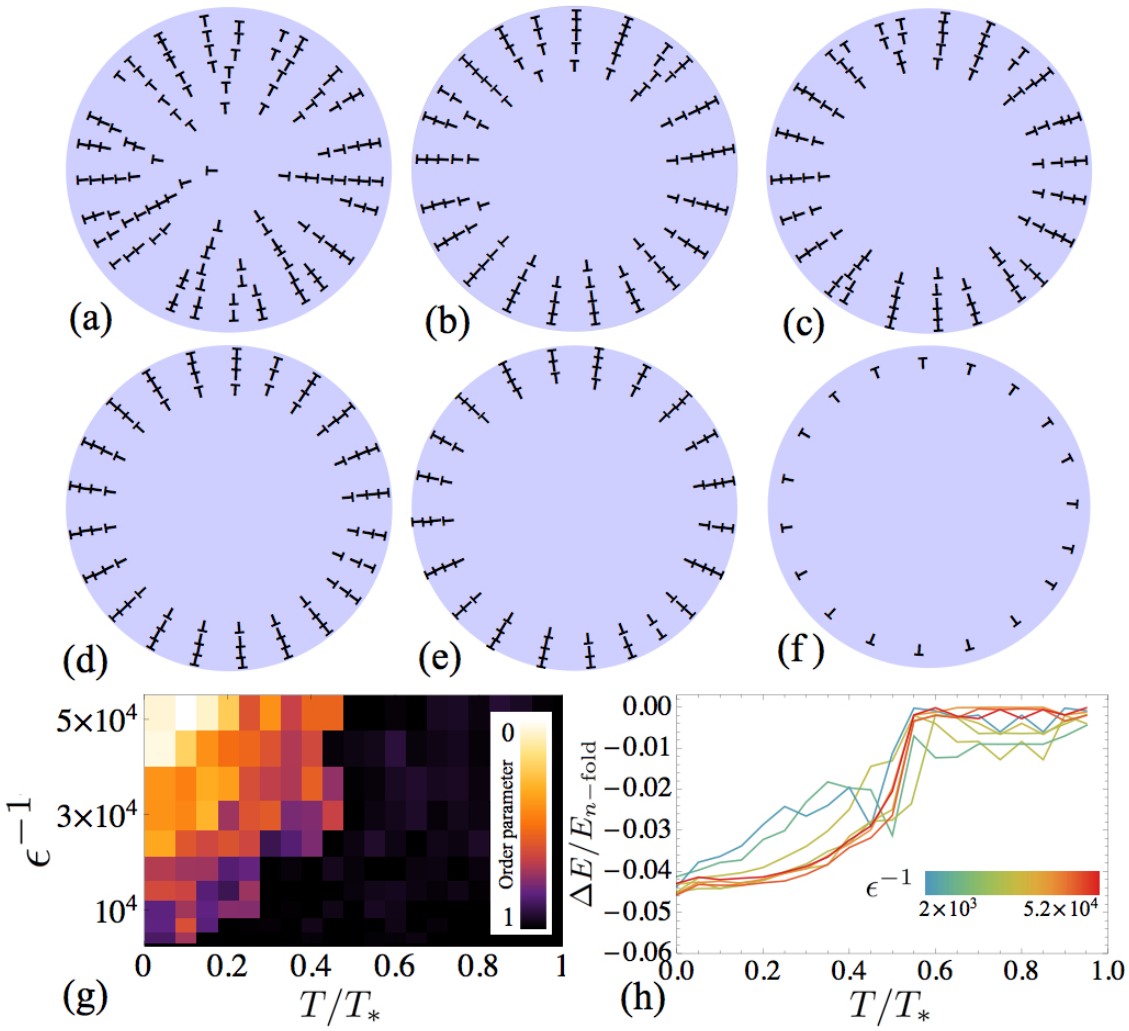

Figure 3.3. (a)-(f)show free dislocation ground-state configurations for $\epsilon = 0.54 \times 10^{-4}$ and sequence of increasing tension: $T/T_* = 0, 0.1, 0.15, 0.3, 0.45$ and 0.7. In (g), map of the degree of n-fold symmetry of dislocation pattern as measured by order parameter S, with dark and light colors showing regions of n-fold symmetric and polydisperse, forked-scar patterns, respectively. In (h), relative energy difference, $\Delta E/E_{n-\text{fold}}$, between sub-dominant energy cost of "free dislocation" and (fixed) n-fold symmetric patterns normalized by sub-dominant energy as functions of reduced tension.

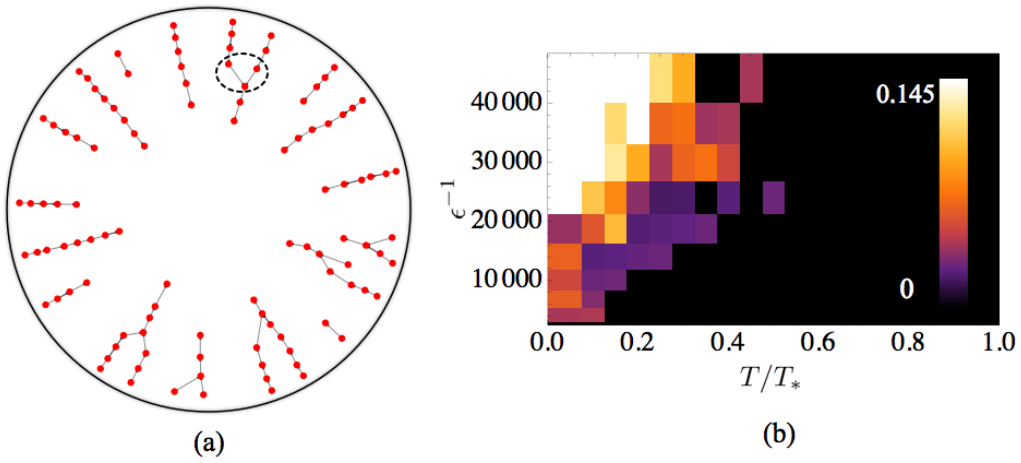

Figure 3.4. (a) shows the cluster analysis which groups dislocations into scars, and counts the number of "forks" or branches (highlighted in the dashed circle). (b) shows the map of ρ_F, the number of forks per scar found in multi-dislocation simulations.

3.3.5 Symmetry of scar patterns

We conclude with an analysis of the symmetry of scar patterns in our "free dislocation" simulations (e.g. defect positions not constrained to n-fold patterns) examples of which are shown in the range $0 \leq T < T_*$ in Fig. 3.3. We quantify the degree of n-fold symmetry in terms of the angular transform of simulated dislocation positions, $\bar{\rho}_m = \int dA\ e^{im\theta}\rho(\mathbf{x})$, and analyze the relative amplitudes of the principle non-zero mode $m = n_s$—which serves as definition of scar number of "free dislocation" simulations—compared to higher harmonics of the distribution, $m = kn_s$. Identical, evenly spaced scars imply $|\bar{\rho}_{n_s}| = |\bar{\rho}_{2n_s}| = |\bar{\rho}_{3n_s}| = \ldots$, and therefore, we define $S \equiv |\bar{\rho}_{2n_s}|/|\bar{\rho}_{n_s}|$ as a measure of perfect n-fold symmetry. Fig. 3.3g shows the variation of n-fold symmetry S with boundary tension and susceptibility to defects, ϵ^{-1}. Significantly, for sufficiently large tension ($T < T_*$) simulated ground states retain high-symmetry, characterized by $S \simeq 1$. Decreasing T for fixed ϵ^{-1}, we find an abrupt transition to $S \ll 1$, indicating marked loss of n-fold symmetry, coincident with the appearance of polydisperse, or forked, scar morphologies observed for $T \to 0$ (Fig . 3.3a-c). Our simulations suggest that in the continuum limit ($\epsilon \to 0$) n-fold symmetric

dislocation patterns become unstable to a lower symmetry, multi-scale pattern for $T < 0.4T_*$, or equivalently, when the length of scarred zone exceeds a critical value, $\ell_s > 0.3W$.

While we relegate a detailed study of this structural instability to a future study [91], we observe here that transition from n-fold to "forked scar" patterns in our simulations is consistent with a transition in the *subdominant energetics* associated with fine-scale variations in the elastic energy. Removing the energy encoded in the field σ_{ij}^{d} from the total energy (see section 3.3.6) Fig. 3.3h compares the subdominant energies of "free dislocation" to fixed n-fold simulations, showing the instability of n-fold patterns gives way to a distinct decrease in the subdominant energy by an amount ($\sim 5\%$) which saturates for large ϵ. The apparently equivalent scaling of subdominant energy with ϵ implies that the loss of n-fold symmetry does not alter the asymptotic, compression-free stress distribution σ_{ij}^{d} achieved in the $b/W \to 0$ continuum limit. As a consequence, those features of the dislocation pattern determined by this asymptotic stress, the scar length and dislocation number, are not altered by the loss of n-fold symmetry, as we observe in Fig. 3.2a-b. Moreover, the "scar number" of forked-scar patterns as measured by the primary mode number of $\bar{\rho}_m$ follows the same data collapse in terms of T/T_* and ϵ implied by eq. (3.20) for n-fold symmetric patterns (Fig. 3.2c-d), highlighting the more general applicability of the structural and energetic hierarchy for controlling defect patterns beyond conditions of idealized symmetry.

Here in order to analyze the structure of polydisperse, forked-scars further and show that the boundary between symmetric, n-fold scars at small T and nonsymmetric structures at larger T observed in Fig. 3.3g does not depend significantly on our chosen structural measure of n-fold symmetry, S the ratio between the first two peaks in the angular Fourier spectrum. Alternatively, we can quantify the transition in terms of the number of "forks" or branches appearing in each optimal configuration. To count the number of forks, we use a simple clustering algorithm that counts number of scars by recognizing set of neighboring dislocations as a an individual scar according to the following rules. 1) each dislocation finds just one nearest neighboring dislocation at a smaller radius, within a $\delta\phi = \pi/4$ azimuthal interval from the radial direction, or 5-7 dipole. 2) each cluster (scar) is a group of dislocations which share at least one neighbor. 3) We define a "fork" as a dislocation that is the neighbor of two or more dislocations at larger radii. One example of

a fork is shown in Fig.3.4a in the dashed circle where filled circles represent dislocations in an optimal configuration. Hence dislocation clusters with perfect radial arrays of dislocations have no forks. We find that when a n-fold symmetry radial scars become sufficiently unstable, scars become increasing branched. We quantify the degree of "scar heterogeneity" in terms of number of forks per dislocation, $\rho_F = F/N_d$. In Fig. 3.4a we show the map of the scar fork density ρ_F, for free-dislocation, ground-state configurations. In this phase map black color shows regions of zero fork density and lighter colors show regions of branched polydisperse scarred patterns, notably a highlighting nearly identical regions of ordered/disordered scars as shown by the Fourier analysis of dislocation distribution.

3.3.6 Dominant and subdominant energy scales

Here, we compute the form of the *dominant* energy stored in the elastic energy of the asymptotic stress pattern, σ_{ij}^{d}, which is realized in the singular, continuum limit, in order to extract and compare the *subdominant* energetics of n-fold and "forked scar" dislocation morphologies observed in our simulations. The dominant energy follows from the solution of stress, strain and displacement fields corresponding to, σ_{ij}^{d}, solutions which are split into two zones, defect free zone for $r < L$, $\sigma_{\theta\theta} > 0$ and compression free zone $r \geq L$, $\sigma_{\theta\theta} = 0$:

$$E_{dom} = \pi \int_0^{L(T/T_*)} (\sigma_{rr}^{in} u_{rr}^{in} + \sigma_{\theta\theta}^{in} u_{\theta\theta}^{in}) r dr + \pi \int_{L(T/T^*)}^{W} \sigma_{rr}^{out} u_{rr}^{out} r dr - 2\pi W T u_r(W), \tag{3.26}$$

In outer zone we have the compression free solution for stress $\sigma_{rr}^{out} = TW/r$, and strain $u_{rr}^{out} = \frac{T}{Y} W/r$. On the other hand the geometric strain-displacement relation yields,

$$u_{rr}^{out} = \partial_r u_r^{out} + 1/2(r/R)^2, \tag{3.27}$$

where R is the radius of the curvature. Knowing u_{rr}^{out}, we integrate eq. (3.27) yielding, $u_r^{out} = TW/Y \ln(r/C_0) - 1/6(r^3/R^2)$. C_0 is determined by matching u_r at edge of the scarred (compression free) zone, $r = L(T/T_*) = (T/T_*)^{1/3} W$. To find u_r^{in} we start with the stress solutions for the inner zone of the sheet that is the rescaled version of stress distribution of the axisymmetric state (eq.

3.5), with $W \to L$ and $T^* \to T(T/T_*)^{-1/3}$. Integration of the radial strain subject to $u_r(0) = 0$ yields,

$$u_r^{in} = -\frac{T}{Y}(\nu - 1)r + \frac{(\nu - 3)r^3}{16R^2} - \frac{(\nu - 1)W^2 r}{16R^2}, \tag{3.28}$$

where ν is poisson ratio.

From matching condition $u_r^{in}(L) = u_r^{out}(L)$, we find the constant,
$C_0 = 2\exp(\nu - 4/3)\, R^{2/3} \left(\frac{TW}{Y}\right)^{1/3}$. Now we can calculate E_{dom} in eq. (13) to find

$$E_{dom} = \frac{\pi T W^2}{6Y}\left(3(2\nu - 3)T + \frac{2W^2}{R^2}Y + 2T\ln\left[2\frac{R^2 T}{W^2 Y}\right]\right), \tag{3.29}$$

We calculate the sub-dominant energy of "free dislocation" and $n-$fold simulations simply by subtracting the dominant energy (eq. (3.29)) from total energy of the system in eq. (3.11)

$$\begin{aligned} E_{sub} &= E_{tot} - E_{dom} \\ &= \sum_{\alpha=2}^{N_d}\sum_{\beta<\alpha}^{N_d} E_{int}^{D}\left(\mathbf{b}_\alpha, r_\alpha; \mathbf{b}_\beta, r_\beta\right) + \sum_{\alpha=1}^{N_d} E_{self}^{D}\left(\mathbf{b}_\alpha, r_\alpha\right) \\ &+ \sum_{\alpha=1}^{N_d} E_{relax}^{D}\left(\mathbf{b}_\alpha, r_\alpha\right) - (E_{dom} - E_0). \end{aligned} \tag{3.30}$$

The last term in eq. (3.30) is,

$$E_{dom} - E_0 = \frac{\pi W^2}{6Y} T_*^2 \left[-1 + (4 - 3\alpha)\alpha + 2\alpha^2 \ln\alpha\right], \tag{3.31}$$

where we define $\alpha \equiv T/T_*$. Expanding the above expression in the limit of weak confinement, $T \to T_*$ we have $E_{dom} - E_0 \approx \frac{\pi W^2 T_*(\alpha-1)^3}{9Y}$. The first three sums in eq. 3.31 are calculated explicitly in numerical simulations of caps.

Based on the decomposition above, we remove the energy encoded in the field σ_{ij}^{d} by using 3.31, from the total energy to calculate subdominant energetics of multi-dislocation patterns. Fig. 3.3h

compares the subdominant energies of "free dislocation" to fixed n-fold patterns, referred to as E_{free} and $E_{n-\text{fold}}$ respectively. The energy difference $\Delta E = E_{\text{free}} - E_{n-\text{fold}}$ plotted in Fig. 3.3, shows that the instability of n-fold patterns to more complex, "forked" scar patterns gives way to a distinct decrease in the subdominant energy by an amount ($\sim 5\%$) which saturates for large ϵ. This implies that the structural transition from n-fold symmetric scars does not alter the asymptotic, compression-free stress distribution σ_{ij}^{d} achieved in the $b/W \to 0$ continuum limit, which is consistent with the stress patterns generated by both defect patterns shown in Fig. 3.5a. The stress patterns are evaluated using positions of dislocations extracted from simulations and superposing the corresponding solutions of the azimuthal stress calculated in the appendix section of chapter 2.6. Hence, those features of the dislocation pattern determined by this asymptotic stress, the scar length and dislocation number, are not altered by the loss of n-fold symmetry, as we observe in Fig. 3.2a-b. Moreover, we find that the "scar number" as measured by the primary mode number of $\bar{\rho}_m$ follows the same data collapse in terms of T/T_* and ϵ implied by eq. (3.19) for n-fold symmetric patterns (Fig. 3.2c-d), highlighting the more general applicability of the structural and energetic hierarchy for controlling defect patterns beyond conditions of idealized symmetry.

3.4 Energy minimization of multi-dislocation ground states

Here, we detail the numerical approach for exploring the multi-dislocation ground states. For a given W/b ratio and curvature $K_G W^2$ (which correspond to a given value of ϵ), total dislocation number N_d and reduced tension T/T^*, two classes of simulations were performed: 1) "free dislocation" and 2) "n-fold" simulations. "Free dislocation" simulations start with random initial configurations of N_d dislocation coordinates at (r_i, ϕ_i), for $i = 1...N_d$, with $\mathbf{b} = b\hat{\theta}$. Each simulation starts with $10^3 - 10^4$ random initial configurations (depending on the number of dislocations growing with $\epsilon^{-1/2}$) to account for the large number of local minima for $N_d \gg 1$. The total energy in eq. (3.11) is minimized with respect to the position of the dislocations for all randomly initiated copies using the method of steepest descent. The state with lowest resulting energy for a given N_d is selected as the minimal energy for N_d dislocation, $E(N_d; T/T_*, b/W, K_G W^2)$. In order to find the minimal-energy dislocation number, we determine $E(N_d; T/T_*, b/W, K_G W^2)$ for a range of possible

dislocation numbers, $N_d = N_d^c \pm 0.25 N_d^c$ (where we use a linearized approximation of the continuum theory prediction $N^c \equiv \epsilon^{-1/2}(1 - T/T_*)$ as the initial guess) and select the N_d corresponding to lowest energy. The resulting "simulated ground states" are structures that are minimized with respect to the dislocation positions and dislocation number.

For the case of fixed "n-fold" simulations, dislocations are constrained to n_s identical radial lines (scars), equally spaced at angular intervals of $2\pi/n_s$ on the cap. The radial positions of the $N_d/n_s = M$ concentric rings (constrained to an integer) of dislocations are initialized randomly, then relaxed via steepest descent. Similar to the procedure outlined for "free dislocation" simulations, the scar number is varied to find the optimal n_s for a given N_d, T/T_*, b/W and $K_G W^2$. Both "n-fold" and "free dislocation" simulations are performed in the range of $T/T_* = 0...1$, with a step size $\delta T/T_* = 0.05$, for $\epsilon = 0.17 \times 10^{-4} - 0.15 \times 10^{-2}$. These simulations were carried out over a range of cap sizes and curvatures: $W/b = 100 - 1400$ and $W/R = 0.05 - 0.3$ (see Table (3.1, 3.2) for full list of parameter values).

3.5 Orientational pinning of dislocations in crystalline caps

Here we aim to study the effect of lattice structure on features of minimal multi-dislocation patterns, optimal pattern of scars, n_s. The formalism we develop in this chapter for continuum theory of scars on membranes, does not include the presence of underlying crystalline structure of the spherical cap. As one introduce the predicted optimal pattern of defects in a hexagonal crystal (see figure 3.6), each dislocation needs to line-up with one of six crystallographic axes of the underlying hexagonal symmetry. Rotating the crystalline lattice by a small rotation can affect the dislocation orientation on each scar, but our formalism does not associate an energy difference between these two configurations, Hence these two states are degenerate. This is not possible except for certain configurations, like three or six fold symmetric patterns which are commensurate with the underlying lattice symmetry. In order to introduce scar patterns that are not compatible with the crystallographic axes, the presence of the orientational pinning of dislocations to the lattice symmetry becomes relevant and we need to consider dislocations with non-parallel Burgers vector on each scar. In our numerical simulations and our continuum theory of scars, we constrained

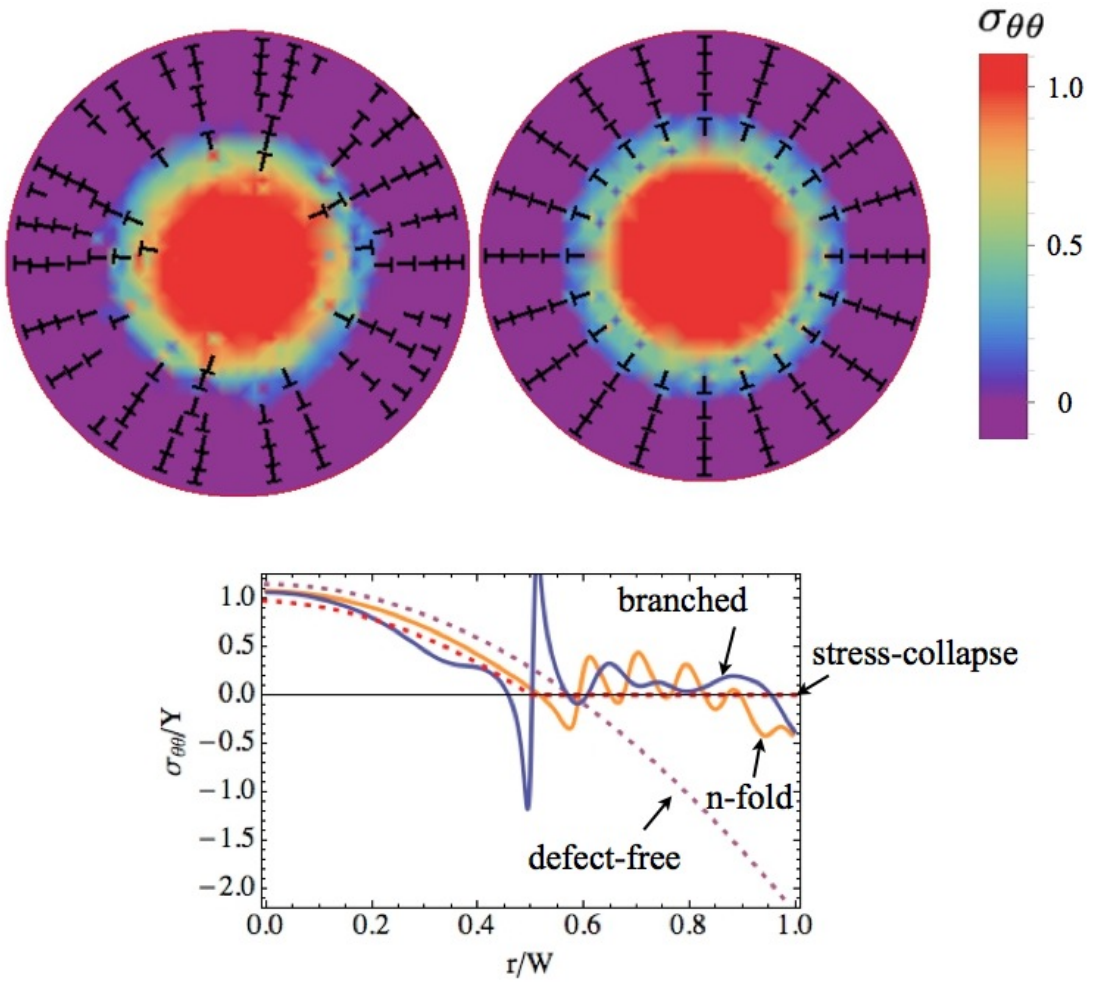

Figure 3.5. It shows the azimuthal stress profile of the "free dislocation" and n-fold symmetric patterns for $\epsilon = 0.42 \times 10^{-4}$ and $T/T_* = 0.15$. According to the color scale, purple indicates the region of compression-free stress field. The stress profile is scaled according to the maximum stress at the center, $\bar{\sigma}_{\theta\theta} = \sigma_{\theta\theta}/\sigma_{\theta\theta}(r = 0)$. The azimuthal stress of the dislocation is calculated in the appendix section of chapter 2.6.

dislocation to have a polarization vector $\vec{a} = |b|\hat{r}$, defined as a 5-7 dipolar vector perpendicular to the Burgers vector $\vec{b}$. We relax this constraint in our numerical simulations and introducing a discrete set of degrees of freedom for each dislocation to consider the effect of orientational pinning of dislocations to the lattice symmetry. These are equivalent to three reciprocal lattice vectors associated to the hexagonal symmetry given by $G_k = |G|\,[\cos(\pi k/3), \sin(\pi k/3), 0]$ for integer k. The modified "Free dislocation" method starts with large number of initial random configurations ($\approx 10^3$) of defects, but here we also randomly assign a lattice orientation to each dislocation from six possible crystallographic axes. Hence each defect has degrees of freedom given by triple, $(\vec{a_i}, r_i, \phi_i)$ which characterizes a dislocation with polarization vector $\vec{a_i}$ at polar position (r_i, ϕ_i) on the cap (see fig. 3.6b). The total energy in eq. (3.11), will be minimized using method of steepest descent with respect to the position of dislocations for all random copies. Next step is equilibrating each simulated quenches using Monte-Carlo method. We update the dislocation orientation, $\vec{a} = a_\phi\hat{\phi} + a_r\hat{r}$ from the discrete lattice set, $\mathbf{G}$ available for the randomly chosen defect via standard Monte-Carlo algorithm, and cooling down the system gradually following the annealing schedule to the final temperature and performing steepest descent on the final configurations. The structure of this algorithm can be considered as a version of "Basin Hoping" algorithm where certain number of Monte-Carlo steps, are followed by a descent relaxation routine. The minimal energy configuration is selected from this ensemble of simulated quenches with minimal dislocation orientation. The schematic of the simulated ground state configurations with each dislocation polarization is represented by the arrow for a sequence of decreasing tension are illustrated in fig. 3.6a. In order to identify the symmetry of the scar pattern we calculated the angular Fourier transform of dislocation positions, $\bar{\rho}_m$ and use the defined order parameter $S = |\bar{\rho}_{2n_s}/\bar{\rho}_{n_s}|$ (see section 3.3.5 for details of the definition). Fig. 3.6c shows the plot of S as function of T/T_* of the simulated configurations which shows $\sim 32\%$ of states exhibit 6-fold symmetric scar pattern. Intuitively one might expect the emergence of majority of states with underlying 6-fold symmetry (dashed vertical line in fig 3.6c), however by looking at schematics of configurations we observe complex modes that polygonization of the scars (kinks in single radial scars) and appearance of

groups of few short scars with their orientation parallel to the local lattice symmetry lead to obscuring the simple 6-fold symmetric patterns.

Nonetheless, the numerical simulations reveal that underlying lattice structure does not affects the global features of minimal multi-dislocation patterns, described by the total number of dislocations. Fig. 3.6d emphasize that the optimal dislocation number derived from the simulated ground state configurations agrees with the scaling of N_d provided by the continuum theory predictions. Although this scaling (dashed line in fig 3.6d) seems to under estimate the dislocation number. This is related to the fact that the presence of the orientation pinning of dislocations forces the dislocation to line up locally with the lattice direction which reduce the total effective radial polarization of dislocations $\vec{a_T} = \sum_{i=1}^{N_d} a_r^i$ needed to screen the frustration. Hence, populating the ground state configurations with more dislocations compensate for the lower total effective polarization of jagged scars with kinks.

3.6 Summary

In summary, multi-dislocation ground states of curved crystals exhibit a characteristic sequence of patterns whose features are governed in concert, by the state of "perfect screening" of geometrically induced stresses achievable in the singular limit $a/W \to 0$, where dislocation number grows unbounded, and simultaneously, by the subdominant mechanical costs associated with the imperfect approximation of this state with a finite number of discrete defects. The emergence of a characteristic structure and energetics of multi-dislocation patterns in the tractable continuum limit of $b/W \to 0$ yields new predictions for the symmetries of observable scar patterns formed on particle-coated liquid interfaces in the poorly characterized shallow-curvature regime [126] and it opens the door to a broader and more rigorous understanding of the role of "plastic" modes of curved-crystal relaxation beyond this particular limit (small area coverage, larger boundary tension, rigid substrate). For example, it has been shown [132] for flexible crystals bound to deformable spherical substrates that the pattern of "elastic" deformation triggered by confinement (radial wrinkles) achieves the *identical* state of asymptotic stress for $T \lesssim T_*$. Hence, the relative stability of plastic vs. elastic response to curvature is determined purely by the respective sub-dominant costs

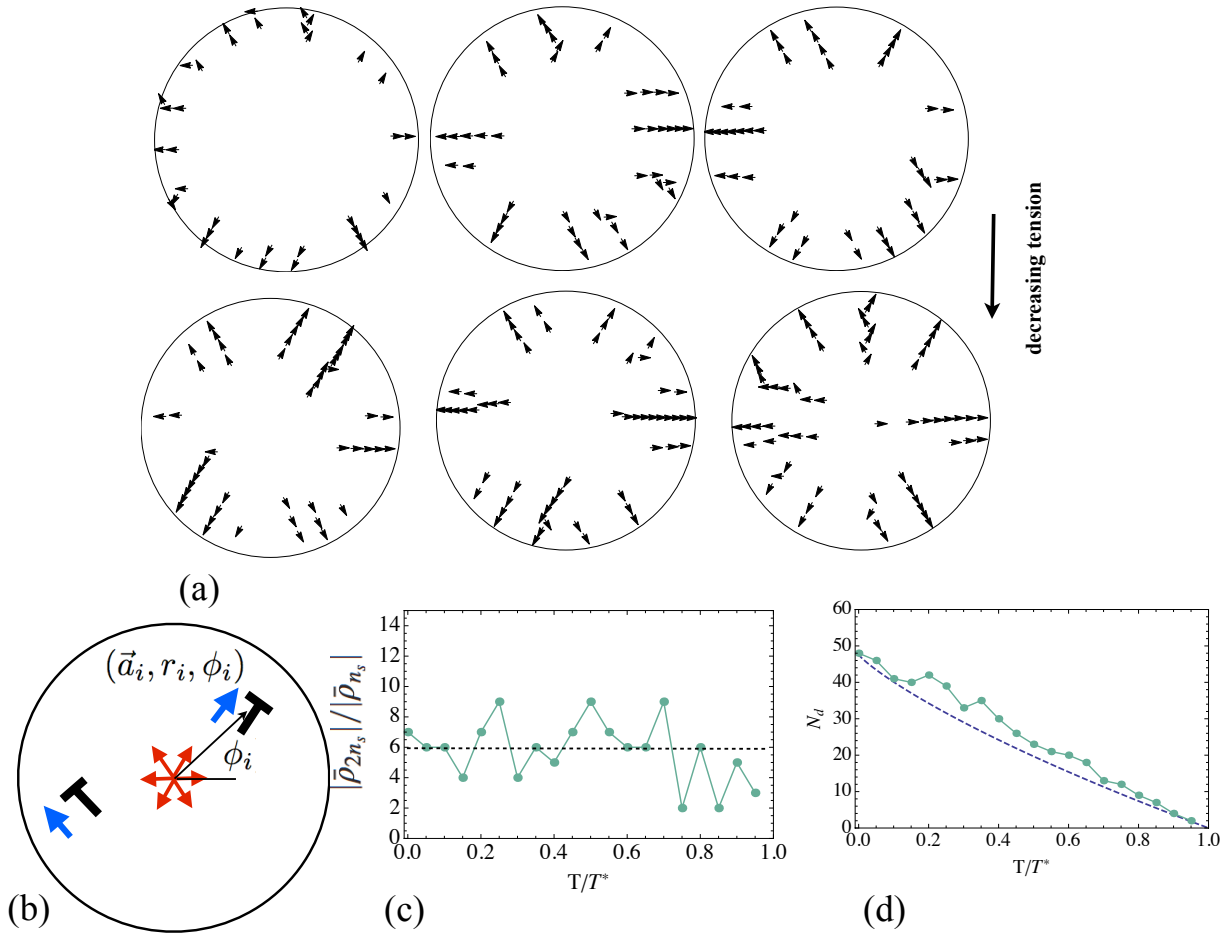

Figure 3.6. (a) Shows schematics of ground state dislocation patterns based on the multi-dislocation simulations on the cap for a sequence of decreasing tension with the degrees of freedom of a dislocation presented in (b) by $(\vec{a_i}, r_i, \phi_i)$. (c) illustrates plot of S as function of T/T_* of the ground state configurations with vertical dashed line marks the 6-fold symmetry for a system with $K_G W^2 = 0.05$ and $b/W = 0.0011$. (d) Points represents the optimal total number of dislocations, N_d, from numerical simulations and dashed line shows the predication of the continuum theory of scars.

of either mode, which reveals a non-trivial transition from wrinkles to scars with increasing geometric compression. Finally, by performing discrete dislocation simulations, we test the accuracy of asymptotic and tractable results of continuum theory of scars in predicting features of ground state configurations. This illustrates how one can replace complex man-body problem of large number of defect singularities with long range interactions by a simple set of stress-relaxed states which explain the geometry, mechanics and energetics of heterogeneous curved crystals.

Next chapter will reconsider long-standing questions about the asymptotic approach to continuum limit of spherical crystals at large surface coverage (e.g. the Thomson problem). We demonstrate how the appearance of excess disclinations restructure the underlying dominant stress distribution of highly-curved caps, and thereby alter the consequences of multi-dislocation stress collapse relevant to 1) optimal symmetries of multi-dislocation scars that decorate "charged" disclinations of close spherical shells [119, 129] (e.g. the Thomson problem) and 2) the curvature-driven transition from "uncharged" to "charged" dislocations scars on crystalline caps.

Table 3.1. Parameters used for ground-state simulations

b/W	W/R	$\epsilon_d^{-1/2}$	Simulation type
0.005	0.25	50	Free
0.0011	0.07	63	Free
0.0011	0.09	81	Free
0.0011	0.11	99	Free
0.0011	0.13	117	Free
0.001	0.15	150	Free
0.0011	0.19	171	Free
0.0011	0.21	189	Free
0.0011	0.23	207	Free
0.0011	0.25	225	Free
0.01	0.25	25	n-fold
0.01	0.3	30	n-fold
0.005	0.25	50	n-fold
0.0011	0.07	63	n-fold
0.0011	0.09	81	n-fold
0.0011	0.11	99	n-fold
0.0011	0.13	117	n-fold
0.001	0.15	150	n-fold
0.0011	0.19	171	n-fold
0.0011	0.21	189	n-fold
0.0011	0.23	207	n-fold
0.0011	0.25	225	n-fold
0.0007	0.05	70	n-fold
0.0007	0.06	84	n-fold
0.0007	0.07	98	n-fold
0.0007	0.08	112	n-fold
0.0007	0.09	126	n-fold
0.0007	0.1	140	n-fold
0.0007	0.11	154	n-fold
0.0007	0.12	154	n-fold
0.0007	0.13	182	n-fold
0.0007	0.14	196	n-fold
0.0007	0.15	210	n-fold
0.0007	0.17	238	n-fold
0.0007	0.19	266	n-fold

CHAPTER 4

NEUTRAL VS. CHARGED SCAR PATTERNS IN CURVED CRYSTALS

4.1 Introduction

Seeking optimal ground state packings of curved crystallography has remained an outstanding challenge for a century from the historic Thompson problem to the assembly of protein subunits in spherical viruses [109, 140], and more recent development in characterizing the structure of particle coated droplets [119, 126]. One of the structural motif in theses problems is the presence of disinclination decorated with the arrays of dislocations (grain boundaries) that leads to a variety of novel structures not encountered in the plane. For instance, for crystalline tilling of the whole sphere, spherical topology requires a variation in the local packing symmetry: All states possess at minimum 12 discs whose nearest-neighbor geometry is fivefold coordinated [141]. Hence, fivefold disclinations in an otherwise sixfold packing are necessary components of the optimal (ground-state) structure. One novel example in predicting the optimal symmetry of disclinations in this class has been proposed in a paper by Caspar and Klug [140] in the context of spherical viruses with shells consisting of protein subunits. Twelve of these fivefold coordinated protein clusters sit at the vertices of a regular icosahedron. This class of tessellation that only include 5-fold disinclination faithfully predicts the ground-state structure of small to intermediate system sizes, R/a where R is the sphere radius and a is the lattice spacing. It has been shown by intensive numerical simulations [110, 111, 129] and experiments [119, 126] that new ground states with dislocations emerge for larger values of particles, $\gtrsim 400$ and more complex defect morphology with arrays of dislocations emerge for large system sizes [146, 147, 149].

The symmetric patterns of scars on a spherical topology also has been studied in the context of Abrikosov vortex lattice in a thin-film superconductor with a spherical geometry [111]. In contrast in [103] the prediction of the existence of such symmetric patterns has been questioned by a series of

numerical simulations and has been shown once the number of charges on a sphere interacting via repulsive electrostatic interaction is large enough, the lowest energy states are not those with the highest symmetry [120]. The range and accuracy of these numerical simulations are limited by the exponential growth of the number of ground states located in a rough energy landscape. Here we aim to develop a theoretical framework that gives rise to predicting the structures, mechanics and energetics of the defective patterns in the well defined continuum limit. In this universal class of crystalline spherical surfaces, spherical caps at arbitrary surface coverage are good model systems to explore defect patterns in presence of the open boundary and generalized boundary condition with boundary forces and lead to tractable analytical solutions. In contrast to Thompson problem where the total topological charge is constrained to 4π, there exist no such topological condition for a surface with an open boundary, including spherical caps. In [135, 136] it has been shown for the case of spherical cap that there is a critical value of the cap surface coverage, $(K_G^{1/2}W)_c = \sqrt{2/3}$, above which the elastic screening by the disinclination is sufficient to compensate for the defects self-energy cost. The favorable interaction between positively charged disclination and the membrane with positive Gaussian curvature indicates the effective screening of the positive curvature by the disclination induced stresses. We will show that elastic energy sets a critical value for the surface coverage of the spherical cap, $K_G W^2 = 2/3$ that does not depend on the system size. Above this critical value curved membranes are unstable to incorporation of one or more disclinaitons. One can generalize the effective screening of integrated Gaussian curvature by positively charged disclination to the case of caps with imposed boundary forces σ_b, consequently construct a phase digram spanned by Gaussian curvature and boundary stresses. The phase digram in fig 4.1a, shows the competition between defect-free state and cap with centered 5-fold disclination, indicates there exist a critical generalized stress, σ_b^* below which bare 5-fold disinclination is stable. This argument is purely based on energetics of disclination that exhibit a logarithmic divergence at the center in the stress fields. Here we focus on the effect of emergent patterns of dislocations, decorating the disclinaiton. This gives rise to the new stable ground state configurations with different underlying mechanical state of stress. Intuitively formation of the dislocation cloud around the excess disclination can

effectively reduce the high strain of the disclination and influence the stability of topologically charged cap and dramatically restructure the phase space of stable states (see fig. 4.1b).

Here we aim to harness and extend the "far-from-threshold" (FT) analysis that originally developed in the context of "tension field theory" to study emergent patterns of wrinkles and crumples in thin sheets, far from buckling threshold [121, 134]. Recently it has been shown that key features of emergent patterns of symmetric dislocation scars (*e.g.* symmetry of the defect pattern in analogy to the wavelength of wrinkles) on curved crystalline sheets can be explained with common basis that underlies the compression-free states in wrinkled thin sheets [154]. This approach was developed in the well-behaved continuum limit, $b/W \to 0$ of highly defective state for the case of topologically "neutral" state, in absence of disinclination. Here we generalize these principles in the presence of 5-fold disclinations, which are expected to be favored in the ground states at large curvature and which introduce singular sources of stress to curved crystals. Significantly, this analysis reveals a remarkable contrast in stress-collapse afforded by wrinkle-mediated vs. dislocation-mediated patterns. While out-of-plane deformation is only capable of collapsing regions of unstable compression, here we show that patterns of dislocation scars are capable of both tension- and compression-collapse depending on their Burger's vector orientation.

Here we derive principles that select the "stress-free" states for tensile and compressive strain at the boundary with a non-trivial asymmetry between two distinct topological states described by topologically neutral and charged lattice.

In this chapter we focus on the morphology and energetics of "*charged scars*" described by arrays of dislocations with an excess disclination, in the presence of an external compressional or tensional field acting at the free boundary. Along with the geometric frustration imposed by the Gaussian curvature, we show that boundary forces play a critical role to regulate the stress in curved crystals, which we show has a critical impact on phase transition between "charged" and "neutral" defect patterns." By exploiting universal stress collapse principles [154], we study the nature and energetics of stability of topologically "charged" and "neutral" crystals (in presence and absence of excess 5-fold disclination) with spherical geometry that gives rise to distinct optimal defect patterns in the ground state configurations.

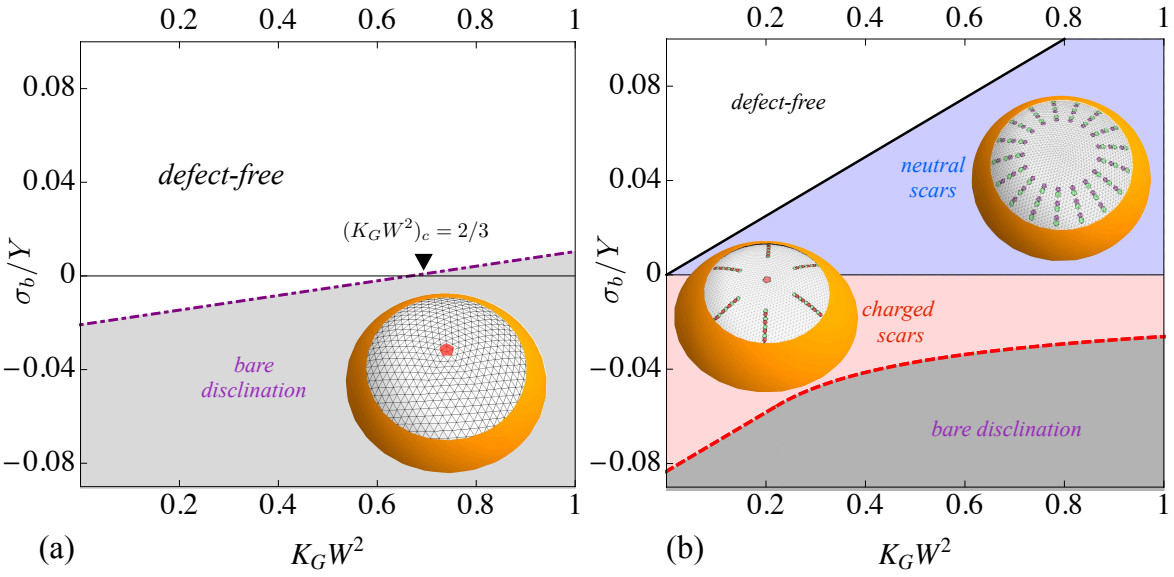

Figure 4.1. Phase diagrams spanned by the surface coverage $K_G W^2$ and external boundary stresses, σ_b/Y for axi-symmetric states in (a) including defect free stressed crystalline sheets and topologically charged caps with the centered 5-fold disclinaiton. (b) illustrates the equivalent phase diagram in the presence of grain boundary scars.

We reveal that the boundary stresses select an optimal relaxed state of stress that lead to scar patterns strongly bounded to the crystal boundary and consequently stabilized the charged scars and bare disclination with compressive boundary stresses and neutral scars with tensile stresses. We construct a phase digram spanned by Gaussian curvature and boundary stresses which illustrate two topologically distinct stable phases of charged and neutral crystal with spherical geometry are separated by the singular limit of infinite confinement (zero boundary forces). We illustrate the morphological phase diagram in fig 4.1b, which shows stretched sheets stabilize neutral pattern of scars and compressed crystalline caps drives the stability of charged scars. This shows the central role of boundary forces in breaking the charge neutrality of the spherical crystal and distinguishing the phase dominated by charged lattice from the topologically neutral phase stabilizes by tensile boundary forces. Comparison between two phase diagrams depicted in fig. 4.1, manifest the dramatic effect of dislocations in restructuring the phase digram of dislocation-free states in fig. 4.1 (a), leading to new mechanical states in the continuum limit. We will show highly heterogeneous

defect-riddled phases in fig. 4.1 (b) can be described by novel asymptotic relaxed stress patterns in the continuum limit where dislocation core energy is vanishingly small.

We find that curvature-induced breaking of the "charge" neutrality of the lattice in this singular limit, can be fully understood in terms of hierarchy of mechanically accessible energy levels in the continuum limit. Imperfect relaxation of geometric stresses by discrete dislocations defines a sub-dominant elastic cost gives a way to identify a transition between charged and neutral states which is governed by the geometry (Gaussian curvature) and lattice spacing at this singular limit.

The organization of this chapter is as follows. In section II we begin with the asymptotic analysis of dominant stress fields related to charged and neutral scar patterns in the presence of non-vanishing boundary forces. Section III focuses on ground state configurations explored via performing discrete dislocation simulations to examine the predictions provided by "far-from-threshold" continuum approach for optimal features of scar patterns. Section IV discusses different scales of elastic energy related to scarred relaxed states which indicates non-trivial transition from "neutral" to "charged" defect patterns controlled by boundary forces, Gaussian curvature. We summarize and conclude with a brief discussion of outstanding challenges for understanding the complex and highly force sensitive spectrum of topological defects in crystalline membrane which .

4.2 Asymptotic analysis of multi-dislocation ground-state patterns with spherical geometry, a continuum perspective

4.2.1 Charged scars in presence of tensile stress field

As a testing ground for understanding the mechanics of charged scars (dislocation scars with excess disclination), we focus on a simple model system, an elastic spherical cap with Gaussian curvature,K_G with a centered five-fold disclination. Our starting point is a continuum description of 2D hexagonal crystal whose stretching moduli is Y. We generalize the elastic description by considering non-vanishing boundary forces that act on the sheet by pulling via a generic substrate adhesion, T or compressing the membrane with stress, P. Our elastic description in presence of

external forces is intimately related to experimental systems like membranes and monolayers that are embedded in the medium often with nearby substrates or interfaces which act on them by some some effective potential [85].

The axially symmetric stress of the spherical cap with curvature K_G with a centered five-fold defect is described by the solution to the compatibility relation (second Föppl- von Kàrmàn eq.),

$$Y^{-1}\nabla_{\perp}^{2}\sigma_{ii} = -K_G + s\delta^2(\mathbf{r}) - \nabla_{\perp} \times \mathbf{b}(\mathbf{x}) \tag{4.1}$$

with $-\nabla_{\perp} \times \mathbf{b}(\mathbf{x}) = \sum_{\alpha}(\mathbf{b}_{\alpha} \times \nabla_{\perp})\delta(\mathbf{x} - \mathbf{x}_{\alpha})$ representing the continuous source of dislocations. In absence of dislocations (ignoring last term in eq. 4.1), Radial and hoop stresses in this state are composed of geometric strains imposed by curvature and the 5-fold disclination (singular source of stress). Including a generalized external stress, σ_b, at the boundary of the crystal, $r = W$ leads to the boundary condition $\sigma_{rr}(r = W) = \sigma_b$ to solve eq (4.1),

$$\begin{aligned}
\sigma_{rr}^{f-axi}/Y &= \frac{s}{4\pi}\ln(r/W) + \frac{K_G}{16}(W^2 - r^2) + \sigma_b/Y; \\
\sigma_{\theta\theta}^{f-axi}/Y &= \frac{s}{4\pi}(\ln(r/W) + 1) + \frac{K_G}{16}(W^2 - 3r^2) + \sigma_b/Y
\end{aligned} \tag{4.2}$$

Tension at the boundary, $\sigma_b = T$ represents the surface adhesion that pulls the sheet over the substrate. Results for external compression given by $\sigma_b = -P$ is presented in the appendix II. The first term in eq. (4.2) are related to the disclinaiton induced stresses ($s = \pm\pi/3$ for five- and seven fold defects) and second contribution in stresses are curvature induced strains. Notice that for $\sigma_b = 0$, curvature introduces hoop tension at the core for $r < W/\sqrt{3}$ and hoop compression at the periphery for $r > W/\sqrt{3}$. But this profile is opposite for the positively charged disclination, where $r < e^{-1}W$ is compressive in the inner zone and tensile in the outer zone, $r > e^{-1}W$. Hence five-fold disclination "screen out" the curvature-induced stresses and for the hyperbolic plane $K_G < 0$ these zones are swapped and make seven-fold disclinaiton ($s = -\pi/3$) favorable. Further investigation of hoop stresses show that for $K_G W^2 < 2/3$ hoop stress in eq. 4.2 has the compressive inner zone

and the tensile outer zone, but for larger surface coverage, $K_G W^2 > 2/3$ azimuthal component of the stress, $\sigma_{\theta\theta}$ develops a third compressive zone at the edge of the cap. We show in the next section this leads to a critical value for the surface coverage above which the elastic screening by the positively charged disclination is sufficient to compensate for the elastic cost of defect in the axi-symmetric state. Generally speaking for surfaces with open boundaries, the number of defects are not set by topological constraints eq. (1.2), instead the energetics govern the stability of the defects. The optimal number is determined by the balance between the large elastic costs of defects and their attractive interaction to curvature and the energetics related to the boundary forces.Our analysis is based on the continuum elasticity theory of 2D crystals, where in axi-symmetric state, described by stress fields in eq. 4.2 the total elastic energy is,

$$\begin{aligned} E^{axi} &= \frac{1}{2}\int dA\sigma_{ij}u_{ij} - \sigma_b \Delta A \\ &= \pi W^2\left[\frac{1}{288} + \frac{1}{6}\sigma_b + \sigma_b^2(\nu-1)/Y + \frac{1}{1152}\left(3YK_G^2W^4 - 6K_GW^2\left[Y - 48\sigma_b\right]\right)\right] \quad (4.3) \end{aligned}$$

For a weakly-curved crystal, elastic strain derives from in-plane displacement $\mathbf{u}(\mathbf{x})$ (components in xy plane) and out-of-plane defection $h(\mathbf{x})$, with $u_{ij} = (\partial_i u_j + \partial_j u_i + \partial_i h \partial_j h)/2$, while the stress response of a hexagonal crystal is characterize by Lamé constants, λ and μ, $\sigma_{ij} = \lambda\delta_{ij}u_{kk} + 2\mu u_{ij}$. The second term in (4.3) represents the work by the generalized external stresses, σ_b where $\Delta A = W\int d\theta\ u_r(r=W)$ is the area change of the sheet, and (r,θ) are polar coordinates. In absence of boundary forces, $\sigma_b = 0$, eq. 4.3 simplifies to $E^{axi}_{\sigma_b=0} = \pi W^2\left[1/288 + Y\left(3K_G^2W^4 - 6K_GW^2\right)/1152\right]$. The first term shows the elastic cost of discretized topologically charged 5-fold disclination related to the disruption of orientational symmetry of the lattice induced by the defect. Elastic cost of stretching the membrane is related to the imposed Gaussian curvature on the sheet represented in the second term. Finally the favorable interaction between positively charged disclination and the membrane with positive Gaussian curvature indicates the effective screening of the positive curvature by the disclination induced stresses. This energy sets a critical value for the surface coverage of the spherical cap, $K_G W^2 = 2/3$ that does not depend on system size. Above this critical value curved membranes are unstable to incorporation of one or more disclinaitons. This

argument is purely based on energetics of disclination that exhibit a logarithmic divergence at the center in the stress fields. Here we aim to focus on the effect of emergent patterns of dislocations, decorating the disclinaiton. This gives rise to the new ground state configurations with different underlying mechanical state of stress. The tensile stresses induced by such a disclination are very high, and the energy can be lowered by polarizing the surrounding medium into dislocation pairs, analogous to point and dipolar charges in a polarized electrostatics medium. This mechanism also can be understood by looking at the right hand side of compatibility equation, where dislocations with certain polarization, (seven-fold disclination points to the centered disclination), can screen the stresses generated by the effective total topological charge of $s\delta(\mathbf{r}) - K_G$. Although this argument might seem intuitive and provide some scaling prediction for the total number of dislocations (see chapter II section 3.3.2), but it fails to provide a full morphological description of the scarred pattern in presence of boundary forces. Even in the absence of any sources of stress ("prefect geometric screening"), the compatibility relation has a non-zero stress solution that might not lead to a energy minimizer configuration. Hence we follow the analytical tools that we develop in the last chapter and construct our analysis based on the stress-collapse principles in the asymptotic continuum limit. We conjecture that exists a unique stress solution to the biharmonic eq. that collapses the stresses in the tensile zone (generated by the bare disinclination) via a certain distribution of dislocations. We call these disloactions with the seven-fold head pointing to the center, "tensile dislocations".

There is a significant difference between two types of singularity, disclination and dislocations, introduced in the compatibility relation, eq. 4.1. Disclination carries a discrete, scale-free topological charge of $s = \pi/3$, in contrast to dislocation that constitute a dipole of 5-7 disclination pair with b as dipolar separation that sets by the lattice spacing. This dipolar separation introduce a length scale for the system that gives a rough estimate of the dislocation energy $\sim Yb^2 \ln(b/W)$ which is vanishingly small in the continuum limit, $W/b \to 0$. In this limit, crystalline sheet generically is unstable to the formation of large number of multi-dislocations, scars which has been dubbed as "*charged scars*" to emphasize on presence of excess disclination.

In the axial symmetry of highly defective state, we conjecture the existence of tension-free solution where the hoop stress collapses via dislocations characterize by Burgers vectors $\mathbf{b} = -b\hat{\theta}$ that reside in an annulus $L_1 < r < L_2$ with tensile strains in the reference state. We construct the stress pattern with three different zones, including first, in the vicinity of the 5-fold discliantion, second, the middle zone that describes the stress collapse field and the third zone at the periphery that includes the effect of interstitial and vacancies. This construction modifies the stress solution to most general form with three region, for $0 < r < L_1$ we have:

$$\begin{aligned} \sigma_{rr}^{Ic}/Y &= \frac{s}{4\pi}\ln(r/L_1) + \frac{1}{16R^2}(L_1^2 - r^2) + C_1; \\ \sigma_{\theta\theta}^{Ic}/Y &= \frac{s}{4\pi}(\ln(r/L_1) + 1) + \frac{1}{16R^2}(L_1^2 - 3r^2) + C_1 \end{aligned} \tag{4.4}$$

and for the middle region $L_1 < r < L_2$, we construct the, tension-free solution where $\sigma_{\theta\theta} = \sigma_{r\theta} = 0$ and in-plane force balance equation in r direction is, $\partial_r(r\sigma_{rr}) = 0$ yields,

$$\begin{aligned} \sigma_{rr}^{IIc}/Y &= C^{'}/r; \\ \sigma_{\theta\theta}^{IIc}/Y &= 0 \end{aligned} \tag{4.5}$$

Finally for the outer region, $L_2 < r < W$, we have the following stress profile,

$$\begin{aligned} \sigma_{rr}^{IIIc}/Y &= s^{'}\ln(r/W) + \frac{1}{16R^2}(W^2 - r^2) + B/r^2 + C; \\ \sigma_{\theta\theta}^{IIIc}/Y &= s^{'}(\ln(r/W) + 1) + \frac{1}{16R^2}(W^2 - 3r^2) - B/r^2 + C \end{aligned} \tag{4.6}$$

$B, C, C^{'}, C_1, s^{'}, L_1$ and L_2 are coefficients and lengths that are unknown and need to be determined. Details of calculation for these coefficients using stress boundary conditions at $r = L_1$, L_2 are reported in the appendix I. Here $s^{'}$ is the effective discliantion charge that is seen in the third zone. This effective charge is related to the dislocation density in the scarred zone. This relation become transparent by integrating the compatibility equation and matching the discontinuity in

$\partial_r \sigma_{ii}^{Ic,IIc,IIIc}$ at two ends of the scar at $r = L_1, L_2$. The calculation is done in the appendix I which shows, $s^{'} = \frac{\pi/3}{4\pi}$ which is equal to the charge of the centered 5-fold disclination. This indicates that in the presence of scars, the topology of the spherical cap with centered disclination remains intact and scar patterns exhibit a local mechanism in stress relaxation.

Having the optimal asymptotic stress pattern in eqs. 4.4,4.5 and4.6, we can solve for "*optimal continuum density*" of dislocations, $b(r)$ using modified Föppl- von Kàrmàn eq. for the known asymptotic stress pattern, σ_{ii}^{c}, related to highly defective crystal in the continuum limit,

$$Y^{-1}\nabla_{\perp}^{2}\sigma_{ii}^{c} = -K_G + s\delta^2(\mathbf{r}) - \nabla_{\perp} \times \mathbf{b}(\mathbf{x}) \tag{4.7}$$

Here we expect that the effective topological charge of scars is controlled by the fixed charge of disclination, Gaussian curvature and the stress-free fields. After integrating the compatibility equation for the coarse grained dislocation density, $b(r)$, we have:

$$b(r) = \frac{-C^{'}}{r^2} + \frac{K_G}{2}r + \frac{C_b}{r} - (\frac{\pi/3}{2\pi})\frac{1}{r} \tag{4.8}$$

where continuum dislocation density $b(r)$ is related to the spacing, $D(r)$ between dislocations along the scar characterized by, $D(r) = n_s|b|/2\pi r b(r)$ in terms of scar number n_s. Matching the discontinuity in $\nabla \cdot \sigma$ at $r = L_1, L_2$, given $C^{'} = \frac{1}{24}L_1\left(3K_G L_1^2 - 2\right)$ using the stress continuity at $r = L_1$ leads to $C_b = 0$ and $s^{'} = \frac{\pi/3}{4\pi}$ which is equal to the charge of the centered 5-fold disclination (see appendix I for coefficients). This indicates that in the presence of scars, the topology of the spherical cap with centered disclination remains intact and scar patterns exhibit a local mechanism in stress relaxations. Further investigation of equation 4.44, shows that the dislocation density changes its sign at the radial distance $r_*/W = 1/\sqrt{3K_G W^2}$. This shows for large enough Gaussian curvature, $K_G W^2 > 1/3$, achieving this certain pattern of dislocation density becomes plausible by introducing two families of dislocation with opposite polarizations. In the second stress zone scars structure consists of dislocations in $r = L_1 ... r_*$ region with Burgers vector orientation, $\mathbf{b} = -b\hat{\theta}$ and in the $r = r_* ... L_2$ region we have the opposite dislocation polarization with $\mathbf{b} = b\hat{\theta}$ similar to the compressive dislocations. In general set of six equations related to boundary conditions on

stress field are quite cumbersome and there is no general analytical solution for these coefficients but we can make progress in the limit of small tension $T \to 0^+, L_2 \to W$, which leads to a general equation,

$$\begin{aligned} & \left[\frac{s}{4\pi}\right] \frac{2W^2}{W^2+L_2^2} \ln\left(L_2/W\right) + \left[\frac{s}{4\pi}\right] \frac{W^2-L_2^2}{W^2+L_2^2} + \frac{K_G W^2}{8} \frac{\left(W^2-L_2^2\right)^2}{W^2+L_2^2} + \frac{2W^2}{W^2+L_2^2} T \\ = \quad & \left[K_G L_1^2/8 - \left(\frac{s}{4\pi}\right)\right] \left(L_1/L_2\right) \end{aligned} \tag{4.9}$$

This relation which govern the length of the scarred zone, controlled by the topological charge of the cap, s and external stresses, can also describe the neutral pattern of scars by setting $s = 0$. Furthermore by replacing T to $-P$, this relation describes the scar length in presence of compression. For instance for the limit of vanishing tension and $L_2 = W$ this yields to the equation,

$$\frac{sL_1}{4\pi} - \frac{K_G L_1^3}{8} + \frac{TW}{Y} = 0 \tag{4.10}$$

which leads to $L_1 = 0, L_1/W = \sqrt{2/3}\left(K_G W^2\right)^{-1/2}$ for $T \to 0$ which is similar to the case of compression at the boundary in appendix II. Hence, eq. 4.9 can describes neutral and charged relaxed states in presence of compression and tension.

Here we make an assumption that $L_1 = 0$ that region around the centered five-fold disclination with divergent stress vanishes, and the stress pattern is governed by two regions, asymptotically stress collapsed region, $r = 0...L_2$ which is given by eq. 4.5 and the outer zone dictated by eq. 4.6. We show that $L_1 = 0$ is a valid assumption for any values of tension by using our numerical scheme in the next section and we show that for any tension the first zone, $0 < r < L_1$ is unstable and $L_1 \approx 0$ similar to the small tension limit in eq. 4.10. We also show in the appendix that dominant energy related to three zone solution is a stricktly decresing function of L_1. The dominant energy plots related to dominant stress patterns given in eq. 4.4-4.6 are illustrated in fig. 4.6 b,c, which shows relaxed states with vanishing L_1 is favorable energetically. This is intuitive, since $L_1 = 0$ leads to relaxation of logarithmically divergent stress field of disinclination at the center.

This leads to a major consequence that in the stress collapsed zone, the radial stress, $\sigma_{rr}^{II}/Y = C'/r$, vanishes, since we have $C'(L_1 = 0) = 0$ (see eqs. 4.39). This is the manifestation of

the existence of a unique asymptotically stress pattern in which both radial and hoop stresses are collapsed. Hence the dominant contribution to the elastic energy vanishes in this limit. By assuming $L_1 = 0$ we have six boundary conditions and six unknown based on eqs. 4.5, 4.6 ,and 4.39. Matching the hoop stress at $r = L_2$, determine coefficient B given $C = T - B/W^2$ and matching the radial component of stress at $r = L_2$ gives a transcendental equation for L_2 which determines the scar length,

$$2\left[1-(L_2/W)^2\right] + 3K_g W^2\left[1-(L_2/W)^2\right]^2 + 4\ln(L_2/W) + 48T/Y = 0 \tag{4.11}$$

We numerically solve this relation for L_2 (dashed curve in fig 4.3 (c)) but we can simply look at two important limits. First in absence of tension $T = 0$, leads to $L_2 = W$ that indicates the scar length is equal to the cap size. On the other hand in the limit of large tension, expansion of eq. 4.11 gives the scar length, $L_2 = W\exp\left[1/2 - 12T/Y - 3K_G W^2/4\right]$. This shows that there exists no finite critical tension above which axially symmetric defect-free solution become stable and always dislocations are stable at the vicinity of five-fold disclination. Non-existence of critical tension is in contrast to the case of neutral scars where there is critical tension $T_*/Y = K_G W^2/8$, above which the defect-free stretched sheet is stable (see chapter II and [154] for details). In the other limit we focus in the limit of small tension $T \to 0$ and $L_2 \to W$ and expand the eq. 4.11 which leads to the relation that governs the scar length,

$$\ell_s = L_2 = W\left[1 - 2\sqrt{\frac{(3T/Y)}{1-3K_g W^2}} - \frac{6T}{1-3K_g W^2}\right] \tag{4.12}$$

This enables us to evaluate the total number of dislocations N_d, by integrating the dislocation density $\rho(r,T) = b(r,T)/|b|$ over the length of scars for small T and $K_G W^2 > 1/3$ yielding,

$$N_d = n_d N_{scr} = \frac{2\pi}{|b|}\int_0^{\ell_s} r b(r)dr = \frac{\ell_s}{|b|}\left[\frac{\pi}{3} - \pi K_g \ell_s^2/3\right] \tag{4.13}$$

This relation for the total number of dislocations shows that the excess disclinaiton on the cap with larger curvature stabilizes fewer dislocations, compared to a system with shallower curvature

and a larger number of tensile dislocations. This relation shows that in the continuum limit, dislocation number grows unbounded and we reach the asymptotic limit where highly defective state is faithfully described by stress relaxed state. This relation holds true for $K_G W^2 < 1/3$ and for larger curvatures we need to consider populating certain length of scars, $(1/\sqrt{3K_G W^2} < r < \ell_s)$, with opposite dislocation polarization, due to the facts that $b(r)$ changes its sign for $K_G W^2 > 1/3$ (see Appendix I).

Worth mentioning that the transcendental eq. in 4.11 can be mapped to a stress relaxed state described by compressive stress at the boundary by replacing tension T to, $-P$. This new state of stress exist for large enough curvature, illustrated by dashed region in fig 4.4. There exist another relaxed state of stress which underlies charged scars with compressive boundary force that leads to stress relaxation close to the boundary of the crystal. We will show in the next section that the state corresponds to stress relaxation at the periphery is energetically favorable compare to the state described by charged scars bounded to the centered disclination. Details of the stable state is analyzed in the appendix II and next section.

As we will depict in the next section, remarkably highly-defective state, described by the asymptotic stress relaxation gives rise to a simple *dominant* elastic energy, E_{dom} that is finite and well defined (except for vanishing σ_b) in the continuum limit in which the unit cell size is much smaller than cap size. Imperfect relaxation of geometric stresses by discrete dislocations is related to the *sub-dominont* scale in elastic energy, E_{sub}, with the asymptotic behavior given by, $\lim_{b/W\to 0} E_{sub}/E_{dom} = 0$. In section IV. b, we derive explicitly how this split in energy scales is possible. The energy scaling fails in the singular limit of vanishing boundary forces, $\sigma_b = 0$, where the dominant energy vanishes and only non-vanishing contribution is, E_{sub} (section IV. b). This separation in scales is universal in a sense that exists both for "elastic" modes of out-of-plane shape deformations (*e.g.* wirnkling) and the "plastic reorganization of lattice packing facilitated by topologically "neutral and "charged" arrays of defects [132].

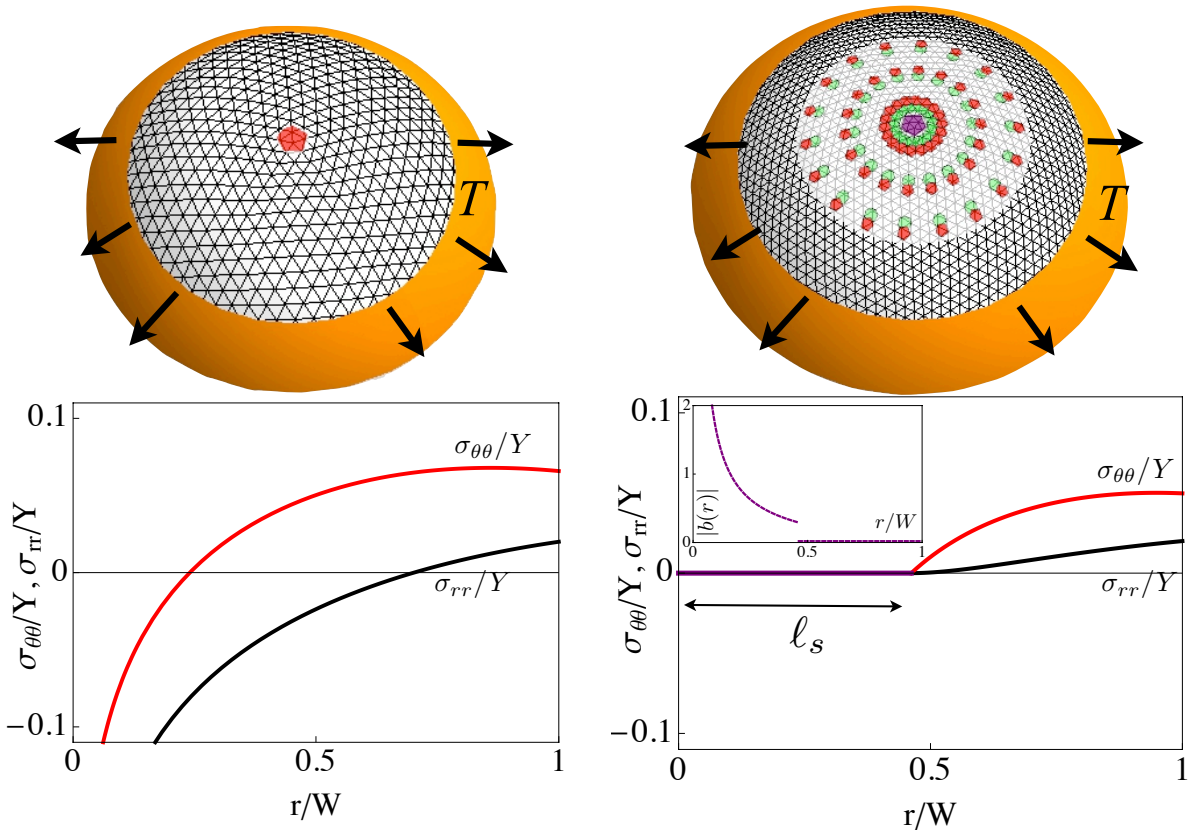

Figure 4.2. Axi-symmetry state of radial and azimuthal stress fields for centered 5-fold disclination and asymptotic stress relaxed states in presence of charged scars with length ℓ_s on a stretched crystalline sheet for $T/Y = 0.02$ and $K_G W^2 = 0.3$. Inset illustrates the corresponding plot for the continuum distribution of dislocations.

4.2.2 Neutral scars in presence of compression

We showed that for large curvature the "charge neutrality" of the lattice is broken by formation of an excess 5−fold disclination and how external fields can rearrange the multi-dislocation patterns. Here the natural question is identifying the role of neutral scars for shallow surface coverage in the presence of the compressive stresses (the effect tensile strains studied in the last chapter). First we show how to construct a stress collapse solution for the case of neutral scar patterns. Following the mechanism that we developed in the last section, we find that tension-free region, in which neutral scars emerge at the center of the confined sheet is governed by,

$$(0 < r < L) : \sigma_{rr}^{I_n}/Y = C'/r; \sigma_{\theta\theta}^{I_n} = 0 \tag{4.14}$$

and for the outer zone where we need to satisfy the compressive boundary condition $\sigma_{rr}(r = W) = P$ we obtain,

$$\begin{aligned} \sigma_{rr}^{II_n}/Y &= \frac{1}{16R^2}(W^2 - r^2) + \frac{B}{r^2} + C; \\ \sigma_{\theta\theta}^{II_n}/Y &= \frac{1}{16R^2}(W^2 - 3r^2) - \frac{B}{r^2} + C \end{aligned} \tag{4.15}$$

where the second term in the stress relations, $\propto 1/r^2$ is necessary to satisfy the compressive strain at the boundary (similar to the outer zone for charged scars in the last section). Using vanishing hoop stress at $r = L$, $\sigma_{\theta\theta}^{n}(r = L) = 0$ and assuming a finite radial stress at the center of the sheet, leads to $C' = 0$ and $C = B/L^2 + K_g\left(3L^2 - W^2\right)/16$. On the other non-divergent radial stress in the center imply the boundary condition $\sigma_{rr}^{II_n}(r = L) = 0$ that sets $B = -K_g L^4/16$. Finally $\sigma_{rr}^{II_n}(r = W) = P$ governs the scar length $L = \ell_s^n$,

$$\ell_s^n = \sqrt{W - \frac{4\sqrt{P/Y}}{\sqrt{K_g}}} \tag{4.16}$$

This relation determines a critical compression $P_*^n/Y = -K_g W^2/16$ above which asymptotic stress solutions do not exist and compressed defect free sheets can be stable relative to the scarred

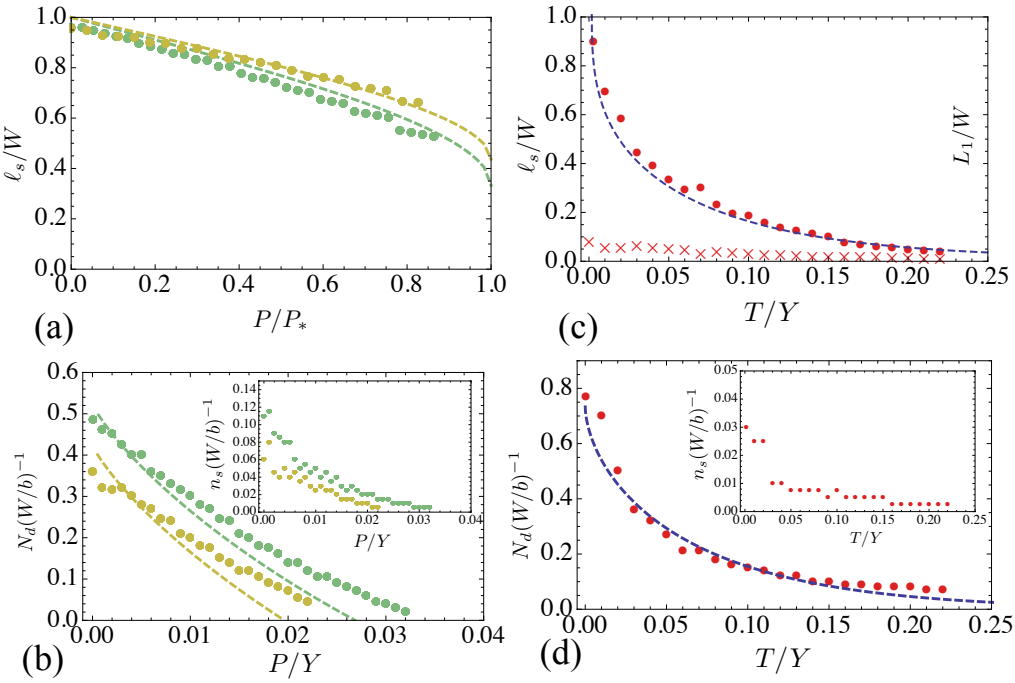

Figure 4.3. (a) shows energy minimization and analytical results for the length of scarred zone ℓ_s and (b) shows the total number of dislocation N_d scaled by the system size, (b/W). n-fold symmetric simulation results (points) and analytical predictions (dashed curves) are plotted according to the stress-collapse solution (dashed curves) for $K_G W^2 = 0.5, 0.6$ and $b/W = 0.0025$.(c) shows scar length ℓ_s and L_1 (points and crosses) for $K_G W^2 = 0.3$ and scaled dislocation number in (d). Insets show scar numbers with same scaling factor used for the total dislocation number.

ones. The critical P_*^n is half the critical tension needs to stabilized the defect free stretched sheet, $T_*/Y = K_G W^2/8$, nevertheless both critical values scales linearly with the Gaussian curvature and stretching moduli Y.

4.3 Discrete dislocation simulations

In the last sections we predicted that, existence of the underlying dominant stress-collapse solution, eq. 4.48 and 4.6, in the presence of an excess disclination leads to new predictions for the scar length in eq. 4.49 and dislocation number. But in general these predictions need to be tested explicitly by including defects as singular sources of the stress in the bi-harmonic relation and solve exactly for their elastic stresses and interactions. Strictly speaking, this is not trivial in general that

stresses and energetics of far-from-threshold solutions as an *effective field theory* can be mapped exactly to the N_d-body problem of N_d singular dislocations interacting via long-range potential in spherical geometry with small but finite unit cell size, thereby limits of the validation of asymptotic solutions needs to be known. These interactions were calculated analytically in [136, 137] in terms the Greens function of the biharmonic equation subject to vanishing normal stress (see last chapter for details).

Here we examine these far-from-threshold asymptotic conjectures, by performing "n-fold dislocation pattern" simulations similar to the method presented in section 3.4 and [154], where the azimuthal positions of the dislocations are constrained to n-fold symmetric scars, and we perform the descent minimization with respect to the number of dislocation, number of scars and radial position of the dislocations for given values of surface coverage $K_G W^2 = 0.3 - 0.6$ and lattice spacing $a/W = 0.0025 - 0.005$. Simulations performed for both tensional and compressional field in presence of excess disclination. We need to modify the total elastic energy, eq. (3.11) in the numerical minimization to account for the presence of centered five-fold disclination and rotating the Burgers vector by π to account for the right polarization of tensile dislocations for compressive strain at the boundary. In this case we refer to the general expression in eq. 4.17 where the pairwise interaction of two disclinations with topological charges $s_{\alpha,\beta}$ at $r_{\alpha,\beta}$ is calculated (see [136] for details),

$$\begin{aligned} E\left(s_\alpha, r_\alpha; s_\beta, r_\beta\right)/Y &= \sum_\alpha \frac{s_\alpha}{32\pi}\Big[\frac{s_\alpha}{\pi} - \frac{K_G W^2}{2}\Big]\Big(1 - \frac{r_\alpha^2}{W^2}\Big) \\ &+ \frac{1}{2}\sum_{\alpha\neq\beta} s_\alpha V_{int}(x_\alpha, x_\beta) s_\beta, \end{aligned} \tag{4.17}$$

where V_{int} is the pairwise disclination interaction,

$$\begin{aligned} e^d_{int}(x_\alpha, x_\beta) = \frac{1}{16\pi^2}\Big(1 - \frac{r_\alpha^2}{W^2}\Big)\Big(1 - \frac{r_\beta^2}{W^2}\Big) \\ + \frac{|\Delta x_{\alpha\beta}|^2}{16\pi^2 W^2} \ln\left[\frac{|\Delta x_{\alpha\beta}|^2}{(W^2 - r_\alpha^2)(W^2 - r_\beta^2)/W^2 + |\Delta x_{\alpha\beta}|^2}\right] \end{aligned} \tag{4.18}$$

and $\Delta x_{\alpha\beta} = x_\alpha - x_\beta$. Here we consider $r_\alpha = 0$ and $s_\alpha = +\pi/3$, as a centered five-fold disclination and sum over all disclination dipoles (dislocations) that are given by $s_\beta = \pi/3$ sitting at $r_\beta - a/2$ and $s_\beta = -\pi/3$ sitting at $r_\beta + a/2$. In fig. 4.3 we plot the results of n-fold simulations for scar length ℓ_s, dislocation number N_d and n_s scar number, versus the predictions of the asymptotic stress-free field theory. The agreement of these numerical results with features predicted by the asymptotic study indicate that dominant stress pattern governs the scar length and dislocation number and shows that the state of "perfect screening" is achievable by the symmetric patterns of dislocation scars. Fig.4.3 (a) indicates that there exists a critical compression above which all the dislocations annihilate and single five-fold disclination relieve the total frustration of the system. This critical compression, $P_* = Y/27\left(\sqrt{2K_G W^2}\right)$, depends on the curvature of the cap and for larger curvatures. The critical compression can be reached faster for large curvature compared to caps with shallower curvature. Fig. 4.3(a) shows that at zero compression all the dislocations are tightly bounded to the central disclination and as imposed boundary compression reaches $\approx P_*$ the length of the defective region vanishes. Further investigation of the structure of the scarred zone indicates that the total number of dislocations decreases as the surface coverage of the spherical cap grows, which agrees with the behavior of eq. 4.54 (see fig. 4.3b). In contrast to the critical behavior of the compressional field in stabilizing the defect-free axi-symmtric state, fig 4.3 (c) shows there exists no finite tension above which bare disclination becomes stable.

4.4 Energetics of neutral-charged scar transition

The focus of the present section is to consider how appearance of excess disclinations (beyond small curvature) modifies the underlying dominant-subdominant energetics associated to neutral and charged scar patterns of highly-curved caps, and thereby, alter the energetic stability of multi-dislocation stress relaxed states and axi-symmetric states. The focus is on the curvature-driven transition from uncharged to charged dislocations scar patterns on crystalline caps. The fundamental role played by boundary forces and Gaussian curvature as independent control parameters in selecting certain dislocation pattens identified by neutral and charged scars will be explored. In presence of external tensional and compressional fields, the dominant energetics, E_{dom}, character-

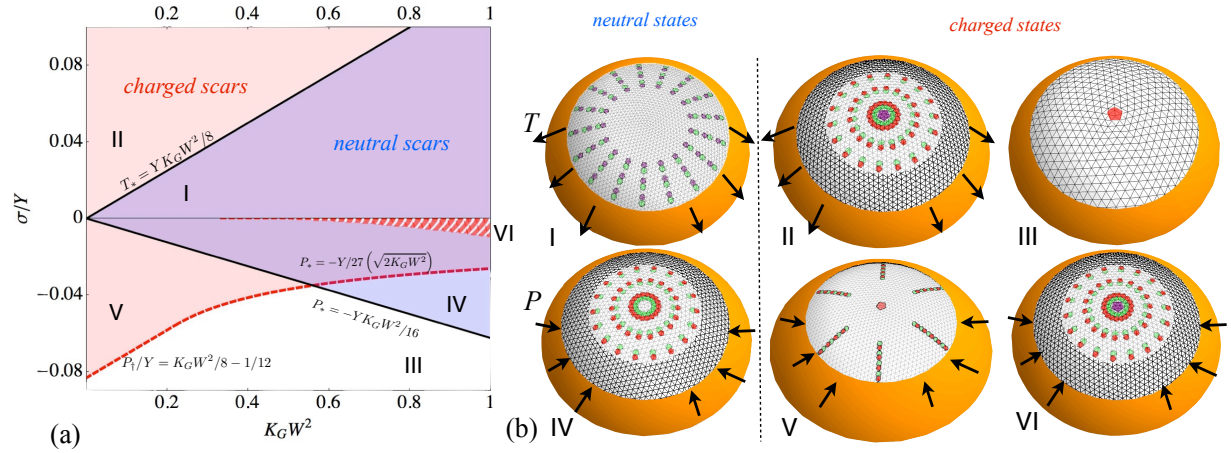

Figure 4.4. (a) depicts the phase space spanned by two independent parameters, surface coverage, K_GW^2 and boundary stresses $\sigma_b = [T, -P]$. The blue region of the phase space highlights the region where neutral scars described by the stress-relaxed state can exist (described by states I, IV). This region is bounded by two critical solid lines $T < T_*$ and $P > P_{**}$. Dominant region in the phase diagram, colored red and bounded by dashed critical curve in the compressive region characterizes the existence of charged scarred sheets. The red dashed region for $\sigma_b < 0$ indicates the existence of a state where charged scars lead to stress relaxation close to the centered disclination (IV). Dot-dashed line represents the critical line below which the axi-symmetric state with bare disclination is stable compare to the defect free state. (b) shows the schematics of six possible states described in different regions of phase space in (a) including neutral and charged scars in stretched and compressed crystalline sheets and bare disclination with compression and tension at the boundary (III).

ized by asymptotic stress relaxed states govern the a curvature-induced transition from "*neutral*" to "*charged*" scar state. Dominant energetics of highly defective cap, explicitly described by the asymptotic stress relaxed solutions, σ^D given in the last section for non-vanishing σ_b (also see appendix II for compressed sheet), $E_{dom} = \pi \int \sigma^D_{ii} u^D_{ii} dr - 2\pi\sigma W u^D_r(r = W)$ with u^D is the strain fields correspond to asymptotic stress relaxed state. This leads to a morphological phase diagram in terms of surface coverage and boundary stresses (tension and compression) that illustrate the stability of charged and neutral scars in stretched and compressed crystalline sheets.

4.4.1 Dominant energy of relaxed states

Tensional Field: First we focus on the dominant part of elastic energy related to the asymptotic stress solutions for neutral and charged scar for external tensional field. We compute the form of the dominant energy stored in the elastic energy of the asymptotic stress pattern, which is realized in the singular, continuum limit $b/W \to 0$ ($N_d \to \infty$), The dominant energy follows from the solutions of stress, strain and displacement fields corresponding to solutions in eqs. 4.5, 4.6, which split into two zones, a defect-free zone for $r > L_2$, and inner zone solutions related to the stress collapsed states,

$$E^c_{dom} = \pi \int_0^{L_2} \left(\sigma^{IIc}_{ii} u^{IIc}_{ii}\right) + \pi \int_W^{L_2} \left(\sigma^{IIIc}_{ii} u^{IIIc}_{ii}\right) - 2\pi T W u^{IIIc}_r (r = W) \tag{4.19}$$

The first term due to the collapse of both radial and hoop stress vanishes and solution of L_2 is the solution of eq. 4.11. In the well-defined and tractable limit of small tension $T \to 0$ and $L_2 \to W$ the solution for asymptotic L_2 is given in eq. 4.12 and the dominant energetic to the leading orders in T becomes,

$$\begin{aligned} E^c_{dom} &= \frac{\pi W^2 Y}{3} K_g W^2 (T/Y) + \frac{2\pi W^2 Y}{3} \left[\sqrt{\frac{1}{3} - K_g W^2}\right] (T/Y)^{3/2} \\ &+ \frac{2\pi W^2 Y}{3} \frac{T^{5/2}}{\sqrt{1/3 - K_G W^2}} - \frac{6\pi W^2 Y}{1 - 3K_G W^2} (T/Y)^3 \end{aligned} \tag{4.20}$$

Here we characterize the transition in dominant energetics of charged scars to neutral scars in the limit of small tension. Analysis in the last chapter (see [154]) on neutral scar patterns on the stretched crystalline sheet shows that the neutral scar energy related to asymptotic stress collapse solution is given by,

$$E^n_{dom} = \frac{\pi T W^2}{6Y} \left[3(2\nu - 3)T + 2K_g W^2 Y + 4T \ln\left(\frac{2T}{K_g W^2 Y}\right)\right], \tag{4.21}$$

By further investigation of eqs. 4.20 and 4.21 in the limit of small tension $T \to 0$, one can show, $E^n_{dom} < E^c_{dom}$ for $T \neq 0$, which means for any surface coverage $K_g W^2$, and finite values of tension, the charged scar pattern is unstable to the neutral scar morphology. This result holds for any values of tension and can be shown also by numerically solving relation that govern the scar length in eq. 4.11 and integrating eq. 4.19. Hence, mechanical strain given by tension, dictates the stability of neutral scar independent from the gaussian curvature. This surprising stability of neutral states, is related to the higher energetic cost of charged scars, $\sim T^{3/2}$ (second term in eq. 4.20), compare to the lower elastic cost of neutral patterns that scales as $\sim T^2$. Nonetheless, for vanishingly small values of tension we need to account for sub-dominant energetic which can affect the stability of neutral scars, which is the focus of next section.

Compressive field: The dominant energy calculation in presence compression at the boundary is similar to the method that presented in the last section and we will use asymptotic stress relation given in eqs. 4.48 in the appendix II, For the case of charged scar we have.

$$E^c_{dom} = \pi \int_0^L \left(\bar{\sigma}^{I_c}_{ii} \bar{u}^{I_c}_{ii} \right) + \pi \int_L^W \left(\bar{\sigma}^{II_c}_{rr} \bar{u}^{II_c}_{rr} \right) + 2\pi P W \bar{u}^{II_c}_r (r = W) \tag{4.22}$$

where $\bar{\sigma}/\bar{u}$ indicates stress/strain fields related to compressional fields. Integrating the first and second terms in the elastic energy yields,

$$\begin{aligned} \bar{E}^c_{dom} &= \pi \int_0^L \left(\bar{\sigma}^{I_c}_{ii} \bar{u}^{I_c}_{ii} \right) + \pi \int_L^W \left(\bar{\sigma}^{II_c}_{rr} \bar{u}^{II_c}_{rr} \right) \\ &= \frac{\pi L^2 Y}{1152} \left[3K_g L^2 \left(K_g L^2 - 2 \right) + 4 \right] - \pi(\nu - 1) P^2 W^2 / Y + \pi P^2 W^2 \ln \left(W/L \right) / Y \\ &+ 2\pi P W \bar{u}^{II_c}_r (r = W) \end{aligned} \tag{4.23}$$

Third term in the elastic energy, eq. 4.22, depends on the displacement field which characterizes the work done by the external compression at the boundary of the crystal. In order to find the radial displacement field for the scarred cap with centered disinclination, $\bar{u}^{II_c}_r$, we first calculate the

strain of the outer zone governed by the stress-free solutions in eq. 4.48. The detailed calculation is reported in appendix II.

$$\bar{u}_r^{II_c}(r=W) = -1/6K_G W^3 + PW/Y\left[(\nu-1) - \ln(W/L)\right] + K_G L^3/24 - L/12 \tag{4.24}$$

Here L is the solution to the equation 4.49 that governs the position of the scar tip. Similarly for the neutral scar morphology with compressive strain at the boundary, with the aid of stress relations in eqs. 4.14 and 4.15 we have,

$$\bar{E}^n_{dom} = \frac{\pi P W^2}{3}\left[-K_g \ell_s^n W + 4\sqrt{K_g P/Y}(\ell_s^n - W) + 3P(\nu+1)/Y\right] \tag{4.25}$$

where ℓ_s^n is the length of the neutral scar in eq. 4.16. For any finite value of compression, $\bar{E}^c_{dom} < \bar{E}^n_{dom}$ and charged scar morphology is always preferable energetically. This is related to the fact that to leading orders in P, energetic cost of introducing neutral scars scales as $\sim P^{3/2}$, but for the case of charged scars, eq. 4.23 shows a lower elastic cost which scales as $\sim P^2$ as we approach the singular limit of $P \to 0^-$. This is similar to case of stability of neutral scars compare to charged scars for stretched sheets, where the same scaling appears for the elastic cost of pulling the charged scar tips away from the crystalline boundary with external tension T in eq. 4.19. This suggests that system always select the dislocation morphologies with scar ends bounded to the boundary, which is an intuitive result considering the screening effect of the boundary. This is analogous to the electrostatic problem where charge dipoles are attracted to a nearby plane with constant potential (akin to the constant stress, σ_b), du to the the polarized charges that induced by electrostatic dipoles. In section IV. B, we show how this high elastic cost, $\sim \sigma_b^{3/2}$, can be derived alternatively via interaction between scar tips as the external field σ_b, pulls the scar tips away from the boundary for charged scars on the stretched sheet and neutral patterns for compressed sheets.

Finally to obtain a consistent picture for the phase diagram that illustrate the relative stability of all the accessible states (see fig. 4.4), we compute the elastic energy of axi-symmetric (*uncollapsed*

stress fields) for dislocation-free state with 5-fold disclinaiton. In the next section we discuss the relative stability of these states compare to defective ones. Using relations for stress fields induced by Gaussian curvature and disclination for (defect-free axi-symmteric states), eq., 4.2, yields elastic contribution to the dominant scale,

$$E_{dom}^{axi} = \pi W^2 \left[\frac{Y K_G^2 W^4}{384} + \frac{K_G W^2 \sigma_b}{4} + \sigma_b^2 (\nu - 1)/Y \right] \tag{4.26}$$

$$E_{dom}^{5fold-axi} = \pi W^2 \left[\frac{1}{288} + \frac{1}{6}\sigma_b + \sigma_b^2 (\nu - 1)/Y + \frac{1}{1152} \left(3Y K_G^2 W^4 - 6 K_G W^2 \left[Y - 48\sigma_b \right] \right) \right] \tag{4.27}$$

where σ_b is the imposed boundary force, needs to be set to $-P$ for the compression and T for the tensile stress. One can imagine the limit where dislocation core energy is very high for crystal with lattice spacing comparable to the system size. Consequently, dislocations are not stable and the only two competing states are defect-free axi-symmteric states with and without disclinaiton with energetics described by eq. 4.26. Comparison between E_{dom}^{axi} and $E_{dom}^{5fold-axi}$ characterizes a phase boundary in the plane spanned by $K_G W^2$ and σ_b/Y, given by $\sigma_b^*/Y = (3K_G - 2)/96$, which indicates there exist a critical generalized stress below which bare 5-fold disinclination is stable. The dot-dashed line in figure 4.4a, marks $\sigma_b^*(K_g W^2)$ in the phase digram.

Comparison between the dominant part of the energy for charged and neutral scars leads to the phase diagram depicted in fig. 4.5 which is spanned by two independent parameters, Gaussian curvature and external boundary forces. For the case of non-vanishing compression, comparing comparing the sub-dominant energies of the neutral and charges scars, eq. 4.23 and 4.25 reveals that neutral scars are not stable relative to charged scars, consequently charged scars are always preferable energetically. For large enough compression above the critical values, given by $P < -Y/27\sqrt{K_G W^2}$ for large curvature and $P < Y(K_G W^2/8 - 1/12)$ for small curvature, energetics of axi-symmetric state in eq. 4.26 drives the stability of bare 5-fold disclinaiton.

Phase diagrams: Two antagonistic parameters boundary stress, σ_b and surface coverage $K_G W^2$ related to the measure of mechanical strain and geometrical confinement in the curved crystal,

enable us to span two phase diagrams in fig. 4.5 for compressional and tensional boundary forces. These phase diagrams illustrate the stability of different states of stress including *charged* and *neutral* scar morphologies, axially symmetric state of bare disinclination and defect-free state.

A phase diagram in fig. 4.5 (a) for tensile boundary stresses illustrates the stability of neutral scars for any value of curvature in presence of finite tension. The critical line that is given by $T_* = YK_GW^2/8$ indicates the values of tension above which defect-free axi-symmetirc state is stable compare to neutral scarred sheets, consequently stretched sheet remains stable . For large tension $T > T_*$, and small curvature energy of charged scars in eq. 4.19 is larger than the cost of axi-symmetric state, consequently stretched sheet remains stable.

Figure 4.5 (a) shows the similar phase diagram for applying external compression to the boundary. The transition line $P(K_GW^2)$ marks the onset of a significant stability of charged scars for any values of surface coverage for sufficiently small compressions. For large curvatures transition curve is characterized by $P < -Y/27\sqrt{K_GW^2}$ and $P < Y(K_GW^2/8 - 1/12)$ sets the transition line for small curvature. The predicted transition line points out that dominant energetics always favors charged scars over neutral dislocations. For sufficiently large compression, depicted by the dashed line accounts for the reentrant of stable bare disinclination characterized by axially symmetric state of the stress. The dominance of a single state for finite σ_b, charged scars in presence of compressive boundary forces and and neutral ones with tensile forces, over a large range of surface coverage (almost every where) might seem anomalous. However, this indicates a universal morphological selection by which system always selects the scarred state with specific underlying stress pattern, characterized by stress relaxation in the outer zone of the cap which is close to the boundary. The behavior of phase diagram for the nonvenishing σ_b, described by phase transitions purely controlled by generalized boundary forces expose the central role of σ_b in dictating the stable states, thereby, conceal the effect of geometrical strains induced by Gaussian curvature.

Although, surprisingly this phase diagram shows that the stability of states described by scars which does not terminate at the boundary, are suppressed by presence of the boundary forces, approaching zero boundary forces $\sigma_b \to 0$ separation in energy scales breaks, since dominant energetics approaches zero, $\lim_{P\to 0} E_{dom} = 0$ due to complete collapse of dominant stress throughout

the sheet. Near to this singular zero force boundary, the subdominant energetics can *enhance* the stability of neutral scars for vanishingly small external forces (see discussion at the end of the next section).

4.4.2 Hierarchy of energy scales

In this section we prove how summation of interacting dislocations can be divided in to two distinct scales of elastic energy, related to scar-scar interaction and scar self-energy. We predicate our analysis on the appearance of the energy hierarchy which relates the subdominant scale of the energy, E_{sub}, to the scar self-energy and the dominant and subdominant part of the energy to the scar-scar interaction. Hence, investigating the relative stability of the charged vs. neutral scar patterns can be characterized by comparing the scar self energy for these two states in the limit of infinite confinement or zero tension. Approaching the high confinement regime ($T, P \to 0$) leads to complete collapse of the dominant stress field in the crystalline cap. The complexity of this singular limit is related to fact that dominant energy of the system becomes vanishing small and we need to consider the subdominant scales of the energies that are related to small but finite size of the unit cell of the crystal. Furthermore the mechanism which underlies the breaking of the "charge neutrality" of the curved crystal (transition from neutral to charge scar) purely induced by change in Gaussian curvature (for zero boundary forces) is intimately related to different scales of the elastic energy. This becomes transparent by identifying the relative scale of inter-scar, intra-scar interaction in the limit of infinite confinement.

Dominant energetics of highly defective cap simply described by the asymptotic stress relaxed solutions, σ^D given in the last section for non-vanishing σ_b. Alternatively this total dominant energy of dislocation scar patterns on curved crystals can be described by the sum of three different energy contributions, including energy of defect-free axi-symmetric state, E_{axi}, interaction energy of 5-fold disclination and scars, $E_{dis-scar}$, and the energy gain of scars. But this energy fails to describe correctly the micro structure of the defective crystal, since it does not depend on the lattice structure. In contrast scar self-energy is the sub-dominant cost of introducing dislocations with dipolar length, b, equal to the lattice spacing. In the next section, we compute this cost by

summing the elastic interactions between all pairs of dislocations along the scar. In the following section we show that strong interaction between scars within the lateral distance contribute mostly to the dominant scale of the energy, but there exist a sub-dominant contribution to scar-scar interaction. On the other hand scar-self energy and interaction between 5-fold disclination and scars are purely sub-dominant and dominant respectively.

Scar interactions and dominant scales: The elastic energy scale of disclination-scar interaction can be estimated by calculating the interaction energy between disclination-like singularities of the scar ends and the centered 5-fold disinclination. Interaction between disclinations of opposite charge in a crystal of size W leads to an elastic gain that scales as $E_{dis-scar} \approx Y s_+ s_-$. Estimating the effective scar charge we have $s_- \approx -(b/W)(N_d/n_s)$ and for the disinclination, $s_+ = \pi/3$. Summing over n_s scars lead to scaling relation for the disclination-scar interaction which becomes $E_{dis-scar} \approx -Y(N_d b/W)\pi/3$. This shows that the disinclination-scar attraction contributes at the dominant scale and has no dependence on scar number or on the microscopic scale, b, identifying these terms with the elastic energy of the asymptotic stress pattern.

Now we turn into the inter-charged scar interaction. In the case of neutral scars and small confinement ($T \approx T_*$), it has been shown in the last chapter, that the scar-scar interaction contributes in the dominant part of elastic energy [132] (see chapter II). Here we aim to exploit that analysis to understand the high elastic cost of pulling the scar ends form the crystal boundary which we showed in the last section, scales with the boundary stress as $\sim \sigma_b^{3/2}$. The scaling argument is based on considering the grain boundary scars terminating inside of the crystal as a source of singularity that is identical to far-field stresses generated by disclinations. This is due to the fact that scar ends disrupt the orientational order if the underlying lattice which mimics the geometric strain induced by disclinations. Each pairs of scar ends interact strongly with the elastic cost that can be estimated by $\sim Y s^2 (W - \ell_s)^2$ where s is the effective topological disclination charge given by $s \sim (b/\ell_s)(N_d/n_s)$. Each scar ends experience a strong repulsion with $n_s(W - \ell_s)/W$ neighbors, which leads to the total elastic cost with the scaling $\sim Y s^2 (W - \ell_s)^3 n_s/W$. Here, $(W - \ell_s)$ characterizes the length of the defect free zone, which is small for scars close to the boundary for

small enough boundary stresses σ_b. This length scales with boundary stresses described by $\sim \sigma_b^{1/2}$ based on small stress expansion in eqs. 4.16 and 4.16 for charged scars in presence of tension and neutral scars with compression. Hence, the elastic scar-scar interaction cost is proportional to $\propto \sigma_b^{3/2}$. Consequently, the preference of the system to select charged scar pattern in presence of compression and neutral scars for the tension at the boundary, is the morphological selection that relies on high elastic scar-scar repulsion of defect morphologies with both scar ends, terminate inside of the crystal.

The analysis in [132] is under the assumption of a narrow radial scarred band near the sheet edge. Here we compute the scar-scar interaction, E_{ss} in the limit of infinite confinement ($T \to 0$, $\ell \to W$) with no approximation in the geometry of the scarred zone. We express, E_{ss} as a double-sum over the elastic interaction between n_s scars separated by ϕ along azimuthal direction $\hat{\theta}$. This contribution to the elastic interaction can be evaluated as a double-sum of dislocation interactions reside on scars that are labeled by k and k', and radial positions of dislocations are labeled by r and r'. It is convenient to convert the dislocation-dislocation interaction E^D_{int} to disinclination interaction e^D_{int} that are the constituent elements of dislocations in the form of $5-7$ dipoles. This can be achieved via, $E^D_{int} = |b|^2 \partial_r \partial_{r'} e^d_{int}$ and by part integration,

$$\begin{aligned} E_{\rm ss}/Y &\approx \sum_{k=1}^{n_s} \sum_{k'=1, k' \neq k}^{n_s} \frac{1}{n_s^2 \epsilon} \int_0^{\ell_s} \tilde{\lambda}(r') dr' \int_0^{\ell_s} \tilde{\lambda}(r) E^D_{int}(r, r') dr = E^{dom}_{ss} + E^{sub}_{ss} \\ &= \int_0^{2\pi} \frac{1}{2\pi} d\phi \frac{|b|^2}{\epsilon} \mathcal{F}(r, r', \phi) = \frac{|b|^2}{\epsilon n_s} \left(\frac{\pi^2}{4} - \frac{s}{K_G W^2} \right) + O(\delta\phi^2) + ... \end{aligned}$$

$$\mathcal{F}(r, r', \phi) = \left[\tilde{\lambda(r)} \tilde{\lambda(r')} e^d_{int}(r, r', \phi) \Big|_{r=0}^{r=\ell_s} \Big|_{r'=0}^{r'=\ell_s} - \int_0^{\ell_s} \int_0^{\ell_s} \partial_r \partial_{r'} \tilde{\lambda}(r) \tilde{\lambda}(r') e^d_{int}(r, r', \phi) \right] \quad (4.28)$$

where $\mathcal{F}(r, r', \phi)$ is a function that depends on e^d_{int}, the pairwise disclination interactions in eq. 4.18 (see appendix IV) and $s = \pi/3$ for the case of charged scars and $s = 0$ obtain $E_{\rm ss}$ for neutral scars. We define $\tilde{\lambda}(r) = \left[\frac{s}{K_G W^2} - \pi r^2 \right]$. Since disclination interactions are well behaved as separation between them approaches zero, we do not need to introduce a cut-off around disclination, in contrast to the case of dislocation where there exist a logarithmic divergence around the dislocation core.

First summation over scars is counted by the factor of n_s. Furthermore, we approximate the second sum over scars, k' by the integral, $\sum_{k=1}^{n_s} F(k) \approx \int_1^{\infty} F(k)dk \approx \int_0^{2\pi}(n_s/2\pi)F(\phi)d\phi$ where $\phi = k(2\pi/n_s)$ is the angular separation between scars. This approximation is valid in the continuum limit where $n_s \to \infty$.

The last term in eq. 4.66 contribution depends on scar number, n_s in contrast to the first term which is independent of the symmetry of the scar pattern. This energy contribution is vanishingly small in the asymptotic, $\lim_{n_s\to\infty} \delta\phi \to 0$ but this contribute to the subdominant part of the energy (next section). We divide scar-scar interaction, E_{ss} to two parts, subdominant part E_{ss}^{sub} and dominant part, $E_{ss}^{dom} = E_{ss} - E_{ss}^{sub}$. Comparing the dominant scale of scar-scar interaction, E_{ss} to the scale of the scar self energy eq. 4.29, shows that in the continuum limit we have, $\lim_{b/W\to 0} E_{ss}^{sub}/E_{ss}^{dom} \approx \epsilon^{1/2}$. This shows that scar-scar interaction contribute in both dominant and subdominant energies.

Scar self-energy and sub-dominant scale: First we present a intuitive scaling argument for characterizing features of the scar self energy, and based on that we present a full calculation of scar self energy aided by Green function of biharmonic relation. Crossing a scar implies rotation of crystal axes by b/D, where D is the dislocation spacing. Hence, scar ends are disclination-like singularities, points around which lattice directions rotate rapidly [138], and the far-field stresses generated by scars are dominated by these end singularities. Estimating dislocation spacing as $D = \ell_s n_s/N_d$ yields two effective disclination charges $s_- \approx b/D \sim (b/\ell_s)(N_d/n_s)$, and the elastic cost to introduce this charges at W and $W - \ell_s$ from the cap edge for two scar ends, correspond to a scar tip that is bounded to centered disclinaiton and another tip, closer to the edge. These self-energy contributions lead to elastic energy $\sim Y\left(s_-^2 W^2 + s_-^2[W-\ell_s]^2\right)$. In addition to the cost of the singular ends, grain boundary scars are characterized by a total "line tension", $\sim Y\ell_s b^2/D\big[\ln(D/b) + E_c\big]$ [138], where E_c parameterizes the inelastic core energies of dislocations, from which we estimate the total charged scar self-energy,

$$E_{\text{self}}/Y \approx n_s^{-1}(N_d b/\ell_s)^2\ell_s^2 + n_s^{-1}[N_d b/(W-\ell_s)]^2(W-\ell_s)^2 + b^2 N_d \ln\left(\frac{N_d\ell_s}{n_s b'}\right) \tag{4.29}$$

where b' is a renormalized core size and $N_d = n_s n_d$ is the total dislocation number. We also used, $\ell_s \to W$ in the limit of infinite confinement ($\sigma_b \to 0$). As mentioned in last section, scar-scar interaction also include a sub-dominant energy contribution, E_{ss}^{sub}, computed in eq. 4.66, which depends on n_s, symmetry of the scar pattern similar to the scar self energy. Total subdominant energetics which depends on micro structure of the lattice, $|b|$, is determined by $E^{sub} = E_{ss}^{sub} + E_{\text{self}}$ and minimizing this sub-dominant part of the energy sets the optimal charged scar number,

$$n_s = \left[N_d + \sqrt{N_d\left(N_d + \kappa\right)}\right]/2 \tag{4.30}$$

where we define $\kappa = \left(\frac{\pi}{3K_G W^2} - \frac{\pi^2}{4}\right)\left(\frac{\pi}{3} - K_g W^2\right)^{-2}$. The optimal scar number leads to the sub-dominant energy scaling to the leading orders in ϵ_c,

$$E^{sub}/Y \approx \frac{b^2\epsilon_c^{-1}}{n_s} + \frac{b^2\epsilon_c^{-1}}{n_s^2} + b^2\epsilon_c^{1/2}\ln[n_s\epsilon_c^{1/2}] \tag{4.31}$$

where we define a parameter $\epsilon_c^{-1/2} = N_d = \ell_s/b\left[\frac{\pi}{3} - \pi K_g\ell_s^2/3\right]$ as a relative measure of disclination charge to the integrated Gaussian curvature. Detailed calculation of multi-dislocation pattern in presence of centered 5−fold disclination is reported in the appendix V. Analysis in the last chapter (also see [154]), shows that the neutral scar self-energy for $n_s^{'}$ scars scales as

$$E^{sub}/Y \approx \frac{b^2\epsilon^{-1}}{n_s^{'}} + b^2\epsilon^{1/2}\ln[n_s^{'}\epsilon^{1/2}] \tag{4.32}$$

where we define $\epsilon = (b/W)^2(K_G W^2)^{-2}$, as the defectability for the neural scars. This relation determines the optimal neutral scar number $n_s^{'} \sim N_d^{'} \sim \epsilon^{-1/2}$ where $N_d^{'}$ is the total dislocation number for the neutral scar configurations. Comparing the dislocation number and the scar number of neutral and charged morphology reveals that presence of excess 5-fold disclination does not break the overall scalings of the geometric features of the spherical cap.

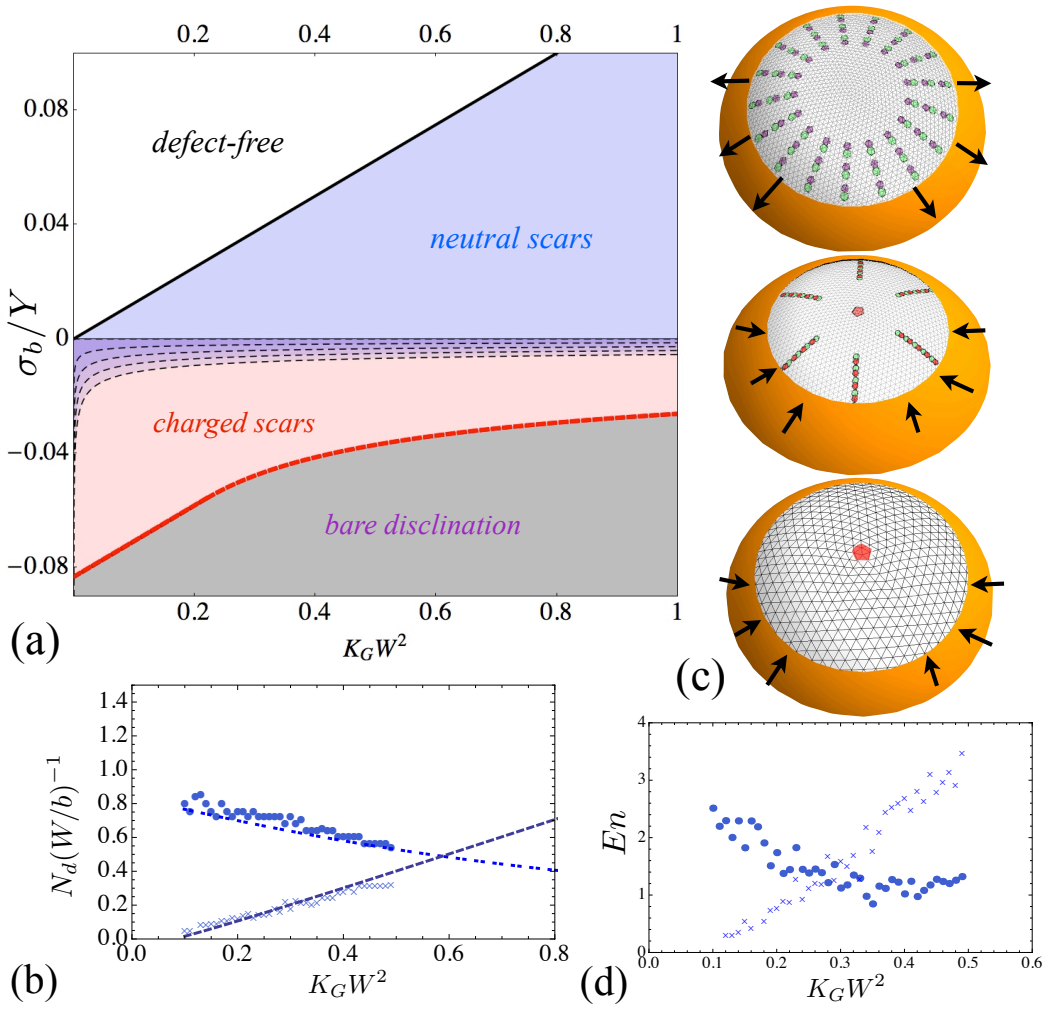

Figure 4.5. (a) shows the phase diagram (tension vs. surface coverage) indicating the onset of dominant stability of the neutral scars for small enough tension below the critical value, T_*. The phase space highlights the significant stability of charged scars for small enough compression and bare disclinaiton for large compressive boundary forces. Dashed lines represent the reentrant of stable neutral scar patterns for small compression (close to infinite confinement limit, $\sigma_b = 0$), related to subdominant energetics for a sequence of lattice spacing $b/W = 0.0002 - 0.001$. (b) shows the scaling behavior of total dislocation number for *charged* vs. *neutral* scars with dashed and double-dashed respectively. Points and crosses represent the result of n_s-fold simulations of multi-dislocation charged and neutral grain boundary scars for the fixed system size of $b/W = 0.005$ for vanishing boundary forces. (c) the schematics of three stable states of neutral scars under tension, charged scars and bare disclination under compression. (d) illustrates the energy of simulated n-fold symmetric multi-dislocation ground states for charged scars (points) and neutral scars (crosses) as a function of surface coverage $K_G W^2$.

In the singular limit of infinite confinement, $\alpha = \sigma_b^*/\sigma \to \infty$, described by the vanishing boundary forces, the charged and neutral scar length is W, which indicates that the length of the defective region is equal to the cap size and dominant stress field is collapsed throughout the sheet. This indicates that the dominant elastic energy of the asymptotic stress pattern vanishes for both charged and neutral dislocation patterns. This shows that these two defective states are degenerate asymptotically. In order to lift this degeneracy in the dominant energetics, we use the subdominant energy computed here. In the continuum limit the scaling law for the energies, $\lim_{b/W\to 0} E^{n,c}_{sub}/E^{n,c}_{dom} \approx \epsilon^{1/2} \to 0$ breaks for $\lim_{\sigma_b\to 0} E^{n,c}_{dom} \to 0$. Consequently characterizing the neutral to charge scar transition is set by the intra-scar energetics and subdominant part of E_{ss}. Strictly speaking, for vanishingly small boundary forces, the dominant energetics approach zero and defective states can be distinguished only by virtue of subdominant energetics, $E^c_{\text{self}} + E^{sub}_{ss}$ (see eqs. 4.31, 4.72 and 4.67).

For vanishingly small boundary forces, the additive subdominant cost of the dislocation self energy is the only non-vanishing energy contribution which drives the stability of charged scars for large curvatures, due to the fact that charged dislocation number decreases (and consequently total dislocation self energy decreases) in contrast to increasing neutral dislocation number. This rough energy estimate fails for charged scars and vanishingly small values of curvature, since the subdominant energy cost related to charged scar-scar interaction (see eq. 4.66) exhibit a power law divergence, $1/K_G$, for zero curvatures. For small enough boundary and non-vanishing compression the scale of dominant energy, becomes comparable to the sub-dominant dislocation cost, E^{sub}. By comparing the total elastic energy of charged and neutral scars, $E^{sub} + E^{dom}$ for small enough compression and small values of curvatures, we can find a critical compression given by,

$$p_* = \frac{1}{4K_G}\left[\frac{4\pi - 3K_G\left(4 + \pi^4 - 4\beta\sqrt{\epsilon}\right)}{\pi\sqrt{\epsilon}}\right]^{2/3} \sim \frac{(\pi/3)^{2/3}}{\epsilon^{1/3}K_G W^2} \tag{4.33}$$

above which neutral scars become stable with $\beta = 4\pi/1152$. This simply means that for sufficiently small boundary compression the divergence in E^{sub}_{ss} enhances the stability of neutral scars relative to charged counterparts for small curvatures that can regularize the anomalous behavior of the

neutral-charged scar stability predicted by dominant energetics as boundary stresses approach zero. As mentioned in the last section the anomaly is related to fact that dominant energetics predicts the significant stability of charged scars on compressed sheet for any values of curvature in contrast to stable neutral scar patterns on stretched crystalline sheets. Hence, E_{ss}^{sub}, recovers the stability of neutral scars for small surface coverage and close enough to singular limit of infinite confinement that can be achieved by $P < P_*$ given by eq. 4.33 The critical dashed lines in fig. 4.5a marks the reentrant of stable neutral scars on compressed sheets which depends on lattice micro structure, b/W.

The curvature induced transition which leads to the breaking of the *chrarge neutrality* of the lattice is characterized by performing n_s-fold simulations for a range of Gaussian curvature for $\sigma_b = 0$. Numerical minimization performed on systems with charged and neutral scars and the energy difference between these states characterizes the transition point on the curvature axes, $\left(K_G W^2\right)_* \approx 0.31$, which characterizes a surface coverage above which charged scars are stable. Furthermore, structural features and asymptotic behavior of charged scars are different from neutral counterparts. In the case of optimal charged scar patterns the growth of the dislocation number and the scar number is governed by, $\epsilon_c^{-1/2}$ which is related to the topological charge of five-fold disclination.

$$n_s \quad \sim \quad N_d \sim \epsilon_c^{-1/2} = (W/b)\left[\frac{\pi}{3} - K_G W^2\right] \tag{4.34}$$

On the other hand for neutral scars we have different scaling for N_d' and n_s',

$$n_s^{'} \quad \sim \quad N_d^{'} \sim \epsilon^{-1/2} = (W/b)(K_G W^2) \tag{4.35}$$

The total optimal number of dislocations, $N_d^{'}$ is increasing linearly with $K_G W^2$ in the ground state configurations populated by neutral scars. In contrast when curvature reaches the transition line (solid line) in fig. 4.5 (a), charged scars become favorable where the total dislocation number, $N_d \approx \epsilon_c^{-1/2}$ is decreasing with the slope of $-K_G W^2$ and optimal packings are governed by smaller number of dislocations. This change in scaling behavior in total dislocation number for *charged* vs.

neutral lattice is shown in fig 4.5b, where the dashed lines are given in eq. 4.34 and 4.35. In fig 4.5b, points and crosses represent the result of simulations for charged and neutral grain boundary scars respectively for vanishing boundary forces.

4.5 Summary

Here we develop a theoretical framework that gives rise to predicting the structure, mechanics and energetics of the defective patterns in the well defined continuum limit. Our study reveals how presence of distinct plastic modes of asymptotic stress relaxation in spherically confined crystalline sheets leads to a morphological phase diagram that illustrate the stability of charged and neutral defect patterns in presence of generalized boundary forces. Small external tensional field stabilizes the neutral scar patterns for any surface coverage and the onset of stability of charged scars occurs for compressional boundary forces. On the other hand for small enough compressive boundary stress charged scars are stable for any values of curvature and bare disclination is energetically favorable for large boundary forces.

We predicated our analysis on the appearance of the energy hierarchy which relates the sub-dominant scale of energy, E_{sub}, to the scar self-energy and the dominant and subdominant part of energy to the scar-scar interaction. We show that in absence of boundary forces this energy hierarchy fails to characterize an energy difference between two topologically distinguishable states, charged and neutral patterns whose dominant elastic energy is strictly zero in the continuum limit, $\lim_{b/W,\sigma_b\to 0} E_{dom} \to 0$. This regime, known as infinite confinement limit, given by $\sigma_b \to 0$, in which geometric strains control the response of curved crystalline sheets. In this limit sub-dominant cost of elastic energy related to the total dislocation self-energy is the only non-vanishing energy contribution that discriminate between "*neutral*" and "*charged*" pattern of scars. Furthermore the subdominant cost can enhances the stability of neutral scars relative to charged ones for vanishing small boundary forces for small values of curvature, since subdominant energy of charged scar-scar interaction, E_{ss}^{sub} diverges as $1/K_G$ for vanishing Gaussian curvature. The predictions for key features of scarred sheets (*e.g.* scar length and symmetry of the patterns) and relative stability of

charged and neutral states provided by asymptotic approach have been examined by numerical minimization scheme based on exact solution of bi-harmonic equation.

We illustrate a morphological phase diagram in which stretched sheets stabilize neutral pattern of scars and compressed crystalline caps drives the stability of charged scars. This shows the central role of boundary forces in breaking the charge neutrality of the lattice with spherical topology and segregating the phase dominated by charged lattice characterized by positively charged bare disclination or decorated by dislocations from the topologically neutral phase stabilizes by tensile boundary forces. Although, the asymmetry of the phase diagram seems surprising that charged morphologies are preferred on the compressive side and neutral ones on the tensile side of the phase, both stable phases, share the same morphological motif in which scars are always bounded to the boundary of the crystal. This is related to high elastic cost of pulling the scars away from the boundary via compressive or tensile stresses.

Neutral and charged phases are connected by the singular limit, $\sigma_b \to 0$, where imperfect relaxation of geometric stresses by discrete dislocations due to small but finite lattice size becomes relevant in selecting between two degenerate states which the relative efficacy of each state be measured via sub-dominant elastic cost of defects.

Our predictions can introduce new directions for experiments related (but not limited) to particle-coated droplets with crystalline structures in which particle packings at the interface can be controlled by tensile or compressive external stresses such as surface tension or confining compressive forces, which gives a robust way to tailor the topology of the lattice that in turn can change the mechanics of the interface.

Revisiting the century old Thomson problem in this context, introduces several key challenges. Specifically, one needs to consider the full covariant elastic formulation which remains valid beyond small slope approximation of our analysis. To date, no analytical solution has been found for the bi-harmonic equation for membranes covering the whole sphere in contrast to the cap with open boundary studied here. One might construct a set of symmetric solutions by decomposing the Thomson problem described by 12 disclination resides at the vertices of an icosahedron to 12 caps with centered disclinaitons and invoke the appropriate boundary forces (and shapes) in order to join

them to the reference manifold. Solution superposition of this type, might provide a new avenue with tractable analytics in the continuum limit, to study the complex spectrum of topological defects on curved manifolds beyond small coverage limit. Although this question remains unexplored that to what extend features of ground state packing of small number of particles inherit from the optimal symmetries predicted in the continuum limit (large particle number).

4.6 Appendix

I. Asymptotic stress fields in presence of tension: In order to fully characterize the asymptotic stress patterns in eq. 4.4, 4.5 and 4.6, we need to determine the coefficients $B, C, C^{'}, C_1, s^{'}$. We have only six boundary conditions by invoking stress continuity at boundary of each region for seven unknowns. Hence all the coefficients can be determined except one, L_1 which we conjecture it to be zero in the next section and provide evidence for this assumption by performing multi-dislocation simulation in section II. Using stress equations,

$$\sigma^{Ic}_{rr,\theta\theta}(r = L_1) = \sigma^{II}_{rr,\theta\theta}(r = L_1) \tag{4.36}$$

$$\sigma^{IIc}_{rr,\theta\theta}(r = L_2) = \sigma^{III}_{rr,\theta\theta}(r = L_2) \tag{4.37}$$

$$\sigma^{IIIc}_{rr}(r = W) = T \tag{4.38}$$

we find the unknown coefficients,

$$C_1 = \frac{1}{24}\left(3K_G L_1^2 - 2\right), \tag{4.39}$$

$$C^{'} = \frac{1}{24} L_1 \left(3K_G L_1^2 - 2\right), \tag{4.40}$$

$$B = -\frac{1}{48} W^2 \left(3K_G W^2 - 24T - 2\right), \tag{4.41}$$

$$C = T - B/W^2 \tag{4.42}$$

where we work in the unit of $Y = 1$ and take the limit $L_2 \to W$ in order to find B (the exact expression used for derivations in the section IIA for $L_1 = 0$). The last unknown is $s^{'}$, the effective discliantion charge that is seen in the third zone eq. 4.6. This effective charge is related to the

dislocation density in the scarred zone. This connection becomes transparent by integrating the compatibility equation and matching the discontinuity in $\partial_r \sigma_{ii}^{Ic,IIc,IIIc}$ at two ends of the scar at $r = L_1, L_2$. In order to find dislocation density we integrate the compatibility relation, given the stress fields in eqs. 4.4,4.5 and4.6 yields,

$$b(r) = \frac{-C^{'}}{r^2} + \frac{K_G}{2} r + \frac{C_b}{r} - \big(\frac{\pi/3}{2\pi}\big)\frac{1}{r} \tag{4.43}$$

where continuum dislocation density $b(r)$ is related to areal defect density by, $\rho(r) = b(r)/|b|$. Matching the discontinuity in $\nabla \cdot \sigma$ at $r = L_1, L_2$, given $C^{'} = \frac{1}{24} L_1 \left(3K_G L_1^2 - 2\right)$ and using the stress continuity at $r = L_1$ leads to $C_b = 0$ and $s^{'} = \frac{\pi/3}{4\pi}$ which is equal to the charge of the centered 5-fold disclination.

In section IIA we find the total dislocation number N_d by integrating the dislocation density. We also mentioned that $b(r)$ changes its sign for the large surface coverage, $K_G W^2 > 1/3$, and in order to find the dislocation number we need to consider populating certain length of scars, $(1/\sqrt{3K_G W^2} < r < \ell_s)$, with the opposite dislocation polarization, due to the facts that $b(r)$ changes its sign for $K_G W^2 > 1/3$. This leads to to dislocation number for $K_G W^2 > 1/3$,

$$N_d = \frac{2\pi r_*}{3|b|}\left(1 - K_g r_*^2\right) - \frac{\pi \ell_s}{3|b|}\left(1 - K_g \ell_s^2\right) \tag{4.44}$$

where $r_* = W/\sqrt{3K_G W^2}$ is the radial position at which the dislocation density switches its polarization.

II. Charged scars in presence of compression: We seek an axially symmetric solution to the compatibility relation, eq. 4.1 in absence of dislocations. We focus on the effect of a generic compression at the boundary P, which requires the boundary condition, $\sigma_{rr}(r = W) = P$,

$$\begin{aligned} \sigma_{rr}^{f-axi}/Y &= \frac{s}{4\pi}(\ln(r/W)) + \frac{1}{16R^2}(W^2 - r^2) + P/Y; \\ \sigma_{\theta\theta}^{f-axi}/Y &= \frac{s}{4\pi}(\ln(r/W) + 1) + \frac{1}{16R^2}(W^2 - 3r^2) + P/Y \end{aligned} \tag{4.45}$$

Since we seek for the stress solution that collapses the tensile zone (generated by the bare disinclination) via a certain distribution of dislocations, we call these defects with the seven-fold head pointing to the center, "tensile dislocations". First we conjecture that a tension-free solution (similar to the case of charged scar with tensile boundary strain) where the hoop stress collapses with dislocations characterize by Burgers vectors $\mathbf{b} = -b\hat{\theta}$ that reside in an annulus $L_{tens.} < r < W$. Hence we construct the outer zone, tension-free solution where $\sigma_{\theta\theta} = \sigma_{r\theta} = 0$ and in-plane force balance equation in r direction becomes,

$$\partial_r \left(r\sigma_{rr} \right) = 0 \tag{4.46}$$

using the boundary condition at the edge of the sheet, $\bar{\sigma}^c_{rr}(r = W) = -P$ leads to radial compression $\bar{\sigma}^c_{rr} = -PW/r$. Hence the full solution in outer zone becomes,

$$(L < r < W) : \bar{\sigma}^c_{rr} = -PW/r; \bar{\sigma}^c_{\theta\theta} = 0 \tag{4.47}$$

In the inner zone in the vicinity of the centered disclination, the sheet is in an axisymmetric state, and solution may be calculated from eq. 4.2 by simple rescaling $W \to L$, up to an additive constat C,

$$\begin{aligned} \bar{\sigma}^c_{rr}/Y &= \frac{s}{4\pi}(\ln(r/L)) + \frac{1}{16R^2}(L^2 - r^2) + C; \\ \bar{\sigma}^c_{\theta\theta}/Y &= \frac{s}{4\pi}(\ln(r/L) + 1) + \frac{1}{16R^2}(L^2 - 3r^2) + C \end{aligned} \tag{4.48}$$

Two unknown constants, L and C are determined by requiring both stress fields σ_{rr}, $\sigma_{\theta\theta}$ to be continuous at $r = L$. Hence by matching both the inner and outer solutions we find $C = -PW/YL$ and for the length of the defective region we have the cubic equation,

$$\frac{Ls}{4\pi} - \frac{K_G L^3}{8} - \frac{PW}{Y} = 0 \tag{4.49}$$

Where $s = \pi/3$ is the disclinaiton topological charge. In the absence of the external pressure P we have two physical solutions for the length of defect-free zone, $L = 0, L/W = \sqrt{2/3}\left(K_G W^2\right)^{-1/2}$. This mechanism suggests two possible scenarios; In the case of $L = 0$, dislocations are tightly bounded to the centered disclination and extend to the boundary. For the second solution, $L/W = \sqrt{2/3}\left(K_G W^2\right)^{-1/2}$ there is always a finite gap between dislocations and the centered disclination and by increasing the curvature the length of the scarred region increases. This last solution determines a lower limit for the curvature, $K_G W^2 \geq 2/3$ and it is the critical curvature above which a compressive zone develops at the edge of the sheet. In order to find the real roots of the cubic eq. in 4.49, it can be written in the standard form of Vieta [155],

$$L^3 + pL = q \tag{4.50}$$

where we define $p = -(8/K_G)(s/4\pi)$ and $q = -(8/K_G)(PW/Y)$. Existence of real solutions can be accomplished by imposing a constraint on the polynomial discriminant, $D = (p/3)^3 + (q/2)^2 \geq 0$ [155]. This leads a critical compression $P_* = Y/27\left(\sqrt{2K_G W^2}\right)$ below which eq. 4.49 has a real solution. Under this condition the real solutions are of the form,

$$L_i = 2\sqrt{-Q}\cos\left(\frac{\theta}{3} + \frac{(i-1)2\pi}{3}\right) \tag{4.51}$$

for $i = 1, 2, 3$, $Q = p/3$ and $\theta = \cos^{-1}\left[(q/2)/\sqrt{-Q^3}\right]$. fig. 4.6 shows two physical roots of the cubic equation which reside in $0 < L_i < W$ for different values of curvature. For small curvature the condition for existence of the roots inside of the cap that indicates existence of the tensile zone for $r < W$ sets by substituting $L = W$ in eq. 4.49 which leads to a second condition for the compression, $P_\dagger/Y < Y(K_G W^2/8 - 1/12)$.

In order to find the "continuum density" of dislocations, we use the stress-free solution (eq. 4.48) as a stress field for the second Föppl- von Kàrmàn eq. (compatibility equation),

$$Y^{-1}\nabla_\perp^2 \bar{\sigma}_{ii}^c = -K_G + s\delta^2(\mathbf{r}) - \nabla_\perp \times \mathbf{b}(\mathbf{x}) \tag{4.52}$$

with $-\nabla_\perp \times \mathbf{b}(\mathbf{x}) = \sum_\alpha (\mathbf{b}_\alpha \times \nabla_\perp)\delta(\mathbf{x} - \mathbf{x}_\alpha)$ representing the continuous source of dislocations. Here we expect that the effective topological charge of scars is controlled by the fixed charge of disclination, Gaussian curvature and the stress-free field. After integrating the compatibility equation for $b(r)$ we have:

$$2\pi r b(r) = \left(\frac{2\pi P}{Y} \frac{W}{r} + \frac{\pi r^2}{R^2} - \frac{\pi}{3} + \frac{C}{r} \right) \tag{4.53}$$

In order to find the constant C we need to match the inner solution and outer solution of stress fields at $r = L$ in eq. 4.49, and we find that $\nabla \cdot \sigma$ is multi-valued at the tip of the scar. This shows that the dislocation density jumps from zero ($b^-(L) = 0$), to a finite value, $b^+(L)$. This condition can be written as, $Y b^+(L) = \partial_r \sigma_{ii}(r = L^+) - \partial_r \sigma_{ii}(r = L^-)$, yields $C = 0$. The areal density of dislocations $b(r)$ is related to their spacing on radial lines, arranged on N-fold symmetric scars (with angular spacing $2\pi/N$). This structure gives us the dislocation spacing $D = N_{scr}|b|/(2\pi r b(r))$ where $|b|$ is the length of the Burgers vector. Here we can define the dislocation line density $\lambda(r)^{-1} = D$. This enable us to evaluate the number n_d of dislocations-per-scar by integrating $\lambda(r)$ over the length of scars $n_d = \int_L^W \lambda(r) dr = \int_L^W 2\pi r b(r)/(N_{scr}|b|) dr$, yielding the product $n_d N_{scr}$, the total number of dislocation:

$$n_d N_{scr} = \frac{2\pi}{|b|} \int_L^W r b(r) dr = \frac{\pi}{3|b|} \left[(L - W) + K_G(W^3 - L^3) + \frac{6PW}{Y} \ln(W/L) \right] \tag{4.54}$$

This relation for the total number of dislocations shows that the excess disclination on the cap with larger curvature stabilizes fewer dislocations, compared to a system with shallower curvature and a larger number of tensile dislocations.

III. Displacement fields: Here we report the steps for computing the radial displacement field in presence of external compression that used in finding the dominant energy contribution in section IV A. In order to find the radial displacement field for the scarred cap with centered disinclination, $\bar{u}_r^{II_c}$, we first calculate the strain of the outer zone governed by the stress-free solutions in eq.

4.48. In the outer zone we have the compression free solution for stress $\bar{\sigma}_{rr}^{II_c} = -PW/r$, and strain $\bar{u}_{rr}^{II_c} = \frac{-PW}{Yr}$. On the other hand the geometric strain-displacement relation yields,

$$\bar{u}_{rr}^{II_c} = \partial_r \bar{u}_r^{II_c} + 1/2(r)^2 K_G, \tag{4.55}$$

where R is the radius of the curvature. Knowing $\bar{u}_{rr}^{II_c}$, we integrate eq. (4.55) yielding,

$$\bar{u}_r^{II_c} = -PW/Y \ln(r/C_0) - 1/6(r^3)K_G \tag{4.56}$$

where C_0 is determined by matching u_r at edge of the scarred (compression free) zone, $r = L$ which is the root of the eq. (4.49). For the radial displacement field in the inner zone, $\bar{u}_r^{I_c}$ using eq. 4.58, we have,

$$\begin{aligned} \bar{u}_{rr}^{I_c} &= \frac{1}{Y}\left(\bar{\sigma}_{rr}^{I_c} - \nu\bar{\sigma}_{\theta\theta}^{I_c}\right) \\ &= \frac{s}{4\pi}\ln(r/L) + \frac{K_G}{16}(L^2 - r^2) - \frac{PW}{YL} \\ &- \nu\left[\frac{s}{4\pi}(\ln(r/L) + 1) + \frac{K_G}{16}(L^2 - 3r^2) - \frac{PW}{YL}\right] \end{aligned} \tag{4.57}$$

and for the radial displacement field using eq. 4.58, we have $\bar{u}_r^{II_c} = \int \bar{u}_{rr}^{II_c} - 1/2(r)^2 K_G dr$. After integration, at the edge of the scarred (compression free) zone, $r = L$ this gives us,

$$\bar{u}_r^{I_c}(r = L) = \int_0^L \bar{u}_{rr}^{I_c} - 1/2r^2 K_G dr = \frac{1}{8}K_G L^3 - \frac{L(\pi/3)}{4\pi} + (\nu - 1)PW/Y \tag{4.58}$$

By matching displacement solutions for the inner and outer zone, $\bar{u}_r^{II_c}(r = L) = \bar{u}_r^{I_c}(r = L)$, we determine the unknown constant $C_0 = \exp\left[\frac{-K_G Y L^3}{24PW} + \frac{sYL}{4\pi PW} + (\nu - 1)\right]$L. Superimposing the cap solution on the sphere leads to the vanishing radial displacement which can be characterized by solving $\bar{u}_r^{II_c}(r = W) = 0$,

$$\begin{aligned} \bar{u}_r^{II_c}(r = W) &= -PW/Y \ln(r/C_0) - 1/6(r^3 K_G)\Big|_{r=W} \\ &= -1/6K_G W^3 + PW/Y\left[(\nu - 1) - \ln(W/L)\right] + K_G L^3/24 - L/12 \end{aligned} \tag{4.59}$$

Similarly For the case of neutral scar we have,

$$\begin{aligned} u_{rr}^{IIn} &= \frac{1}{Y}\left(\bar{\sigma}_{rr}^{II_n} - \nu\bar{\sigma}_{\theta\theta}^{II_n}\right) \\ &= -K_G\left(L^2 - r^2\right)^2/16r^2 - \nu K_G\left(L^4 + 2L^2r^2 - 3r^4\right)/16r^2 \end{aligned} \tag{4.60}$$

where $L = \ell_s^n = \sqrt{W - \frac{4\sqrt{P/Y}}{\sqrt{K_G}}}$. and for the radial displacement we have,

$$u_r^{IIn} = \int u_{rr}^{IIn} - 1/2K_G r^2 dr = K_G(L^2 - r^2)\left[L^2(\nu+1) - r^2(\nu-3)\right]/16r + C \tag{4.61}$$

$$u_r^{In} = -K_G r^3/6 \tag{4.62}$$

matching displacements at $r = L$ yields,

$$u_r^{IIn} = K_G(L^2 - r^2)\left[L^2(\nu+1) - r^2(\nu-3)\right]/16r - K_G L^3/6 \tag{4.63}$$

$$\tag{4.64}$$

We used this relation to compute the work done by the external compression, $2\pi W P u_r^{IIn}(r = W)$, at the boundary in the dominant part of the energy for neutral scars.

IV. Scar-Scar interaction: The total scar-scar interaction energy can be written in the form of,

$$E_{\rm ss}/Y \approx \sum_{k=1}^{n_s}\sum_{k'=1,k'\neq k}^{n_s}\frac{|b|^2}{n_s^2\epsilon}\int_0^{\ell_s}\tilde{\lambda}(r')dr'\int_0^{\ell_s}\tilde{\lambda}(r)\bar{E}_{int}^{D}(r,r')dr \tag{4.65}$$

This contribution to interaction is a double-sum of dislocation interactions reside on scar that are labeled by k and k', and radial positions of dislocations are labeled by r and r'. It is convenient to convert the dislocation-dislocation interaction E_{int}^{D} to disinclination interaction e_{int}^{D} that are

the constituent elements of dislocations in the form of $5-7$ dipoles. This can be achieved via, $E^D_{int} = |b|^2 \partial_r \partial_{r'} e^d_{int}$ and by part integration,

$$\begin{aligned}
E_{\rm ss}/Y &\approx \sum_{k=1}^{n_s} \sum_{k'=1,k'\neq k}^{n_s} \frac{1}{n_s^2 \epsilon} \int_0^{\ell_s} \tilde{\lambda}(r') dr' \int_0^{\ell_s} \tilde{\lambda}(r) E^D_{int}(r,r') dr \\
&= \sum_{k=1}^{n_s} \sum_{k'=1,k'\neq k}^{n_s} \frac{|b|^2}{n_s^2 \epsilon} \left[\tilde{\lambda(r)} \tilde{\lambda(r')} e^d_{int}(r,r') \Big|_{r=0}^{r=\ell_s} \Big|_{r'=0}^{r'=\ell_s} - \int_0^{\ell_s} \int_0^{\ell_s} \partial_r \partial_{r'} \tilde{\lambda}(r) \tilde{\lambda}(r') e^d_{int} \right] \\
&= n_s \int_0^{2\pi} \left(\frac{n_s}{2\pi} \right) d\phi \frac{|b|^2}{n_s^2 \epsilon} \left[\tilde{\lambda(r)} \tilde{\lambda(r')} e^d_{int}(r,r') \Big|_{r=0}^{r=\ell_s} \Big|_{r'=0}^{r'=\ell_s} - \int_0^{\ell_s} \int_0^{\ell_s} \partial_r \partial_{r'} \tilde{\lambda}(r) \tilde{\lambda}(r') e^d_{int} \right] \\
&- \int_0^{\delta\phi} \left(\frac{1}{2\pi} \right) d\phi \frac{|b|^2}{\epsilon} \left[\tilde{\lambda(r)} \tilde{\lambda(r')} e^d_{int}(r,r') \Big|_{r=0}^{r=\ell_s} \Big|_{r'=0}^{r'=\ell_s} - \int_0^{\ell_s} \int_0^{\ell_s} \partial_r \partial_{r'} \tilde{\lambda}(r) \tilde{\lambda}(r') e^d_{int} \right] \quad (4.66)
\end{aligned}$$

where $\tilde{\lambda}(r) = \tilde{\lambda}(r)\Theta(\ell_s - r)$ and $\Theta(r)$ is a Heaviside step function and e^d_{int} is the pairwise disclination interaction in eq. 4.18. Since disclination interactions are well behaved as separation between them approaches zero, we do not need to introduce a cut-off around disclination in contrast to the case of dislocation where there exist a logarithmic divergence around the dislocation core. First summation over scars is counted by the factor of n_s. Furthermore we approximate the second sum over scars, k' by the integral, $\sum_{k=1}^{n_s} F(k) \approx \int_1^{\infty} F(k) dk \approx \int_0^{2\pi} (n_s/2\pi) F(\phi) d\phi$ where $\phi = k(n_s/2\pi)$ is the angular separation between scars. This approximation is valid in the continuum limit where $n_s \to \infty$. The last term with upper limit of integration $\delta\phi = 2\pi/n_s$ is the interaction contribution needed to be subtracted to satisfy the double-sum constrain, $k \neq k'$. This contribution depends on scar number, n_s in contrast to the first term which is independent of the symmetry of the scar pattern. This energy contribution is vanishingly small in the asymptotic, $\lim_{n_s \to \infty} \delta\phi \to 0$ but this contribute to the subdominant part of the energy (next section). In order to understand the exact behavior of the sub-dominont part of the scar-scar interaction which to the highest order scales as, $\delta\phi\epsilon^{-1}$, we investigate the last term in eq. 4.66,

$$\begin{aligned}
E^{sub}_{\rm ss}/Y &\approx - \int_0^{\delta\phi} \left(\frac{1}{2\pi} \right) d\phi \frac{|b|^2}{\epsilon} \left[\tilde{\lambda(r)} \tilde{\lambda(r')} e^d_{int}(r,r') \Big|_{r=0}^{r=\ell_s} \Big|_{r'=0}^{r'=\ell_s} - \int_0^{\ell_s} \int_0^{\ell_s} \partial_r \partial_{r'} \tilde{\lambda}(r) \tilde{\lambda}(r') e^d_{int} \right] \\
&= \frac{|b|^2}{\epsilon n_s} \left(\frac{\pi^2}{4} - \frac{\pi}{3 K_G W^2} \right) + O(\delta\phi^2) + ... \quad (4.67)
\end{aligned}$$

Here we used the fact that in $e^d_{int}(r,r',\phi)$ (see eq. 4.18) the part that depends on ϕ contribute to the interaction energy, E_{ss} to the second (and higher) order in $\delta\phi$ for $n_s \to \infty$. We divide scar-scar interaction, E_{ss} to two parts, subdominant part E^{sub}_{ss} and dominant part, $E^{dom}_{ss} = E_{ss} - E^{sub}_{ss}$. Comparing the dominant scale of scar-scar interaction, E_{ss} to the scale of the scar self energy eq. 4.29, shows that in the continuum limit we have the $\lim_{b/W\to 0} E_{self}/E_{ss} \approx \epsilon^{1/2}$.

V. Scar self-energy and sub-dominant scale: We can improve the scaling predictions in eq. 4.29 for the elastic energy by the exact calculation for the elastic self-energies of the n_s charged scars that can be written as the summations

$$E^c_{\rm self}/n_s = \sum_{\alpha=2}^{M}\sum_{\beta<\alpha}^{M} E^D_{int}\left(r_\alpha, r_\beta\right) + \sum_{\alpha=1}^{M} E^D_{self}\left(r_\alpha\right), \tag{4.68}$$

where $M = N_d/n_s$ is the number of dislocation per scar. To approximate the value of the discrete sums along the scar, we replace dislocation self-energies and interaction energies with their *mean values* along intervals of width $D(r_\alpha)$, centered around dislocation positions r_α, allowing us to convert sums to integrals,

$$\begin{aligned} E^c_{\rm self}/n_s &\cong \int_0^{W-D(W)/2} \lambda(r', T/T_*)dr' \int_{r'+D(r')/2}^{W} \lambda(r, T/T_*) E^D_{int}\left(r, r'\right) dr \\ &+ \int_0^W \lambda(r, T/T_*) E^D_{self}\left(r\right) dr, \end{aligned} \tag{4.69}$$

where we have dropped $\pm D/2$ corrections to the range of integration at the ends of scars $r = 0$ and $r = W$ for $T \to 0$. Here we can define $\rho(r)$ that is related to defect density by, $\rho(r) = b(r)/|b|$ and $b(r)$ given in eq. 4.44 for charged scars. Since $\rho(r)$ is independent of scar number, n_s, the scar number enters the self-energy calculation of scars only through the change in linear density of dislocations along a scar, $\lambda(r)$. Assuming pattern of n_s-fold symmetry we find a local dislocation spacing $D(r) = 1/\lambda(r)$,

$$\lambda(r) = 2\pi r \frac{b(r)}{|b|n_s} = -\frac{K_g}{|b|n_s}\left[\pi r^2 - \frac{\pi/3}{K_g}\right] = -\epsilon^{-1/2}/n_s\left[\pi r^2 - \frac{\pi/3}{K_g}W^{-3}\right] = \epsilon^{-1/2}/n_s\tilde{\lambda}(r) \tag{4.70}$$

Collecting all terms we find the total self-energy of scars as a function of scar number, n_s and Gaussian curvature, K_g,

$$\begin{aligned} E^c_{\rm self}(n_s, K_g) &= \frac{4\pi^2}{n_s}\int_0^W \rho(r')r'dr' \int_{r'+n_s\epsilon^{1/2}d(r')}^W \rho(r)E^D_{int}(r,r')rdr \\ &+ 2\pi\int_L^W \rho(r)E^D_{self}(r)rdr. \end{aligned} \tag{4.71}$$

The scar self energy is minimized numerically with respect to scar number for different values of curvature

$$\begin{aligned} E^c_{\rm self}(n_s, K_g)/4\pi^2 &= \frac{|b|^2}{n_s\epsilon}\int_0^W \tilde{\lambda}(r')dr' \int_{r'+n_s\epsilon^{1/2}d(r')}^W \tilde{\lambda}(r)\bar{E}^D_{int}(r,r')dr \\ &+ (2\pi)^{-1}\frac{|b|^2}{\epsilon^{1/2}}\int_L^W \tilde{\lambda}(r)\bar{E}^D_{self}(r)dr. \end{aligned} \tag{4.72}$$

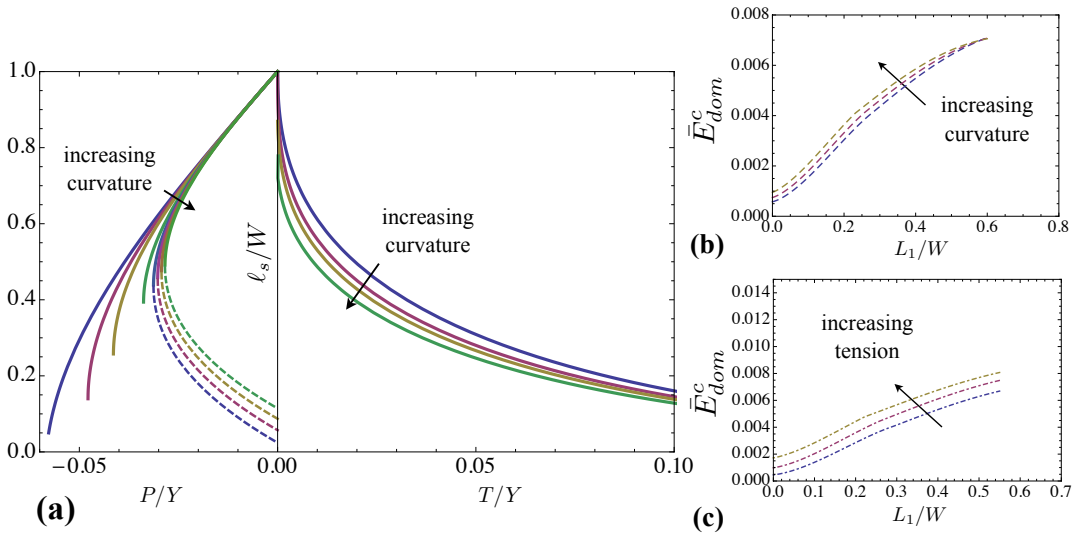

Figure 4.6. (a) shows two physical roots of eq. 4.49, $\ell_s = W - L$ in the presence of compression for increasing Gaussian curvature. The first root as a function compression exists for all values of P/Y, in contrast to the second root, dashed lines that exist for $K_g W^2 \geq 2/3$. (b) and (c) shows the dominant energetics of charged scar as a function of L_1 related to three-zones stress-relaxed solutions for $T/Y = 0.01$ and increasing values of curvature $K_G W^2 = 0.08 - 0.22$ in (b) and fixed surface coverage, $K_G W^2 = 0.05$ and a sequence of increasing tension, $T/Y = 0.011 - 0.021$ in (c).

BIBLIOGRAPHY

[1] Randall D. Kamien, Science 299, 5613 (2003).

[2] G. A. DeVries, et al. Science 315, 358 (2007).

[3] W. L. Bragg and J. F. Nye, Proc. Roy. Soc. A **190**, 474 (1947).

[4] Varpu Marjomki, et al. Proc. Nat. Acad. Sci. USA **111** (2014).

[5] Gregory M. Grason, Rev Of Mod Phys, **87**, 401 (2015).

[6] Klman, M. J. Phys. Lett. **46**, 723 (1985).

[7] J. P. Sethna, D. C. Wright and N. D. Mermin, Phys. Rev. Lett. **51**, 467 (1983).

[8] J. M. Kosterlitz and D. J. Thouless, Prog. Low Temp. Phys. , **78**, 371 (1978).

[9] V.L. Berezinski, Zh, Eksp. Teo. Fiz. **59**, 907, (1970) [Sov. Phys. JEPT **32**, 493, (1971).

[10] B. I. Halperin and D. R. Nelson, Phys. Rev. Lett. **41** , 121 (1978).

[11] D. R. Nelson and B. I. Halperin, Phys. Rev. B **19**, 2457 (1979).

[12] E. Cerda and L. Mahadevan, Phys. Rev. Lett. **90**, 074302 (2003).

[13] H. King, R. D. Schroll, B. Davidovitch, Proc. Nat. Acad. Sci. USA **109**, 9716 (2012).

[14] B. Davidovitch, R. D. Schroll, D. Vella, M. Adda-Bedia and E. A. Cerda, **108**, 18227 (2011).

[15] G. M. Grason and B. Davidovitch, Proc. Nat. Acad. Sci. USA **110**, 12893 (2013).

[16] S. Schneider and G. Gompper, Europhys. Lett. **70**, 136 (2005).

[17] Alexander Yu. Morozov and Robijn F. Bruinsma, Phy. Rev. E **81**, 041925 (2010)

[18] D.R. Nelson, *Defects and Geometry in Condensed Matter Physics* (Cambridge University Press, Boston, 2002).

[19] J.-F. Sadoc and R. Mosseri, *Geometrical Frustration*, (Cambridge, Cambridge, 1999).

[20] Yang, S., L. Zhao, C. Yu, X. Zhou, J. Tang, P. Yuan, D. Chen, and D. Zhao, J. Am. Chem. Soc. **128**, 10460 (2006).

[21] E. L. Altschuler, T. J. Williams, E. R. Ratner, T. Tipton, R. Strong, F. Dowla and F. Wooten, Phys. Rev. Lett. **72**, 2671 (1994).

[22] T. Aste and D. L. Weaire, *The Pursuit of Perfect Packing*, 2nd ed. (Taylor and Francis, New York, 2008).

[23] D. L. D. caspar and A. Klug, Cold Spring Harbor Symp. Quant. Biol. **27**, 1 (1962).

[24] R. Zandi, D. Reguera, R. F. Bruinsma, W. M. Gelbart and J. Rudnick, Proc. Nat. Acad. Sci. USA **101**, 15556 (2004).

[25] A. D. Dinsmore, M. F. Hsu, M. G. Nikolaides, M. Marques, A. R. Bausch and D. A. Weitz, Science **298**, 1006 (2002).

[26] A. R. Bausch, M. J. Bowick, A. Cacciuto, A. D. Dinsmore, M. F. Hsu, D. R. Nelson, M. G. Nikolaides, A. Travesset and D. A. Weitz, Science **299**, 1716 (2003).

[27] D. R. Nelson and L. Peliti, J. Phys. France **48**, 1085 (1987).

[28] H. S. Seung and D. R. Nelson, Phys. Rev. A **38**, 1005 (1988).

[29] M. J. Bowick, D. R. Nelson and A. Travesset, Phys. Rev. B **62**, 8738 (2000).

[30] M. J. Bowick and L. Giomi, Adv. in Phys. **58**, 449 (2009).

[31] W. T. Irvine, V. Vitelli and P. M. Chaikin, Nature **468**, 947 (2011).

[32] G. M. Grason, Phys. Rev. Lett. **105**, 045502 (2010).

[33] G. M. Grason, *to be published* (2011).

[34] P. Fratzl, Curr. Opin. Colloid Interface Sci. **8**, 32 (2003).

[35] T. J. Wess, in *Collagen: Structure and Mechanics*, edited by P. Fratzl (Springer, Boston, 2008), Chap. 3.

[36] J. W. Weisel, J. Thromb. Haemost. **5** (Suppl. 1), 116 (2007).

[37] J. W. Weisel, C. Nagaswami and L. Makowski, Proc. Nat. Acad. Sci. USA **84**, 8991 (1987).

[38] M. S. Turner, R. W. Briehl, F. A. Ferrone, and R. Josephs, Phys. Rev. Lett. **90**, 128103 (2003).

[39] G. M. Grason and R. F. Bruinsma, Phys. Rev. Lett. **99**, 098101 (2007).

[40] G. M. Grason, Phys. Rev. E **79**, 041919 (2009).

[41] Y. Yang, R. B. Meyer and M. F. Hagan, Phys. Rev. Lett. **104**, 258102 (2010).

[42] C. Heussinger and G. M. Grason **135**, 035104 (2011).

[43] L. Giomi and M. Bowick, Phys. Rev. B **76**, 054106 (2007).

[44] S. Schneider and G. Gompper, Europhys. Lett. **70**, 136 (2005).

[45] M. Bowick, A. Caccuito, D. R. Nelson and A. Travesset, Phys. Rev. Lett. **89**, 185502 (2002).

[46] P. G. de Gennes and J. Prost, *The Physics of Liquid Crystals* (Claredon, Oxford, 1993), 2nd ed.

[47] J. V. Selinger and R. F. Bruinsma, Phys. Rev. A **43**, 2910 (1991).

[48] L. D. Landau and E. M. Lifshitz, *Theory of Elasticity* (Pergamon, Oxford, 1986), 3rd ed., Chap. 2.

[49] J. S. Koehler, Phys. Rev. **60**, 397 (1941).

[50] J.P. Hirth, J. Lothe, *Theory of Dislocations* (McGraw-Hill, New York,1968).

[51] F. R. N. Nabarro, *Theory Of Crystal Dislocations* (Oxford University Press, Oxford, 1967).

[52] M. Peach and J. S. Khoehler, Phys. Rev. **80**, 436 (1950).

[53] A. Travesset, Phys. Rev. B, **68**, 115421 (2003).

[54] R. Bruinsma, B. I. Halperin and A. Zippelius, Phys. Rev. B **25**, 579 (1982).

[55] M. J. Bowick and Z. Yao Europhys. Lett. **93**, 36001 (2011).

[56] V. Ottani, M. Raspanti and A. Ruggeri, Micron **32**, 251 (2001).

[57] D. J. Prockop and A. Fertala, J. Struct. Biol. **122**, 111 (1998).

[58] J. Charvolin and J.-F. Sadoc, Biophys. Rev. and Lett. **6**, 13 (2011).

[59] D. J. Hulmes, T. J. Wess, D. J. Prockop and P. Fratzl, Biophys. J. **68**, 1661 (1995).

[60] Azizi, A. et al. Nat. Commun. 5, 4867 (2014).

[61] D. L. D. Caspar and A. Klug, Cold Spring Harbor Symp. Quant. Biol. **27**, 1 (1962).

[62] R. Zandi, D. Reguara, R. F. Bruinsma, W. M. Gelbart and J. Rudnick, Proc. Nat. Acad. Sci. USA **101**, 15556 (2004).

[63] M. J. Bowick, A. Cacciuto, D. R. Nelson, and A. Travesset, Phys. Rev. B **73**, 024115 (2006).

[64] M. J. W. Dodgson and M. A. Moore, Phys. Rev. B **55**, 3816 (1997).

[65] A. Siber, arXiv:0711.3527 (2007).

[66] S. Schneider and G. Gompper, Europhys. Lett. **70**, 136 (2005).

[67] J. Hure, B. Roman and J. Bico, Phys. Rev. Lett. **106**, 174301 (2011).

[68] A. Y. Morozov and R. F. Bruinsma, Phys. Rev. E **81**, 041925 (2010).

[69] G. Meng, J. Paulose, D. R. Nelson and V. N. Manoharan, Science **343**, 634 (2014).

[70] G. Vernizzi, R. Sknepnek and M. Olvera de la Cruz, Proc. Nat. Acad. Sci. USA **108**, 4292 (2010).

[71] A. R. Bausch, M. J. Bowick, A. Cacciuto, A. D. Dinsmore, M. F. Hsu, D. R. Nelson, M. G. Nikolaides, A. Travesset and D. A. Weitz, Science **299**, 1716 (2003).

[72] M. Kléman, Adv. Phys. **38**, 605 (1989).

[73] J.-F. Sadoc and R. Mosseri, *Geometrical Frustration*, Cambridge University Press, Cambridge, (1999).

[74] E. L. Altschuler, T. J. Williams, E. R. Ratner, F. Dowla and F. Wooten, Phys. Rev. Lett. **72**, 2671 (1994).

[75] M. Bowick, A. Caccuito, D. R. Nelson and A. Travesset, Phys. Rev. Lett. **89**, 185502 (2002).

[76] W. T. Irvine, V. Vitelli and P. M. Chaikin, Nature **468**, 947 (2011).

[77] D. J. Wales, H. McKay and E. L. Altschuler, Phys. Rev. B **79**, 224115 (2009).

[78] H. Kusumaatmaja and D. J. Wales, Phys. Rev. Lett. **110**, 165502 (2013).

[79] M. Bowick, D. R. Nelson and A. Travesset, Phys. Rev. B **62**, 8738 (2000).

[80] A. Travesset, Phys. Rev. B **68**, 115421 (2003).

[81] V. Vitelli, J. B. Lucks and D. R. Nelson, Proc. Nat. Acad. Sci USA **103**, 12323 (2006).

[82] G. M. Grason and B. Davidovitch, Proc. Nat. Acad. Sci. USA **110**, 12893 (2013).

[83] E. Cerda and L. Mahadevan, Phys. Rev. Lett. **90**, 074302 (2003).

[84] H. King, R. D. Schroll, B. Davidovitch, Proc. Nat. Acad. Sci. USA **109**, 9716 (2012).

[85] D. R. Nelson, *Defects and Geometry in Condensed Matter Physics*, (Cambridge, Cambridge, 2002).

[86] G. M. Grason, Phy. Rev. Lett. **105**, 045502 (2010).

[87] G. M. Grason, Phy. Rev. E **85**, 031603 (2012).

[88] A. Azadi and G. M. Grason, Phy. Rev. E **85**, 031604 (2012).

[89] J. P. Hirth and J. Lothe, *Theory of Dislocations*, (Wiley, New York, 1982).

[90] B. Davidovitch, R. D. Schroll, D. Vella, M. Adda-Bedia and E. A. Cerda, **108**, 18227 (2011).

[91] A. Azadi and G. M. Grason, to be published.

[92] D. L. D. Caspar and A. Klug, Cold Spring Harb Symp. Quant Biol. 27, 1 (1962).

[93] Altschuler EL, et al. . Phys Rev Lett 78 2681 (1997).

[94] U. Albrecht and P. Leiderer, J. Low Temp. Phys. 86, 131 (1992).

[95] P. Leiderer, Z. Phys. B: Condens. Matter 98, 303 (1993).

[96] C. C. Grimes and G. Adams, Phys. Rev. Lett. 42, 795 (1979).

[97] D. C. Glattli, E. Y. Andrei, and F. I. B. Williams, Phys. Rev. Lett. 60, 420 (1998).

[98] Prez-Garrido, M. J. W. Dodgson, and M. A. Moore, Phys. Rev. B 56, 3640 (1997).

[99] Prez-Garrido and M. A. Moore, Phys. Rev. B 60, 15628 (1999).

[100] M. J. Bowick, D. R. Nelson, and A. Travesset, Phys. Rev. B 62, 8738 (2000).

[101] S. B. Dierker, R. Pindak, and R. B. Meyer, Phys. Rev. Lett. 56, 1819 (1986).

[102] S. B. Dierker, R. Pindak, and R. B. Meyer, Phys. Rev. Lett. 56, 1819 (1986).

[103] A. Pe'rez-Garrido, M. J. W. Dodgson, and M. A. Moore, Phys. Rev. B 56, 3640 (1997).

[104] H. Vandeparre, M. Pineirua, et. Phys. Rev. Lett. **106**, 224301 (2011).

[105] Kim P. Abkarian, M. Stone, H.A. Nature Mater. **10**, 952 (2011).

[106] M.C. Miguel, A. Mughal, S. Zapperi, Phys. Rev. Lett. **106**, 245501 (2011).

[107] M.C. Miguel and S.Zapperi, NatureMater. 2, 477 (2003).

[108] D. L. D. Caspar and A. Klug, Cold Spring Harbor Symp. Quant. Biol. **27**, 1 (1962).

[109] R. Zandi, D. Reguara, R. F. Bruinsma, W. M. Gelbart and J. Rudnick, Proc. Nat. Acad. Sci. USA **101**, 15556 (2004).

[110] M. J. Bowick, A. Cacciuto, D. R. Nelson, and A. Travesset, Phys. Rev. B **73**, 024115 (2006).

[111] M. J. W. Dodgson and M. A. Moore, Phys. Rev. B **55**, 3816 (1997).

[112] A. Siber (2007), arXiv:0711.3527.

[113] S. Schneider and G. Gompper, Europhys. Lett. **70**, 136 (2005).

[114] A. Azizi, et al. Nat. Commun. 5, 4867 (2014).

[115] J. Hure, B. Roman and J. Bico, Phys. Rev. Lett. **106**, 174301 (2011).

[116] A. Y. Morozov and R. F. Bruinsma, Phys. Rev. E **81**, 041925 (2010).

[117] G. Meng, J. Paulose, D. R. Nelson and V. N. Manoharan, Science **343**, 634 (2014).

[118] G. Vernizzi, R. Sknepnek and M. Olvera de la Cruz, Proc. Nat. Acad. Sci. USA **108**, 4292 (2010).

[119] A. R. Bausch, M. J. Bowick, A. Cacciuto, A. D. Dinsmore, M. F. Hsu, D. R. Nelson, M. G. Nikolaides, A. Travesset and D. A. Weitz, Science **299**, 1716 (2003).

[120] D.J. Wales, H. Mackay and E.L. Altshuler, Phys. Rev. B **79**, 224115 (2009).

[121] M. Stein and J.M. Hedgpeth, NASA Technical Note, **813** (1961); A.C. Pipkin, IMA J. Appl. Math **36**, 85 (1986)

[122] M. Kléman, Adv. Phys. **38**, 605 (1989).

[123] J.-F. Sadoc and R. Mosseri, *Geometrical Frustration* (Cambridge University Press, Cambridge, 1999).

[124] E. L. Altschuler, T. J. Williams, E. R. Ratner, F. Dowla and F. Wooten, Phys. Rev. Lett. **72**, 2671 (1994).

[125] M. Bowick, A. Caccuito, D. R. Nelson and A. Travesset, Phys. Rev. Lett. **89**, 185502 (2002).

[126] W. T. Irvine, V. Vitelli and P. M. Chaikin, Nature **468**, 947 (2011).

[127] D. J. Wales, H. McKay and E. L. Altschuler, Phys. Rev. B **79**, 224115 (2009).

[128] H. Kusumaatmaja and D. J. Wales, Phys. Rev. Lett. **110**, 165502 (2013).

[129] M. Bowick, D. R. Nelson and A. Travesset, Phys. Rev. B **62**, 8738 (2000).

[130] A. Travesset, Phys. Rev. B **68**, 115421 (2003).

[131] V. Vitelli, J. B. Lucks and D. R. Nelson, Proc. Nat. Acad. Sci USA **103**, 12323 (2006).

[132] G. M. Grason and B. Davidovitch, Proc. Nat. Acad. Sci. USA **110**, 12893 (2013).

[133] E. Cerda and L. Mahadevan, Phys. Rev. Lett. **90**, 074302 (2003).

[134] H. King, R. D. Schroll, B. Davidovitch, Proc. Nat. Acad. Sci. USA **109**, 9716 (2012).

[135] G. M. Grason, Phy. Rev. Lett. **105**, 045502 (2010).

[136] G. M. Grason, Phy. Rev. E **85**, 031603 (2012).

[137] A. Azadi and G. M. Grason, Phy. Rev. E **85**, 031604 (2012).

[138] J. P. Hirth and J. Lothe, *Theory of Dislocations*, (Wiley, New York, 1982).

[139] B. Davidovitch, R. D. Schroll, D. Vella, M. Adda-Bedia and E. A. Cerda, **108**, 18227 (2011).

[140] D. L. D. Caspar and A. Klug, Cold Spring Harb Symp. Quant Biol. 27, 1 (1962).

[141] Altschuler EL, et al. . Phys Rev Lett 78 2681 (1997).

[142] U. Albrecht and P. Leiderer, J. Low Temp. Phys. 86, 131 (1992).

[143] P. Leiderer, Z. Phys. B: Condens. Matter 98, 303 (1993).

[144] C. C. Grimes and G. Adams, Phys. Rev. Lett. 42, 795 (1979).

[145] D. C. Glattli, E. Y. Andrei, and F. I. B. Williams, Phys. Rev. Lett. 60, 420 (1998).

[146] Prez-Garrido, M. J. W. Dodgson, and M. A. Moore, Phys. Rev. B 56, 3640 (1997).

[147] Prez-Garrido and M. A. Moore, Phys. Rev. B 60, 15628 (1999).

[148] M. J. Bowick, D. R. Nelson, and A. Travesset, Phys. Rev. B 62, 8738 (2000).

[149] S. B. Dierker, R. Pindak, and R. B. Meyer, Phys. Rev. Lett. 56, 1819 (1986).

[150] H. Vandeparre, M. Pineirua, et. Phys. Rev. Lett. **106**, 224301 (2011).

[151] Kim P. Abkarian, M. Stone, H.A. Nature Mater. **10**, 952 (2011).

[152] M.C. Miguel, A. Mughal, S. Zapperi, Phys. Rev. Lett. **106**, 245501 (2011).

[153] M.C. Miguel and S.Zapperi, NatureMater. 2, 477 (2003).

[154] A. Azadi, G.M. Grason Phys. Rev. Lett. **112**, 225502 (2014).

[155] Beyer, W. H. CRC Standard Mathematical Tables, 28th ed. Boca Raton, FL: CRC Press, (1987); Theory of Equations by J.V. Uspensky, McGraw Hill, 1st ed. (1948).